PREDICTING ELASTIC PROPERTIES OF LIQUID CRYSTALS FROM

MOLECULAR SIMULATION

A Dissertation

Submitted to the Graduate School

of the University of Notre Dame

in Partial Fulfillment of the Requirements

for the Degree of

Doctor of Philosophy

by

Hythem Sidky

_____

Jonathan K. Whitmer, Director

Graduate Program in Chemical and Biomolecular Engineering

Notre Dame, Indiana

April 2018

PREDICTING ELASTIC PROPERTIES OF LIQUID CRYSTALS FROM MOLECULAR SIMULATION

Abstract

by

Hythem Sidky

The elastic behavior of liquid crystalline materials plays an important role in the design of responsive electrical, mechanical, and optical devices. This dissertation focuses on developing, extending, and implementing sampling methods to predict the elastic properties of liquid crystals from molecular simulation. The utility of molecular simulation in predicting elastic properties of liquid crystals has historically been limited due to the immense time and length scales needed to generate accurate estimates of quantities such as the bulk elastic moduli. A recently proposed free energy perturbation method was shown to overcome many of these limitations and produce reliable estimates of the elastic constants. However, there remained a number of challenges to be addressed which would eliminate the use of approximations and extend the technique to molecular systems.

We begin by introducing uniaxial nematic liquid crystals and Frank elastic theory. Next, a series of studies of increasing complexity investigating the elastic properties of liquid crystal systems are presented. First, we perform comprehensive study of binary liquid crystal mixtures represented by the multicomponent Lebwohl-Lasher lattice model. Then we use density-of-states simulations to systematically study the elastic properties of four common Gay–Berne nematogenic models. The third study investigates the elastic and thermodynamic properties of chromonic liquid crystals which

exhibit a unique self–assembly process. Finally, we present the first direct simulations of the bulk and surface-like elastic constants for molecular 4-5-alkyl-4'-cyanobiphenyl which challenge indirect experimental observations that suggest spontaneous elastic curvature in certain geometries.

وَمَا تَوْفِيقِي إِلَّا بِاللَّهِ

To my mother.

CONTENTS

TABLES

ACKNOWLEDGMENTS

A special thanks and a debt of gratitude to Manish Kelkar for encouraging me to apply to graduate school *one last time*, and for personally recommending me to Dr. Edward Maginn. I acknowledge my University of Chicago collaborators for their contributions and work on the advanced sampling suite, SSAGES. Thanks to Dhagash Mehta, who introduced me to the wonderful world of algebraic geometry, and to my ACMS adviser Dr. Jonathan Hauenstein for his mentorship and instruction.

To my wife *Dunia*, whose name means "world", and whose patience, support, and love mean the world to me. She had no idea what she was getting herself into, yet somehow managed to be my anchor. I shall forever be grateful for her personal sacrifices over the past few years. To my family for their everlasting and unconditional support and encouragement. I could not have accomplished anything without them. To my cat Whiskers who kept me company day and night and took it upon herself to replace my alarm clock.

To my mother. There are no words to express what she has done for me. I know that my years of study have been difficult for her as I was not able to be with her in times of need. I dedicate this dissertation to her.

I would like to thank the department administrative staff, especially Nadia Casas and Anne Veselik for helping me navigate the finer aspects of graduate school. I acknowledge the Notre Dame Center for Research Computing for their computational resources and support, and the National Science Foundation Graduate Research Fellowship (NSF-GRFP) for financial support and recognition.

Finally, I would like to thank God, for truly His blessings are innumerable. My success lies with Him alone.

CHAPTER 1

INTRODUCTION

Liquid crystals (LC) are molecules that organize into intermediate phases of matter having liquid-like positional and solid-like orientational order. Transitions between these *mesophases* may be induced through a change in temperature (*thermotropic* LCs), or density (*lyotropic* LCs). Such phases exhibit a curvature elasticity which disfavors deviations from global orientational order. Thermotropic LCs, in particular, are prominent in the manufacture of liquid crystalline displays (LCDs) [1, 2], where ordering transitions in LCDs are forcibly triggered through external stress, exploiting competition between elastic restoring forces, surface forces, and imposed fields. The combined stresses modify the internal morphologies of the LC and change how light propagates through them. This property also makes LCs particularly useful in sensing applications [3–6], where intriguing new devices exploit intraphase morphological transformations of LC droplets for biomolecule detection [7, 8]. Local LC morphologies have similarly been utilized to facilitate nanoparticle and colloidal self-assembly [9–16], owing to the character of surface-imposed defects present in the system. It is clear that a fundamental molecular-level understanding of elasticity and ordering transitions arising through external stress and geometric frustration is crucial in advancing applied LC technologies.

Many theoretical frameworks have been developed to describe the phenomenology of LCs. Onsager [17] formulated a purely entropic model for systems of hard rods, while the Maier–Saupe mean field model [18, 19] captured anisotropic van der Waals interactions more explicitly, using a description based on enthalpic interac-

1

tions. Each represents an ideal situation targeting one part of the entropy–enthalpy balance. To unify both concepts, molecular simulations have augmented theoretical arguments, replacing hard rods with ellipsoidal particles having orientationally dependent attraction [20], and full molecular models [21–23]. Lattice approaches derived from Maier–Saupe theory have also been modified to define spatially dependent interactions [24].

In particular, cases involving *uniaxial* nematic liquid crystals, where individual molecules in bulk align on average with a global nematic director $\hat{\mathbf{n}}$, have been greatly informed by the use of molecular simulations [25–29]. It is often of interest to understand how boundaries, particle inclusions, and external fields can perturb a system away from homogeneous bulk conditions. These situations incur an order-elastic free-energy penalty in the nematic liquid, with each individual deformation characterized by its own elastic constant [30]. In practice symmetry concerns reduce the independent degrees of freedom considerably [31, 32]. In the absence of molecular polarity and chiral interactions, the linear-order elastic free energy density of a uniaxial nematic may be represented in the Frank-Oseen form [33, 31, 32, 34]

$$
\begin{aligned}
f_{\text{FO}} = {} & \frac{1}{2}k_{11}\left(\nabla\cdot\hat{\mathbf{n}}\right)^2 + \frac{1}{2}k_{22}\left(\hat{\mathbf{n}}\cdot\nabla\times\hat{\mathbf{n}}\right)^2 + \frac{1}{2}k_{33}\left(\hat{\mathbf{n}}\times\nabla\times\hat{\mathbf{n}}\right)^2 \\
& + \frac{1}{2}\left(k_{22}+k_{24}\right)\left[\text{Tr}\left(\nabla\hat{\mathbf{n}}\right)^2 - \left(\nabla\cdot\hat{\mathbf{n}}\right)^2\right] \ .
\end{aligned}
\tag{1.1}
$$

This expression contains the most commonly used elastic terms: splay (k_{11}), twist (k_{22}) and bend (k_{33}). The additional term, referred to as "saddle-splay", depends on k_{24} and penalizes bidirectional deformations. This surface-like term has been the subject of considerable recent interest due to its role in dictating confined morphologies of liquid crystals [35–38], though it has often been ignored in bulk studies. The free-energy density is phrased so that it is positive definite, and globally homogenous in equilibrium, which places bounds on the values of the four elastic constants [39]. Terms which imply a spontaneous deformation of the global nematic texture (such

as the chiral term t_0 [31, 32]) are not present in this expansion.

Though this energy is relatively simple to phrase, elastic properties are difficult to measure experimentally. The saddle-splay constant k_{24}, in particular, which penalizes bi-directional deformations, [40] is only accessible through indirect measurements that rely on morphological instability thresholds. [41–43, 36, 37] Past experimental studies have reported conflicting measurements, and some of the published values of k_{24} have in fact been found to lie outside stability criteria established by Ericksen, [39] hinting at new physics that may be used to purposely engineer instability into nematic materials. Note that the form above contrasts with another common theoretical representation (the Landau–de Gennes free energy [44]) which utilizes the nematic order tensor $\mathbf{Q}$, which can simultaneously handle phase and elastic behavior—such a representation is debatably more relevant due to recent observation of biaxial ring defects in otherwise uniaxial mesophases [16]. Though these two representations cannot be easily mapped onto each other, and the elastic coefficients in the $\mathbf{Q}$ representation are often inferred from the Frank–Oseen form above [44].

An intriguing subset of LCs are lyotropic chromonic liquid crystals (LCLCs), which derive their name from early studies on the anti-asthmatic Chromolyn (disodium cromoglycate, or DSCG), [45] and encompass many molecularly similar drugs and dyes. [46] The predominant forms are flat molecules with aromatic cores which experience energetically favorable π-stacking interactions, causing the molecules to arrange into elongated rod-like assemblies. As the length of these aggregates approaches a critical value, the rods will spontaneously order into a nematic phase. Further densification leads to the formation of a columnar phase. As one might expect from the enthalpic origins of stacking, these phases possess a partial thermotropic character, as stacks cannot elongate sufficiently if the temperature is too high. [47]

Additional complexity occurs in the presence of depletants, and, if the molecules

are charged, salt. [48–50] This latter case, which we will refer to as an ionic lyotropic chromonic liquid crystal (iLCLC) includes many common LCLCs such as DSCG and sunset yellow dye (SSY). [22, 51] These latter systems have been the subject of intense recent scrutiny due to novel morphologies and defect formations which arise from large elastic anisotropy, with the "twist" elastic mode having a tenfold cheaper elastic cost in many cases. [52, 53, 51, 37, 54] Such behavior is similar to that predicted by Meyer and co-workers [55] for long flexible polymer chains, and thus must be determined directly by the equilibrium stacking behavior of mesogens.

This dissertation explores and predicts the elastic behavior of thermotropic and lyotropic chromonic liquid crystals using molecular simulation. A new methodology is presented throughout which utilizes enhanced sampling calculations to estimate *in silico* the Frank elastic free energy of both coarse-grained and atomistic systems. Chapters 2-5 consist of a series of independent published studies of increasing complexity investigating lattice, coarse-grained, chromonic, and molecular LCs. The publications constituting each chapter are:

- Chapter 2: Hythem Sidky and Jonathan K. Whitmer, "Elastic response and phase behavior in binary liquid crystal mixtures" *Soft Matter*, **12**, 19, 4489-4498 (2016).

- Chapter 3: Hythem Sidky and Jonathan K. Whitmer, "Elastic properties of common Gay-Berne nematogens from density of states (DOS) simulations" *Liquid Crystals*, **43**, 13-15, 2285-2299 (2016).

- Chapter 4: Hythem Sidky and Jonathan K. Whitmer, "The emergent nematic phase in ionic chromonic liquid crystals" *Journal of Physical Chemistry B*, **121**, 27, 6691-6698 (2017).

- Chapter 5: Hythem Sidky, Juan J. de Pablo, and Jonathan K. Whitmer, "In silico measurement of elastic moduli of nematic liquid crystals" *Physical Review Letters*, **120**, 10, 107801 (2018).

The final chapter provides a summary of the work in this dissertation and discusses potential improvements and future directions.

CHAPTER 2

ELASTIC RESPONSE AND PHASE BEHAVIOR IN BINARY LIQUID
CRYSTAL MIXTURES

2.1 Introduction

The elastic responses of liquid crystals (LCs) may be targeted by molecular engineering of LC materials. In the absence of readily identifiable LCs expressing desired elastic properties, one may choose between synthetically altering moieties or exploring mixtures of existing mesogens. The latter is prominent in industry, with eutectic blends such as E7 often utilized [21, 56, 57]. These often broaden the nematic–isotropic (NI) transition or reduce the operating potential for LCDs by raising the dielectric constant anisotropy. The non-trivial nature of elasticity measurement makes it desirable to have a theoretical or computational approach that can provide deep insight into the underlying microscopic interactions and correlations reflected at a macroscopic scale.

While recent work [58] has examined the phase behavior of binary mixtures in the entropic limit as hard-sphere chain fluids, little work has explored the role of enthalpy in mixtures (though, cf. Refs. [59, 60]). Importantly, none of these investigations have studied the elastic response of mixtures, even though nematic elasticity is known to induce local phase segregation [61]. In this work, we utilize advanced Monte-Carlo sampling techniques applied to the multicomponent Lebwohl–Lasher (LL) model [62]. Mean field analogs, extended from Maier–Saupe theory by Palffy-Muhoray, have been shown to describe orientational behavior in real experimental systems in great
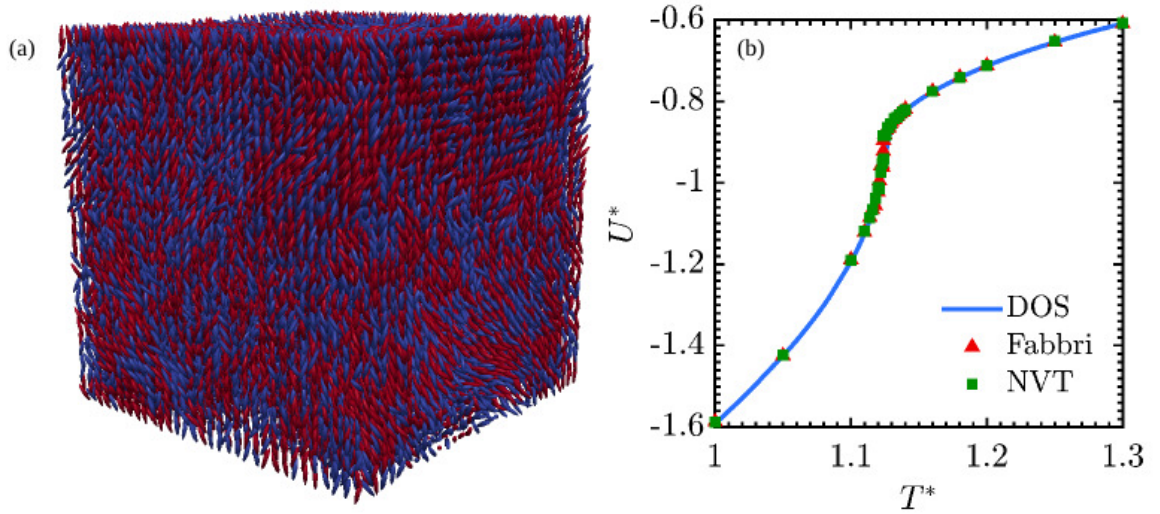
Figure 2.1. (a) Snapshot of a typical liquid crystal mixture at $x_B = 0.5$, $\epsilon_{AA}/\epsilon_{BB} = 0.4$ and $T/T_{NI}^B = 0.4$ for an $N = 32^3$ lattice. The composition at this temperature is homogeneous, as evidenced by the random distribution of A (red) and B (blue) species. (b) This system exhibits a phase transition at $T_{\mathrm{NI}}^* \approx 1.1229$, which may be calculated directly through targeted canonical ensemble (NVT) simulations [64] or through density-of-states (DOS) formalism [65]. We observe excellent agreement between these two methods.

detail [63]. We therefore expect the LL model, which incorporates fluctuations, to provide valuable molecular-level insight into ordering and elastic phenomena. The model is used to detail the phase diagrams and elastic behavior in binary mixtures of liquid crystals, representing a new framework for characterizing the properties of materials via comprehensive free energy sampling.

2.2 Lebwohl-Lasher Model

The LL model [62] is a lattice version of the Maier–Saupe description [18, 19] of nematic liquid crystals. The multicomponent Hamiltonian for these systems may be

phrased as

$$H = -\sum_{i,j} \epsilon_{\alpha\beta} P_2(\cos\theta_{ij}) \qquad (2.1)$$

where $\epsilon_{\alpha\beta}$ is the strength of interaction between nearest neighbors i and j (of species α and β, respectively), $P_2(x) = \frac{1}{2}(3x^2 - 1)$ is the second Legendre polynomial and $\cos(\theta_{ij}) = \hat{\mathbf{n}}_i \cdot \hat{\mathbf{n}}_j$ for nearest neighbors i, j. This model is incapable of treating steric interactions, and represents a simplified thermotropic model containing orientational entropy and enthalpic interactions. The NI transition occurs at $T_{\mathrm{NI}} = 1.1229\epsilon$ for a system with uniform composition ($\epsilon_{\alpha\beta} := \epsilon$) [66]. Elastic coefficients in the pure model are determined solely by the temperature $T^* = T/\epsilon$ for $T < T_{\mathrm{NI}}$. When two species are present (denoted A and B, where without loss of generality $\epsilon_{BB} > \epsilon_{AA}$), we utilize standard rules for polarization-driven interactions, resulting in $\epsilon_{AB} = \sqrt{\epsilon_{AA}\epsilon_{BB}}$. A typical configuration for this simplified model of binary nematic mixtures is given in Figure 2.1(a).

2.3   Simulation Details

2.3.1   Binary phase behavior

Traditionally, identifying phase boundaries in binary systems involves use of an ensemble which allows the composition to vary; on lattices this is often the semi-grand canonical ensemble which fixes the relative chemical potential $\Delta\mu$ of the two species. The choice of appropriate $\Delta\mu$ is guided by approximations and/or exploratory simulations. A series of simulations supplemented by histogram re-weighting techniques [67, 68] then obtains the coexistence chemical potentials. Alternatively, one may employ *flat-histogram* methods to sample phase space along the relative composition. Here, we adapt the multicanonical method of Wang and Landau [65]. As our interest is the equilibrium composition at a specific temperature, we choose the variables ($\Delta\mu = \mu_A - \mu_B$, $\Delta N = N_A - N_B$) relevant to the semi-grand canonical ensemble

7

(SGE). Our adaptation of the Wang–Landau algorithm allows direct evaluation of phase equilibria by sampling the partition function at each accessible composition, $Z(\Delta N)$.

The n-species semi-grand canonical partition function is [69]

$$\Xi' = \sideset{}{'}\sum_{\vec{N}} \left(\frac{q_1^N}{N!} \prod_{i=1}^{n} \left(\frac{q_i}{q_1} \right)^{N_i} \exp\left[\beta(\mu_i - \mu_r)N_i \right] \right) V^N \int d\mathbf{s} \exp\left[-\beta H(\vec{s}) \right] \qquad (2.2)$$

where q_i is the kinetic contribution to the partition function of species i, β is $1/k_BT$, μ_i is the chemical potential of species i, μ_r is an arbitrary reference chemical potential, $\vec{N} = (N_1, N_2..., N_n)$ is an n-tuple of populations with N_i the number of particles of species i, V is the system volume, H is the Hamiltonian of the mixture and $\mathbf{s}$ is the coordinate containing the classical degrees of freedom in the system, and the prime $'$ denotes that the sum is restricted by $\sum_{i=1}^{n} N_i = N$. This yields a probability

$$p(\mathbf{s}, N_i) \propto \exp\left[-\beta U(\vec{s}) + \sum_{i=1}^{n} (\mu_i - \mu_r)N_i \right] \qquad (2.3)$$

where μ_r an arbitrary reference chemical potential. Recognizing the Helmholtz free-energy F is related to Ξ' by [70]

$$F - \sum_{i=1}^{n} (\mu_i - \mu_r)N_i = -k_BT \ln \Xi' \ , \qquad (2.4)$$

permits the definition of a one-dimensional DOS biasing on the variable ΔN yielding an estimate $Z^{\text{est}}(\Delta N)$ of the relative weight for each composition state in Equation 2.3, resulting (up to an arbitrary constant) in an estimate of the Helmholtz energy $-\beta F^{\text{est}}(\Delta N) = \ln Z^{\text{est}}(\Delta N)$. Such a construction results in an acceptance probability

$$P_{acc} = \min\left(1, \frac{Z^{\text{est}}(\Delta N^{\text{old}})}{Z^{\text{est}}(\Delta N^{\text{new}})} \exp\left[-\beta \Delta H \right] \right) . \qquad (2.5)$$

Notably absent from this expression is $\Delta\mu$, highlighting the strength of this technique: no *a priori* estimate of the chemical potential is necessary—only post-simulation reweighing of the DOS is necessary to obtain the desired value.

The details of our bias updating and convergence schemes are consistent with previous methods described elsewhere [65, 71, 72]. In short, each simulation proceeds by randomly selecting a particle from the ensemble and performing either an identity swap move or a random rotation. After each trial move, $\ln Z^{\text{est}}(\Delta N)$ is updated with the final compositional state $\ln Z^{\text{est}}(\Delta N) \rightarrow \ln Z^{\text{est}}(\Delta N) + \ln f$, where f is a convergence factor. This process is repeated until the histogram achieves a flatness of 0.85, whereupon the convergence factor is updated to $f_{\text{new}} = \sqrt{f_{\text{old}}}$. We have defined flatness as the ratio $\min(\mathcal{H}(\Delta N))/\langle\mathcal{H}(\Delta N)\rangle_{\Delta N}$, with $\mathcal{H}$ the histogram of visited composition states. Simulations are halted when the convergence factor reaches $\mathcal{O}(10^{-8})$.

To accelerate DOS convergence, a multiple-window–multiple-walker implementation was used. The composition ΔN was evenly divided across windows with 50% overlapping regions. Individually converged segments were reassembled using a fourth-order central finite difference. Derivative errors at the joining point were typically on the order of 10^{-7} for high energy barrier points (low T) and as low as 10^{-9} along the nematic-isotropic coexistence regions. No replica exchange was necessary between windows, since at each composition ΔN, all of configurational space is accessible by the spins. This was validated by computing the mean absolute percentage error between a single-window/single-walker run and corresponding parallel version, which was 0.1291%, indicating a high degree of agreeability.

Equilibrium compositions at a particular β are obtained via re-weighing using the following relationship[73]:

$$P(\Delta N; \Delta\mu, \beta) \propto e^{-\beta F(\Delta N)+\beta\Delta\mu\Delta N} \tag{2.6}$$

Coexisting phases may then be obtained by performing a parameter sweep on $\Delta\mu$ using distribution data from the DOS simulations described above. Phase compositions are obtained using an equal-area construction applied to the resulting bimodal distributions, as illustrated in Figure 2.2. It is worth emphasizing that unlike other histogram reweighing techniques, the identification of μ_{eq} is exact to an accuracy proportional [74] to $\sqrt{f_{\mathrm{final}}}$ and the result of a single simulation and since the simulation spanned the entire composition space, the existence of a two phase region can be definitively known.
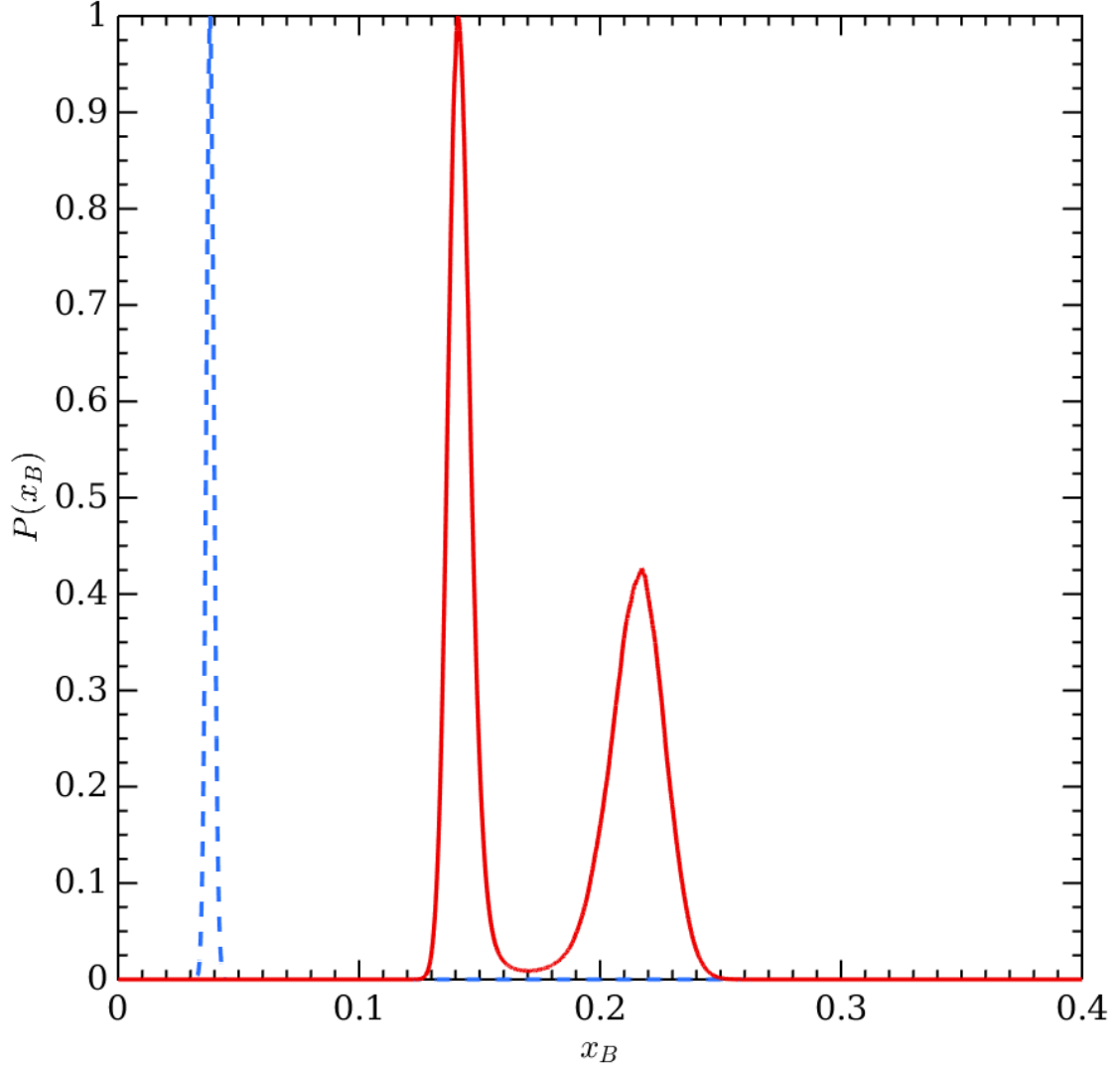
Figure 2.2. Probability distribution of a LL binary mixture with $\epsilon_{AA}/\epsilon_{BB} = 0.35$ at $T^* = 0.50$. The dashed blue line represents $P(x_B)$ at a starting guess of $\mu = 2.0$. Coexistence was identified by numerically determining the position of two peaks in probability, and automatically adjusting the chemical potential until the integrated areas under these peaks were equal. The solid red line represents that final value, $\mu_{\text{eq}} = 1.451$.

2.3.2 Elastic coefficient measurement

Mixture elastic coefficients were measured using a free energy perturbation approach first described for Gay–Berne systems and later applied (using polynomial expansion biases) to a pure LL system [75, 76]. For a uniaxial nematic, the elastic free energy density may be written in the Frank–Oseen form [34],

$$f_{FO} = \frac{1}{2}K_1(\mathbf{\nabla} \cdot \hat{\mathbf{n}})^2 + \frac{1}{2}K_2(\hat{\mathbf{n}} \cdot \mathbf{\nabla} \times \hat{\mathbf{n}})^2 + \frac{1}{2}K_3(\hat{\mathbf{n}} \times \mathbf{\nabla} \times \hat{\mathbf{n}})^2 \, , \qquad (2.7)$$

with K_1, K_2, and K_3 being the splay, twist and bend elastic constants. The Hamiltonian describing the LL model is fully rotationally symmetric with regard to global spin alignment—this permits deformation of one elastic mode into another, resulting in all three elastic constants being equal [77, 24]. This affords freedom in the choice of which elastic coefficient to measure. The equality of the three elastic modes are a special case of more generalized multiple–elastic constant models [24]. Following the methods derived in Ref. [75] and in keeping with previous investigations of pure species [77, 76], the K_2 (twist) mode was chosen as the deformation coordinate.

We chose to implement the expanded-ensemble DOS (ExEDOS) formalism [72] to calculate elastic free energies. The update is similar to Equation 2.5, with $Z^{\text{est}}(\Delta N)$ replaced by $Z^{\text{est}}(\xi)$, where ξ is the expanded ensemble coordinate (here, one representing twist deformation). Within this formalism, it is useful to consider the prefactor Z^{est} within the exponent as a biasing potential Φ, $\Phi = \ln Z^{\text{est}}$ [76], so that the biasing potential flattens the free energy surface, negating variations in F. Elastic constant simulations were performed on a $N = 32^3$ fully periodic system. The nematic director of the spins in the first layer of the box ($x = 0$) was constrained to the z-direction using P_2 of the dot product between this vector and each spin as the penalty function. The magnitude of the constraint potential was set to 10^5. Approximately 2^{17} canonical moves were then performed to relax the system. After

relaxation, DOS sampling began by creating an estimator with 200 bins with a twist order parameter range of $[-0.01, 0.01]$. The twist biasing potential was applied to the spins in the central layer ($x = 16$). The DOS convergence factor was initially set to 10^{-6}, a value commensurate with the estimated free energy difference due to a small perturbation in order parameter. A target flatness of 0.90 was used to achieve the desired accuracy. In accordance to the ExEDOS formalism, the final bias potential Φ equates to $-\beta F$. The elastic constant was extracted by fitting a quadratic form to this resulting free energy density surface using the relation $F = K\Phi^2/2$ [75, 76]. It was then normalized by the system volume and non–dimensionalized via $K^* = Ka/\epsilon$ where a is equal to the lattice spacing.

2.3.3   Externally applied stress

The elastic response of a bulk binary LC mixture under stress is modeled by an $N = 32^3$ lattice with varying composition, interaction potential ratio and temperature. An external field given by

$$U_{\text{field}} = -U_0 P_2(\hat{\mathbf{n}}_L \cdot \hat{\mathbf{d}}), \tag{2.8}$$

where $\hat{\mathbf{n}}_L$ is the local nematic director of a single layer of spins in the x direction and $\hat{\mathbf{d}} = (0, \sin\theta(x), \cos\theta(x))$ is the field director, augments the Hamiltonian to provide tunable elastic deformations within the simulation box. This penalty is applied collectively to a layer of spins with the same x position to retain fluctuations in the relative orientation of adjacent spins. U_0 is scaled accordingly as $U_0/(N_L\epsilon_{BB}) = 1$ where N_L is the number of spins in a layer; this corresponds to an orienting strength commensurate with spin-spin interactions.

To understand the response of our system to nonlinear deformations, we utilize nonlinear perturbations with a Gaussian form for the angle $\theta(x) \in [0, \pi]$ centered

about the lattice with $\sigma = 3a$; simple linear stresses may also be applied using a profile $\theta(x) = \pi x/L$. These simulations were performed in the NVT ensemble with the standard Metropolis[78] acceptance rule. Each iteration involved randomly selecting either a rotation move performed on an individual spin or an identity swap move where the species of two spins are exchanged. The local nematic director $\hat{\mathbf{n}}_L$ is computed each iteration for each x-layer from the order parameter tensor

$$\mathbf{Q} = \frac{3}{2N_L}\left[\sum_{i=1}^{N_L}\hat{\mathbf{u}}_i\hat{\mathbf{u}}_i - \frac{\boldsymbol{\delta}}{3}\right] \tag{2.9}$$

where $\hat{\mathbf{u}}_i\hat{\mathbf{u}}_i$ is the outer product of spin i with itself and δ is the Kronecker delta. $\hat{\mathbf{n}}_L$ is then taken as the eigenvector corresponding to the largest eigenvalue of $\mathbf{Q}$. Several short runs (10^5 sweeps) were performed with production runs of 10^7 MC sweeps.

2.3.4   Cylindrical confinement

Simulations of the LL mixtures under cylindrical confinement were carried out on an $N = 32^3$ cubic lattice. The cylinder was centered at $(x_0, y_0) = (15, 15)$ and spins with $R = \sqrt{(x - x_0)^2 + (y - y_0)^2} > 15$ were removed. Homeotropic anchoring was imposed on the spins comprising the boundary using a P_2 penalty function, with the constraint direction being $\hat{\mathbf{d}} = (x - x_0, y - y_0, 0)/\|R\|$. Numerical experiments were performed to choose the appropriate anchoring coefficient, striking a balance between the applied strength and suppression of local fluctuations; a value of 10^4 was chosen. Periodic boundaries were applied in the z–direction.

Each cylinder was initialized with spins pointing in the axial, radial and random directions to identify possible metastability due to initial configurations. All three initial configurations yielded identical results presented below. Production runs consisted of 2^{35} total moves, with directors and compositions averaged axially to yield the reduced composition and ordering data.

2.4 Results and Discussion

We begin by validating our DOS convergence algorithm, computing the NI transition of a single nematic species on $N = 32^3$ lattice with periodic boundary conditions; this transition has been previously studied extensively [79, 66], and as such provides a robust assessment of sampling and convergence criteria. We explicitly compare our results to those computed in Ref. [64] by sampling the density of states in energy $\Omega(U)$ for a single-component system [cf. Fig. 2.1(b)], obtaining exact agreement. We then proceed to apply DOS to binary mixtures, utilizing $N = 25^3$ sites. Though previous investigations had calculated the phase diagram for select energies [59], our method permits a comprehensive study, including nematic–nematic (NN) phase transitions at temperatures which are practically inaccessible with standard methods. These simulations were facilitated by implementing a multiple-window–multiple-walker algorithm [80]. Our results for $\epsilon_{AA}/\epsilon_{BB} = 0.4$ are given in Figure 2.3. Our results for the NI phase transition of this mixture in Figure 2.3 are consistent with those of Ref. [59]. The novel NN separation, which occurs in some polymer–nematic mixtures [81], has been previously predicted for LC mixtures by mean-field theory [82]. Interestingly, the critical region exhibits Ising-like behavior expected of unstructured binary liquid mixtures despite the presence of orientational fluctuations, though the mean-field theory is accurate at lower temperatures when compositional *and* orientational fluctuations become quenched.
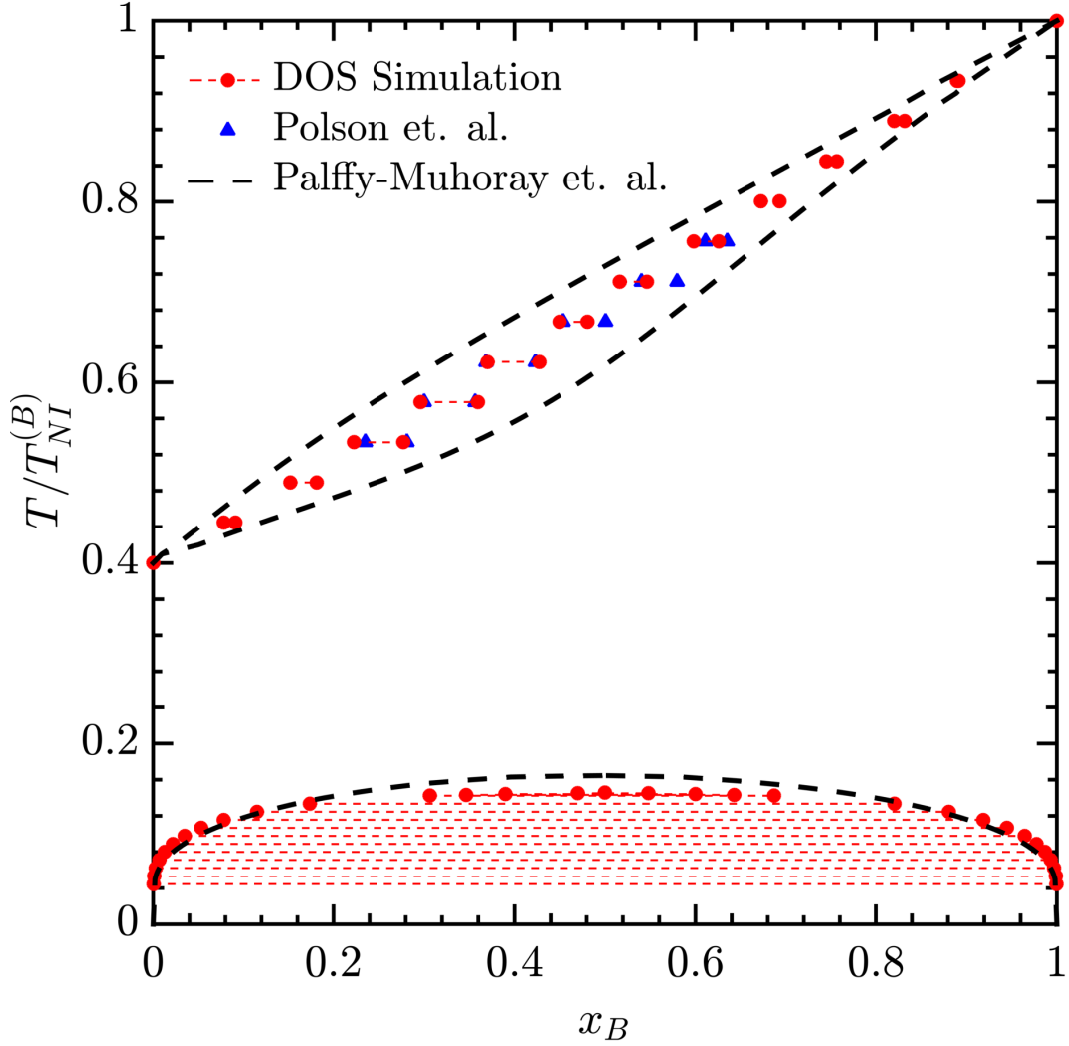
Figure 2.3. Extending the DOS approach to binary mixtures by sampling composition space N_A at a fixed β improves upon earlier findings [59], increasing accuracy in the NI coexistence region and permitting extension to the nematic–nematic (NN) coexistence region previously examined only in the mean-field limit [82].

Agreement with theoretical mean field predictions which have been confirmed by experiment [63] provides justification for studying LC ordering and elastic behavior

16

using the LL model. In fact, the mean field model shows agreement in order parameter and composition across the entire phase diagram, which we calculate below. The distinct advantage of our simulation approach is the ability to measure corresponding elasticities due to spatial inhomogeneity of the thee-dimensional lattice.

Expanding upon these results, Figure 2.4 presents phase diagrams at four representative values of $\epsilon_{AA}/\epsilon_{BB}$. Intriguingly, the resulting curves display both a widening of NI coexistence and an upwards shift of the NN regime as $\epsilon_{AA}/\epsilon_{BB}$ is decreased. At values of $\epsilon_{AA}/\epsilon_{BB} \lesssim 0.30$ these regions intersect, creating a vast two-phase region which restricts the existence of a single homogeneous nematic phase to the extremes in composition. This results in a curious feature where the system may transition directly from NN coexistence to NI coexistence through a temperature increase that induces demixing, promoting formation of a nearly-pure A-rich phase [cf. Fig 2.4(a)]. Such nearly pure phases are particularly interesting, representing LC media which have been doped by a miscible species. This suggests that mixtures containing disparate species are susceptible to phase separation under relatively small perturbations to the free energy, resulting in partial demixing. It is worth noting that latent heat effects have been shown to play a significant role in the kinetics of the NI transition [83, 84], consistent with experimental observations for pure LCs, where competition between free energy and curvature insufficiently describes the growth of a nematic nucleus. The combination of compositional segregation with the nematic–isotropic transition could lead to interesting effects in fast-switching materials near this boundary.
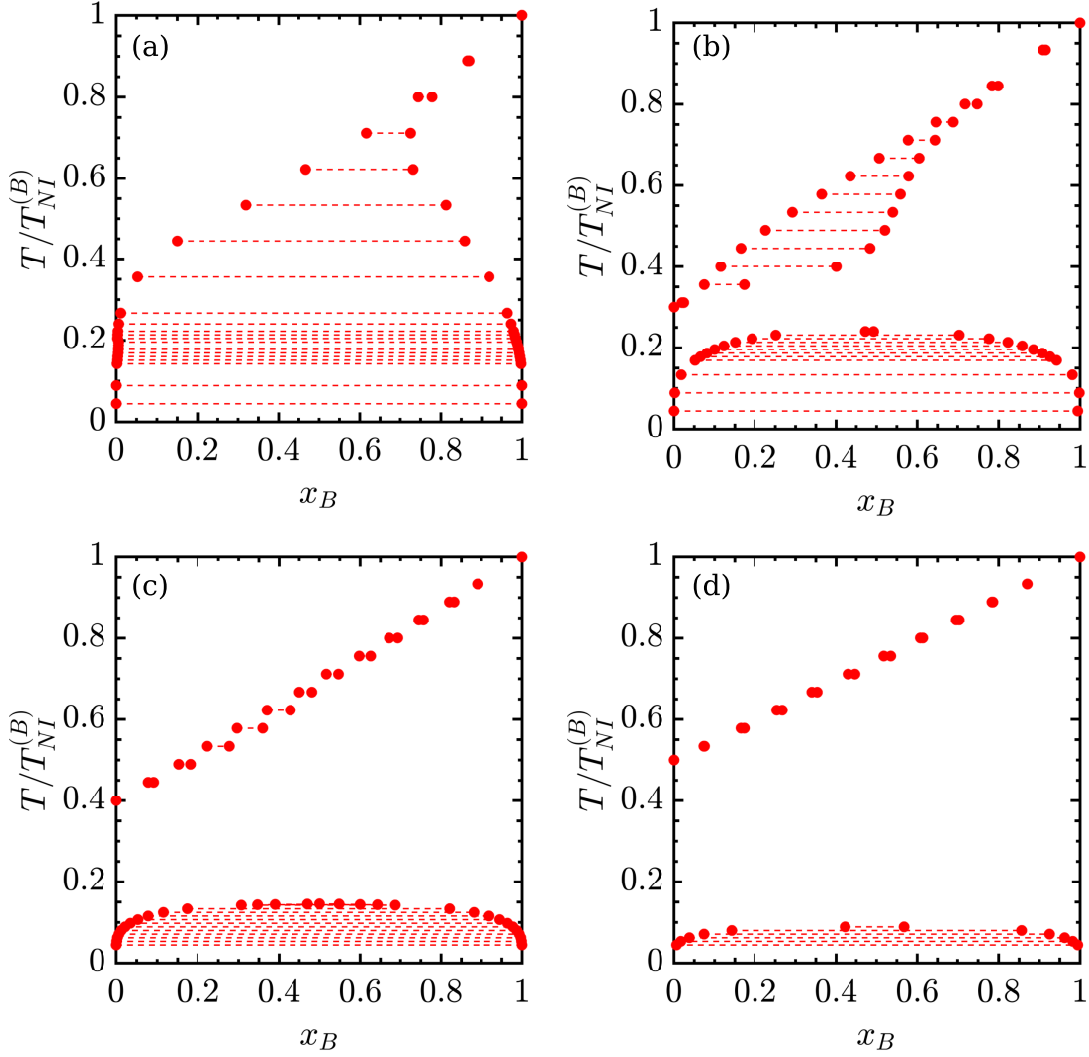
Figure 2.4. Lebwohl-Lasher lattice binary phase diagrams at $\epsilon_{AA}/\epsilon_{BB} =$ (a) 0.20, (b) 0.30, (c) 0.40 and (d) 0.50. Moderate values of $\epsilon_{AA}/\epsilon_{BB}$ (b)–(d) exhibit a continuous I-N region spanning between the pure-species transition points, with a homogeneous nematic phase giving way to A and B-rich phases at low temperature. Reducing $\epsilon_{AA}/\epsilon_{BB}$ causes broadening of the nematic–isotropic (NI) coexistence region towards x_B as a consequence of large asymmetry in interaction energy, which concomitantly promotes the nematic–nematic (NN) region to higher temperatures.

Kinetic pathways for the NI transition were previously studied in detail for the single-component LL model [66], with spinodal decomposition (SD) identified as the mechanism. Early–stage dynamics of SD in binary LC mixtures were also studied using a linearized time–dependent Landau-Ginzburg (LG) model [85]. It was found that SD was driven by concentration fluctuations within the isotropic spinodal curve while instabilities of the orientational order parameters induced SD outside the spinodal curve. Further investigations into the dynamics of phase transitions for LC–polymer mixtures using similar LG models identified possible isotropic-isotropic metastable coexistence buried below NI equilibrium [86]. Our density-of-states investigations are capable of obtaining both thermodynamically stable and metastable states. As our interest is in the equilibrium structure adopted by liquid crystalline mixtures under elastic stress, we have focused here on the stable binodal regions and the effects of interaction disparity between the LC species.

Molecular theory and experimental studies [87, 88] involving LC–nanoparticle mixtures have shown a significant broadening of the NI coexistence region, not unlike what is observed at low $\epsilon_{AA}/\epsilon_{BB}$. Furthermore, phase separation of homogeneous nematic phases are observed at low temperatures except for extremely low nanoparticle concentrations. The disparity in LC–nanoparticle interaction in addition to large isotropic attractions are highlighted there as dominant effects in phase separation. We will return to this result later when discussing the behavior of confined mixtures. For now, we utilize the NN coexistence curve to ensure we are examining mixtures in the homogeneous nematic state.
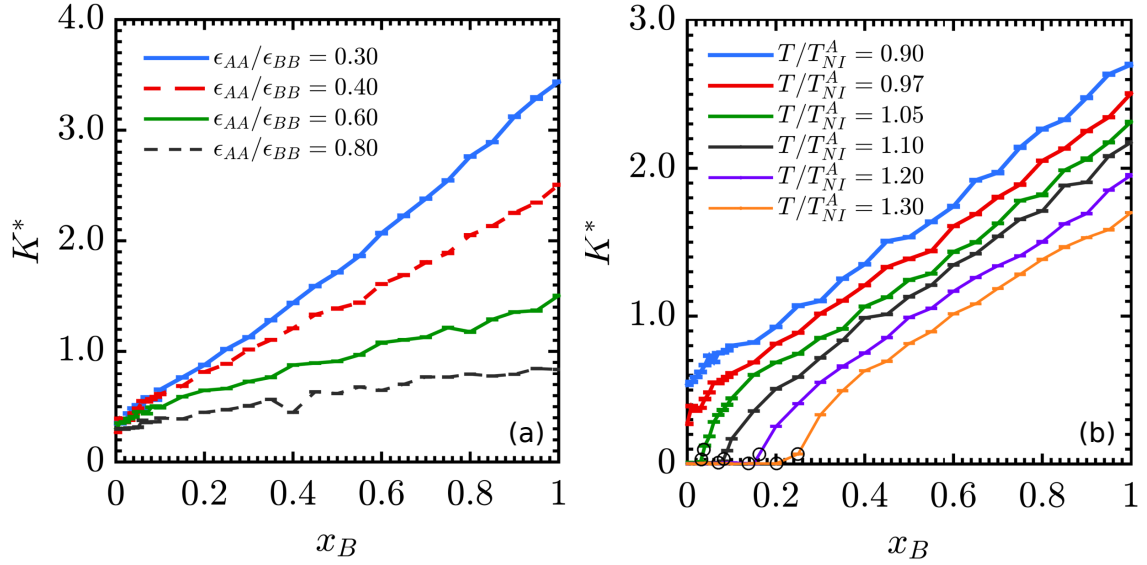
Figure 2.5. Elastic coefficient measurements performed using free energy perturbations as a function of composition (a) for $\epsilon_{AA}/\epsilon_{BB} = 0.30, 0.40, 0.60, 0.80$. Measurements are performed at a temperature T which is 97% of T_{NI}^A. The LL model exhibits an elastic response which is linear in composition over a wide range, suggesting that these systems retain uniform mixing [89] within the linear stress regime. In the region close to the NI transition nonlinear effects (b) become prominent. For $\epsilon_{AA}/\epsilon_{BB} = 0.40$ at temperatures between 90% and 130% of T_{NI}^A the elastic response exhibits a high degree of nonlinearity at low x_B. Coexisting compositions along each curve are represented by open circles.

We continue our free-energy mapping approach by applying the properties, we apply the expanded ensemble DOS algorithm (ExEDOS) to extract the parabolic free-energy profile associated with the twist elastic coefficient, as discussed in Section 2.3.2. The elastic coefficients of binary mixtures, obtained as a function of composition at $T/T_{NI}^A = 0.97$, are plotted in Figure 2.5(a) for a wide range of $\epsilon_{AA}/\epsilon_{BB}$. It is clear that LL mixtures exhibit elastic coefficients which follow linear mixing rules over the majority of compositions. Such mixing was previously noted to be consistent

with experiments on mixtures of the apolar mesogens 1PHCE5 and 5PBE01 [89], though it was indicated that to within experimental error, a quadratic form mixing rule also matched the data. It is likely that the linear mixing rules will be modified in practice for eutectic mixtures such as E7, which incorporate strongly interacting mesogens such as 5CT which are solid at room temperature and thus exhibit divergent elasticities. In particular, E7 is comprised of four species, three of which (5CB, 7CB, 8OCB) have a T_{NI} in the range 305 K–355 K, and a fourth (5CT) at 512K [90]. Such a mixture is effectively represented by a much lower value of $\epsilon_{AA}/\epsilon_{BB}$ where the quadratic form and measured elasticity vary significantly.

Exploring the model further, we also note a divergence from linearity in the $K^*(x_B)$ curve for mixtures near the NI coexistence region. These results are plotted in Figure 2.5(b). Specifically, we examine a system with $\epsilon_{AA}/\epsilon_{BB} = 0.40$ at temperatures ranging from $T/T_{NI}^A = 0.90$ to 1.30. At these temperatures, the initial phase may be nematic or isotropic; the coexisting values for x_B are denoted for each temperature studied. While zero elastic coefficient is expected (and observed) when either a homogeneous or coexisting isotropic phase is present, the elastic response is demonstrably nonlinear *after* the phase transition. The limit $x_B \approx 0$ is particularly relevant to cases where a more rigid species is added in nematogenic mixtures to raise the NI transition temperature, or increase elastic resistance [91, 92], thus a detailed understanding of this behavior is relevant for engineering applications.
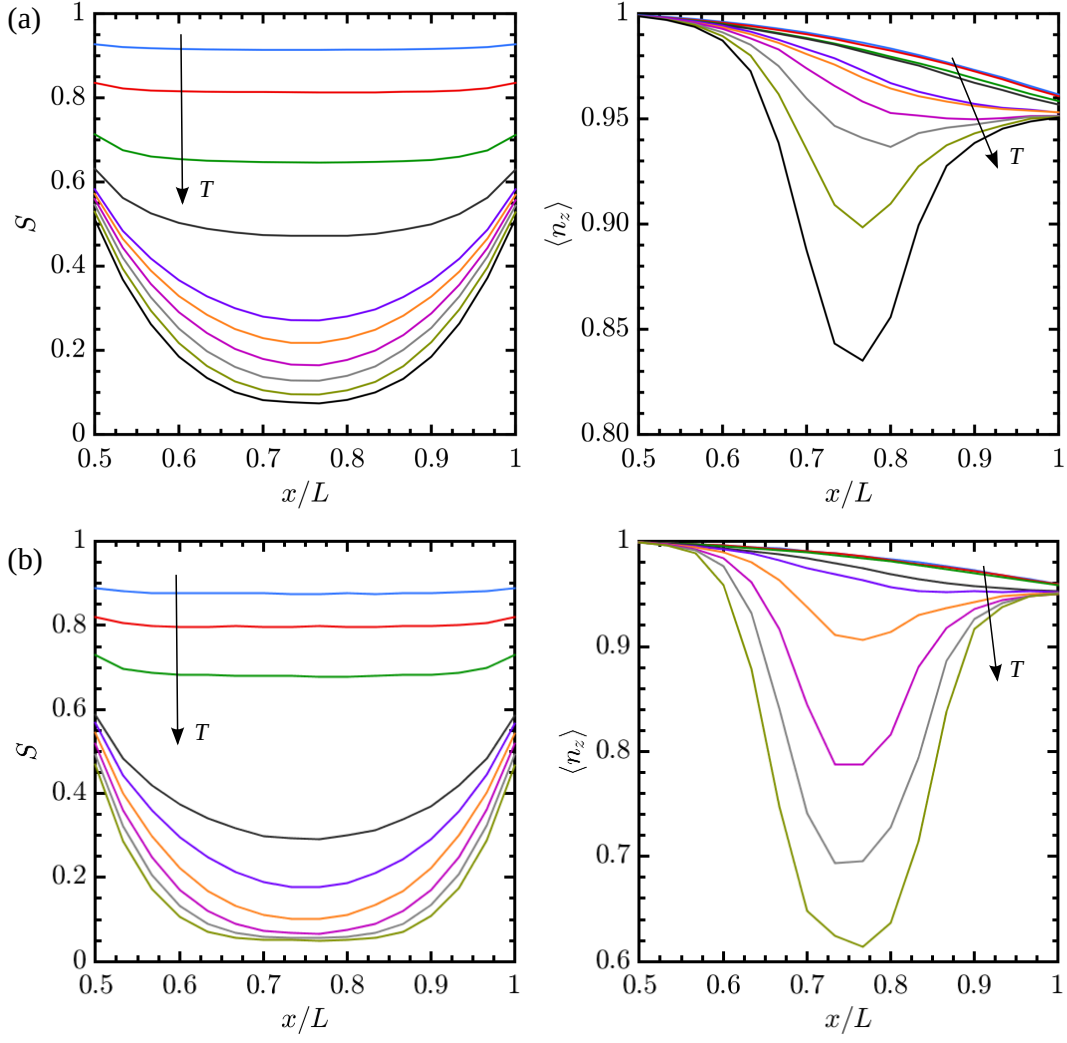
Figure 2.6. The dependence of the order parameter S and z-component of the layer director $\langle n_z \rangle$ on temperature at (a) $x_A = 0.5$ and (b) $x_A = 0.9$ for $\epsilon_{AA}/\epsilon_{BB} = 0.4$ in the presence of induced twist. The arrows indicate increasing temperature ranging from $T/T_{NI} = 0.4$ to 1.0 at each composition. The twist is applied to the central and periodic edge x-coordinate, with one symmetric half shown above (L here denotes the box length). As the temperature approaches T_{NI}, the twist no longer propagates across the length of the box and the profile of the director becomes highly nonlinear. This effect is responsible for the nonlinearity observed in the elastic coefficient measurements.

To ascertain the cause of the observed nonlinearity in elasticity, we induce a small twist in a $N = 32^3$ system with $\epsilon_{AA}/\epsilon_{BB} = 0.4$. The applied nematic director is set to $\hat{\mathbf{d}} = (0, 0, 1)$ at the center and $\hat{\mathbf{d}} = (0, \sin \pi/10, \cos \pi/10)$ at a periodic edge. For $x_A = 0.5$ and 0.9, canonical simulations are performed at various temperatures ranging $T/T_{NI} = 0.4$ to 1.0. Figure 2.6 plots one symmetric half of the systems and shows that for low temperatures, the twist, indicated by the z-component of the nematic director $\langle n_z \rangle$, is able to propagate from the center to the edges of the simulation cell. However, as the transition temperature is approached, this uniform profile can no longer be sustained due to increasing fluctuations, resulting in localized melting away from the applied stress induced by the field. The order parameters as shown in Figure 2.6(b) indicate near-complete disorder at the nonlinear conditions. This phenomenon can be thought of as a yield stress, wherein the deformation threshold is reached near the NI transition. The elastic constants, which measure a material's resistance to elastic deformation, exhibit a nonlinear decrease as a result.

One may inquire if elastic demixing extends in any way to homogeneous mixture compositions. While these are stable against small linear perturbations away from T_{NI}, areas exhibiting stronger deformations through nonlinear perturbations may recruit the weaker elastic species. We directly probe this by applying an external field potential as described by Equation 2.8.

Figure 2.7 shows the results of these calculations. For each interaction strength ratio, temperatures $T = \epsilon_{AA}$ were specifically chosen to be within the nematic state, but far from the NI and NN coexistence regions. Application of a Gaussian perturbation $\theta(x)$ with amplitude π and width $3a$ [cf. Fig. 2.7(a)] results in enrichment of the weaker-interacting A species within the regions of strongest elastic deformation. The nonlinear stress thus modulates local phase separation. Figure 2.7(b) shows that although compositional segregation becomes less pronounced as $\epsilon_{AA}/\epsilon_{BB}$ increases, there is still a significant orientational penalty in the high stress regions, resulting

in localized melting. This is affirmed by observing that the average absolute value of $n_z = \hat{\mathbf{n}} \cdot \hat{\mathbf{z}}$, which should approach zero when $\theta(x) = \pi/2$, instead melts into the random configuration $\langle |n_z| \rangle \approx 0.5$ [cf. Fig. 2.7(c)]. The dynamic response to stress through compositional and orientational means is a strong indication that the driving force is truly elastic in nature. The system would rather melt, paying substantial free-energetic costs to do so, than remain a homogeneous (but elastically deformed) fluid. Note that, though there is a slight enthalpic gain for phase separation, it is the entropic gain associated with mixing that dominates the bulk phase behavior. In the presence of a nonlinear elastic perturbation, the free energy penalty may be offset by partial demixing to gain enthalpy and the rotational freedom of localized isotropic fluid. In the absence of nonlinear deformations, this system is unable to perform such a balance.

We also explore the role of temperature in the segregation effects observed. Figure 2.8 shows that this phenomenon is insensitive to temperature. Simulations across a broad region of the homogeneous nematic regime show little change in compositional fractionation towards regions of high stress by the weaker elastic species. This further supports the elastically driven nature of the phase separation. Enthalpy dominated effects would certainly exhibit a significant change over a nearly two–fold increase in temperature. A removal of the field for the systems studied resulted in a restoration of the original homogeneous unperturbed state.
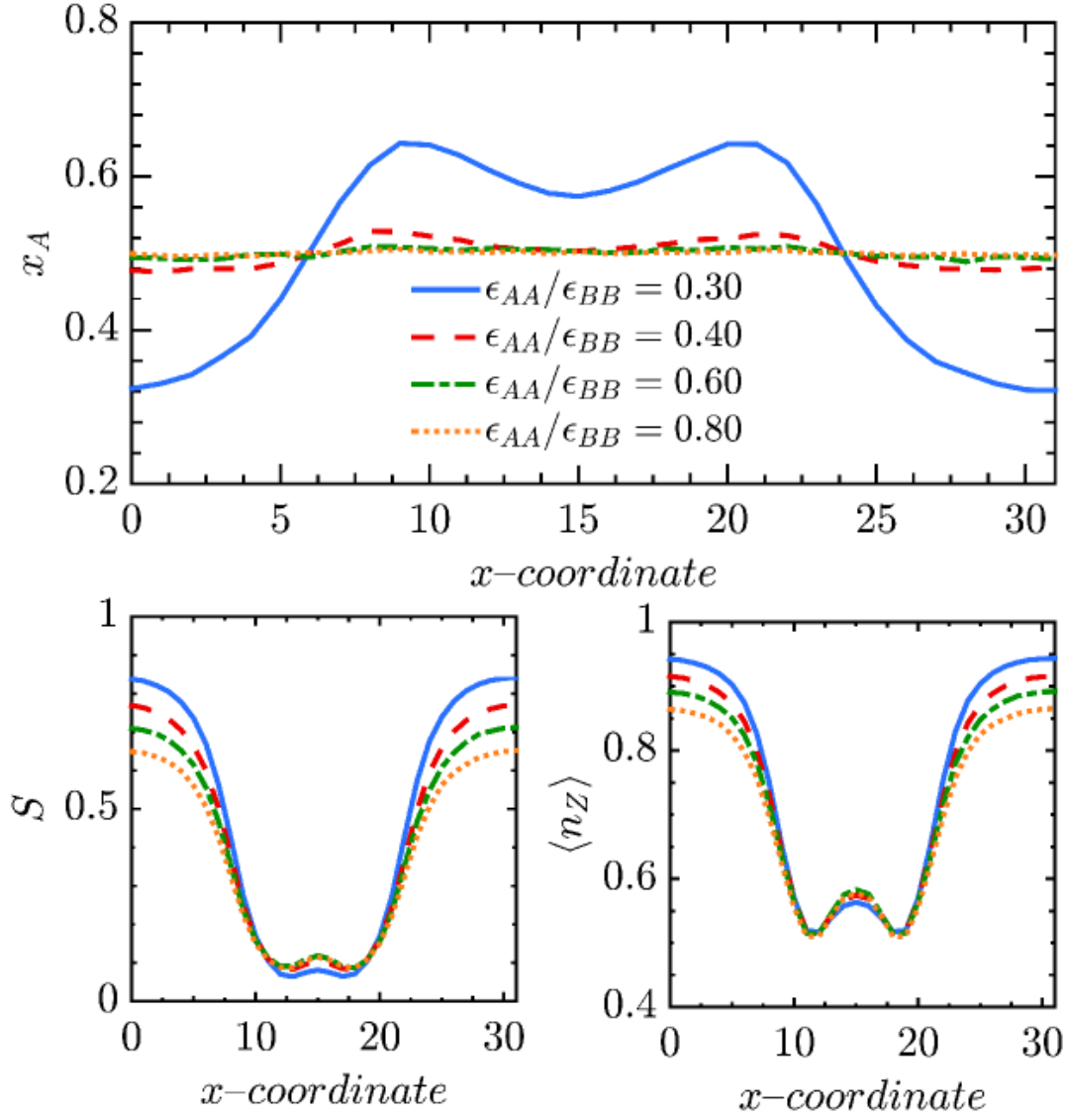
Figure 2.7. The presence of a nonlinear external field (a-c) induces segregation of a homogeneous nematic mixture. An applied Gaussian field influences the weaker elastic component to migrate to regions of high stress (a). This segregation is accompanied by decreasing nematic order (b) and disordering of spin orientations (c) [quantified by the nematic order parameter S and average absolute z component of the director $\langle n_z \rangle$ respectively], signifying apparent elastic melting near the highly deformed center layers. In all the systems studied here, the overall composition was $x_B = 0.5$.

Segregation effects are even more pronounced upon examining topological defect structures imposed on confined LC systems. For pure LC systems cylindrically confined with homeotropic anchoring, competition between bulk elastic and surface free energies can give rise to symmetry–breaking configurations. In particular, two $+1/2$ split core arrangements, known as planar–polar (PP), have been seen experimentally and shown to always be of lower free energy than alternate planar–radial disclinations provided that the defect structures have the same radii and $K_1 \approx K_3$ [41]; the latter condition is true for our LL model. Note that the PP designation is occasionally split [93] into versions which have disclinations within the LC phase, and those where anchoring is weak enough to merely distort the surface, expelling defects from the phase.
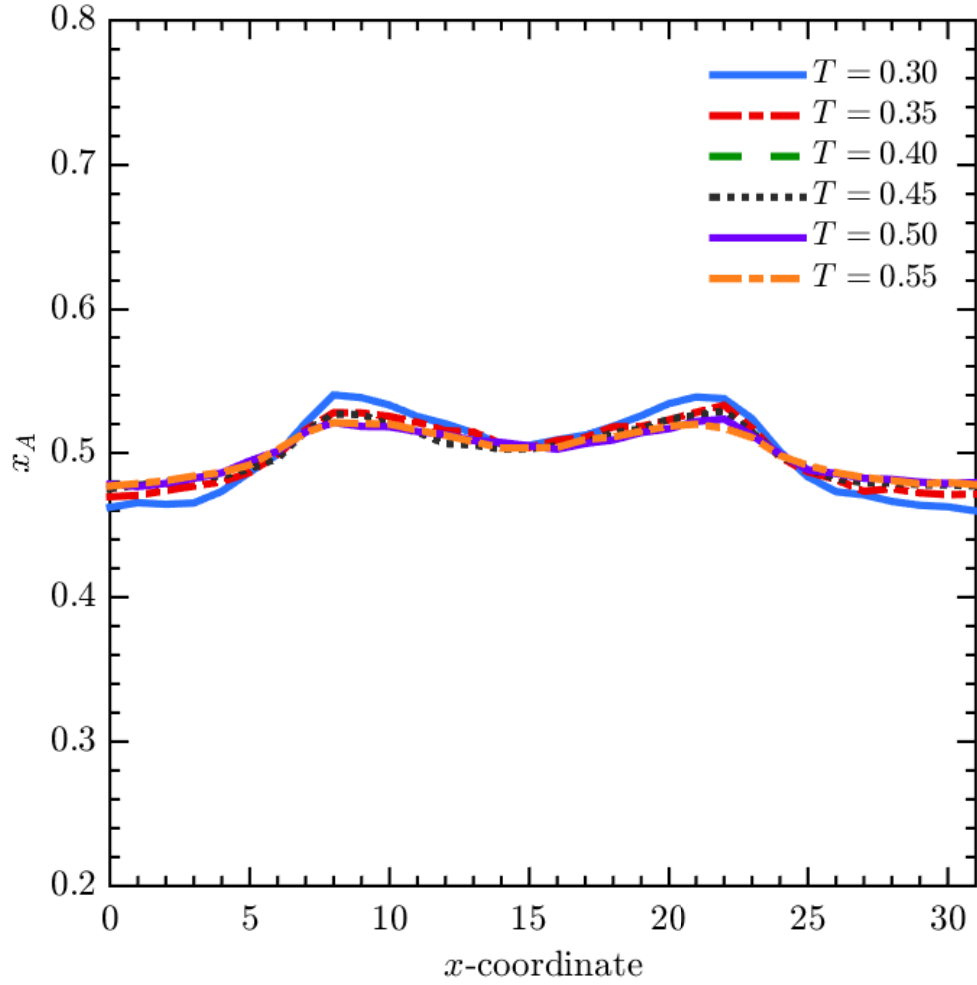
Figure 2.8. The compositional segregation resulting from external nonlinear stress responds weakly to changes in temperature. For $\epsilon_{AA}/\epsilon_{BB} = 0.40$ there is little change in profile of x_A throughout nearly the entire homogeneous nematic regime.

Numerical solutions to the dynamic alignment tensor equation in a (cylindrical) capillary show that the PP solution is favored over the planar–radial for all but the narrowest capillaries [95]. This configuration persists across almost the entire nematic
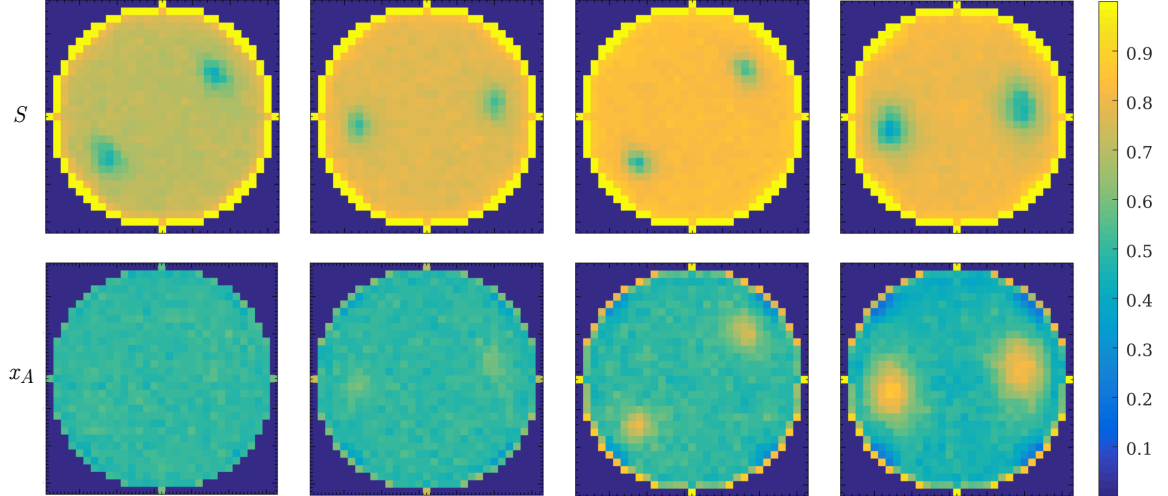
Figure 2.9. Under cylindrical confinement with homeotropic anchoring the system exhibits two $+1/2$ split core defects (from top: $\epsilon_{AA}/\epsilon_{BB} = 0.80, 0.60, 0.40, 0.30$). Such morphology agrees with that of Ref. [94] for pure systems. In all the systems studied here, the overall composition was $x_B = 0.5$.

region until the NI transition temperature. Computer simulations using the LL model for a single component nematic yielded planar-polar structures [94], as did molecular dynamics simulations of a rod-like model [93] for a variety of cylinder heights, radii and anchoring strength. The lack of an escaped radial configuration (ER) was later found to be due to surface extrapolation lengths exceeding bulk to surface energy ratios except at very low temperatures [96] (also, cf. [97]). Confined to concentric cylinders however, the LL model presented ER structure along the cylinder axis [98].

We simulate cylindrically confined binary LL mixtures and observe the formation of PP structures for various $\epsilon_{AA}/\epsilon_{BB}$, with $T = \epsilon_{AA}$, shown in Figure 2.9, consistent with results for single component systems. The presence of a secondary species introduces additional enthalpic competition to the existing bulk and surface contributions. This causes a migration of the weaker species A towards the defect cores. As the disparity of the mixture increases, the size of the A aggregates grow larger.

This effect is most prominent in mixtures with small $\epsilon_{AA}/\epsilon_{BB}$, but is present to some degree in all systems studied. The unique behavior of the binary system is that the order parameter at the disclinations remain $\approx 1/2$ despite variations in $\epsilon_{AA}/\epsilon_{BB}$ and temperature, enlarging to accommodate the increase in aggregation of A. As $\epsilon_{AA}/\epsilon_{BB}$ approaches unity, the single–component result [94] is recovered.
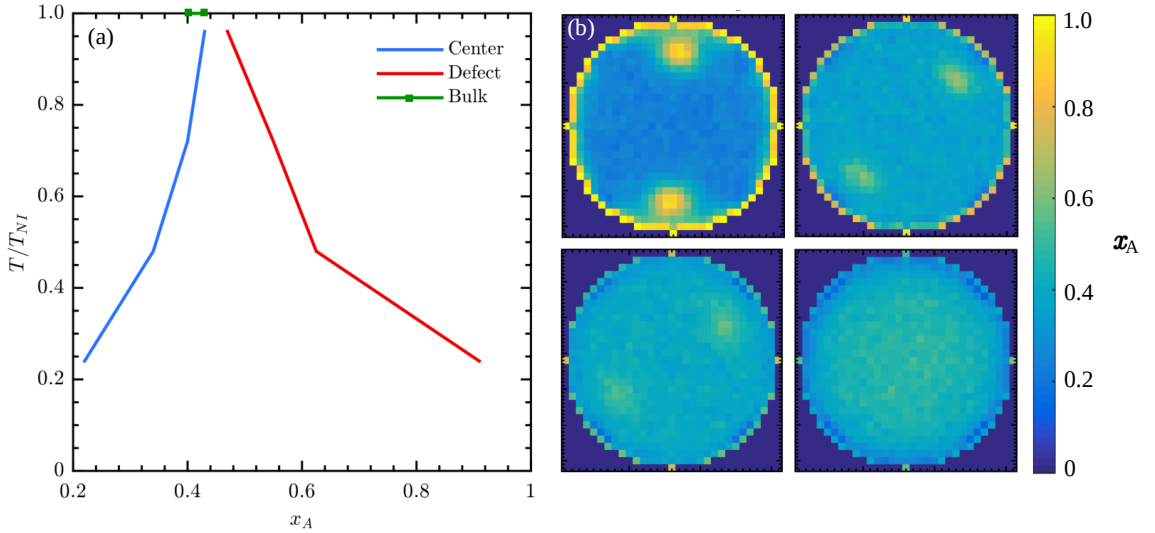
Figure 2.10. Compositions (a) taken from defect cores and centers for a binary system under cylindrical confinement at various temperatures with $\epsilon_{AA}/\epsilon_{BB} = 0.40$ and an overall composition of $x_B = 0.6$. As the NI transition is approached, the compositions at the center appears to approach isotropic bulk values obtained from Fig 2.4. However, at T_{NI} fractionation is no longer present in the system. Shapshots (b) at $T/T_{NI} = 0.24, 0.48, 0.72, 0.96$ (top left to bottom right) show the evolution of the PP defect towards a radial configuration near the transition temperature. The compositions at the center and defect cores are unique to cylindrical confinement, where a bulk system would reside well in the single phase nematic regime.

The fractionation present in the cylinders is studied in greater detail for $\epsilon_{AA}/\epsilon_{BB} = 0.4$. Compositions from the defect core and the center of the cylinder for species A are plotted against temperature in Figure 2.10(a). Approaching the transition, the system shifts from a PP to a radial configuration; data plotted at $T/T_{NI} = 0.96$ reflects this, and is obtained from the defect core at the cylinder's center and from an annulus at a radius 0.9 from the center of the cylinder. Both compositions exhibit a nonlinear temperature dependence which is enhanced approaching the NI transition. This temperature dependence is notably stronger in the defect cores compared to the center of the cylinder. Near the NI transition, the composition at the center appears to approach the isotropic bulk value obtained previously (cf. Figure 2.4), though these values are slightly offset within the cylinder due to surface effects in cylindrical confinement. As can be seen from snapshots of the cylinder in Figure 2.10(b), the compositional segregation disappears near T_{NI}. Concomitantly, we observe the split defect core of the plane polar morphology transforming into a single +1 disclination. This is characteristic of imposed stress relaxation by persistent localized melting, a phenomenon repeatedly shown previously. It is clear, then, that the presence of different elastically active species in the nematic phase has the potential to fundamentally alter the stress-induced morphologies relevant for sensing applications. Further, owing to the fact that the measured compositions in cylindrical confinement correspond to a single homogeneous region in bulk, and that the compositions are drastically different from their bulk two-phase region counterparts, we see direct evidence of a unique elastically-driven phase separation.

2.5   Conclusion

Utilizing DOS sampling, we were able to map out the entire phase diagram and and measure elastic constants of model binary liquid crystal mixtures. At low temperatures, nematic-nematic coexistence is observed, consistent with mean field pre-

dictions. Our results show that elastic segregation can be induced through a variety of different means. Near the NI transition, small linear perturbations are enough to cause melting, driving phase segregation and resulting in observed nonlinearity in elasticity. In the homogeneous nematic region, nonlinear stress is also found to cause localized melting and segregation which is largely independent of temperature; this effect is reversible. Finally, cylindrical confinement presents two $+1/2$ split core defects which cause enrichment of the weaker elastic species at the defect cores and associated melting. At temperatures approaching the transition temperature, the symmetry breaking disclinations give way to a radial configuration with homogenized composition. All three distinct stresses give rise to similar responses characteristic of elastically driven behavior.

These results have the potential to affect many developing areas of liquid crystal technology. For instance, elastic segregation effects have profound implications for systems with a small component of 'dopant' species exhibiting stronger or weaker elasticity added to alter response behavior in many industrial blends. Further, we expect induced compositional differences to be particularly relevant for nanoparticle self-assembly or templated polymerization where defects may be used to guide the formation of complex heterostructures. Colloid in liquid crystal gels, for instance, are known to exhibit an enhanced NI transition temperature relative to bulk LC, consistent with segregation of weak elastic species to surface-mediated defects [99]. These effects might even be exploited to enhance the relative solubility of included species for templated defect regions. Compositional differences also have the potential to significantly affect the stability of liquid-crystalline droplets where topological defects play a significant role. This is due to their delicate surface–bulk interplay, which may enhance the molecular recognition of sensors through selective solvation within surface defects.

31

CHAPTER 3

ELASTIC PROPERTIES OF COMMON GAY–BERNE NEMATOGENS FROM
DENSITY-OF-STATES SIMULATIONS

3.1   Introduction

The unique ordering properties of liquid crystals imbue these materials with novel
electrical, mechanical or optical properties, and are key to several emerging appli-
cations [8, 27, 100, 101]. While there remains much interest in the use of liquid
crystals in displays [102, 34], self-assembly [100, 103, 14, 10, 104, 15, 105–109] and
molecular sensing [110, 3, 111–114, 8, 7, 115] have received substantial interest re-
cently. Topological defects formed by surface interactions with embedded colloidal
particles have been used to create gel-like liquid-crystalline materials and ordered
arrays of microspheres [99, 116, 11]. Assembly is driven either by defects on the
colloidal surface, which attract in order to minimize elastic deformations, or by the
desire of a liquid crystal to partially alleviate the elastic stress and imposed melting
at nematic disclinations or smectic boundaries [117, 118, 104]. The nature and struc-
ture of these defects, and thus the subsequent assemblies, are controlled by elastic
properties. Molecular sensing applications have demonstrated exquisite sensitivity
to bacterial toxins by controlling the interplay of surface and bulk forces within a
liquid crystalline film or in droplet confinement [7, 8]. Much of this work utilizes
nematogenic cyanobiphenyls (in particular 5CB), though these methods could make
use of the any nematogenic system.

As the elastic properties of LCs play a key role in their function, it is impera-
tive that molecular models accurately capture not only molecular sizes and ordering

properties, but also the elastic behavior crucial to real-world applications. Here, our primary interest is in the coarse-grained modeling of uniaxial nematics through the Gay–Berne (GB) potential [119, 20]. Despite widespread use, little is known about the elastic properties of individual models, which makes understanding their applicability to real systems challenging. In particular, though a few GB potentials have been parameterized to match the interaction properties of real nematogens [120, 121], GB models have largely been used primarily to generate a "typical" nematic medium, devoid of molecular specificities and often having some unphysical features such as a significant density difference between nematic and istropic phases [28]. As new applications can depend on a sensitive balance of the elastic coefficients, it is imperative to elucidate their properties.

While use of the Gay–Berne potential is widespread, measurements of the nematic elastic coefficients have focused primarily on the well-characterized (3, 5, 2, 1) model (utilizing the notation of Bates and Luckhurst [122], explained further below) [123, 75, 124], though a few notable exceptions exist[125, 124]. Here, we will examine four additional models for measuring the elastic coefficients in nematic liquid crystals, using free-energy perturbation methods [75]. Each of the models examined was chosen for a particular reason, and all but one lacks significant elastic characterization. The (3, 5, 1, 2) model, primarily studied when augmented with a chiral interaction term, where it may be used to form cholesteric, blue, and chiral smectic phases within a coarse-grained model. The (3, 5, 1, 3) model [126], which broadens the nematic range relative to the (3, 5, 1, 2) model, and has been used in studies of LC adsorption onto graphite surfaces [127], also represents the only model other than (3, 5, 1, 2) to receive significant elastic characterization [123, 124]. The (4.4, 20, 1, 1) [122] model, derived from a parameterization for p-terphenyl, has been used to study important surface–elastic properties in confinement. Finally, the (0.345, 0.2, 1, 2) parameterized for a triphenylene core [121] is a common discogen used to study systems exhibiting

nematic and columnar phases [128], and is closely related to models proposed to function as model chromonic liquid crystals [129].

Our results, which utilize a recently developed density-of-states formalism [75], obtain elastic coefficients within each model for significant portions of the nematic range from the isotropic phase to the more highly ordered smectic or columnar phases. We find very good agreement between our elastic measurements for the (3, 5, 1, 3) model and previous measurements [124]. Our results are further able to demonstrate that the (4.4, 20, 1, 1) model represents an exceptional coarse-grained model for liquid crystalline systems—in particular it matches the elastic ratios of p-azoxyanisole, and presents a solid foundation upon which representations of cyanobiphenyls may be developed. This work serves to present a base-line understanding of the elasticity of Gay–Berne models and to inform and systematize their application to modeling real liquid-crystalline systems.

3.2 Gay–Berne Potential

The Gay–Berne (GB) potential [119, 130, 20] is an anisotropic generalization of the standard 12–6 Lennard–Jones potential describing the short range interactions of uniaxial ellipsoidal particles. The ability to tune the aspect ratio and potential asymmetry has made it widely used to model liquid crystalline systems. Various generalizations of the original model exist [131, 132], one of which [133] overcomes the numerical difficulties associated with capturing both oblate and prolate spheroids simultaneously. The GB interaction between two particles i and j may be written as

$$U_{GB}(\hat{\mathbf{u}}_i, \hat{\mathbf{u}}_j, \hat{\mathbf{r}}_{ij}) = 4\epsilon(\hat{\mathbf{u}}_i, \hat{\mathbf{u}}_j, \hat{\mathbf{r}}_{ij}) \left[R^{12} - R^6 \right] \tag{3.1}$$

where $\hat{\mathbf{u}}_i$ is the orientation of particle i, $\hat{\mathbf{r}}_{ij}$ is the distance vector between particles i and j, and R approximates the surface to surface distance by

$$R = \frac{d_w \sigma_0}{r_{ij} - \sigma(\hat{\mathbf{u}}_i, \hat{\mathbf{u}}_j, \hat{\mathbf{r}}_{ij}) + d_w \sigma_0} \tag{3.2}$$

with the range parameter $\sigma(\hat{\mathbf{u}}_i, \hat{\mathbf{u}}_j, \hat{\mathbf{r}}_{ij})$ having the form

$$\sigma(\hat{\mathbf{u}}_i, \hat{\mathbf{u}}_j, \hat{\mathbf{r}}_{ij}) =$$
$$\sigma_0 \left[1 - \left\{ \frac{\chi \alpha^2 (\hat{\mathbf{u}}_i \cdot \hat{\mathbf{r}}_{ij})^2 + \chi \alpha^{-2} (\hat{\mathbf{u}}_j \cdot \hat{\mathbf{r}}_{ij})^2 - 2\chi^2 (\hat{\mathbf{u}}_i \cdot \hat{\mathbf{r}}_{ij})(\hat{\mathbf{u}}_j \cdot \hat{\mathbf{r}}_{ij})(\hat{\mathbf{u}}_i \cdot \hat{\mathbf{u}}_j)}{1 - \chi^2 (\hat{\mathbf{u}}_i \cdot \hat{\mathbf{u}}_j)^2} \right\} \right]^{-\frac{1}{2}} \tag{3.3}$$

where

$$\chi = \left[\frac{(l_i^2 - d_i^2)(l_j^2 - d_j^2)}{(l_j^2 + d_i^2)(l_i^2 + d_j^2)} \right]^{1/2}, \tag{3.4}$$

and

$$\alpha^2 = \left[\frac{(l_i^2 - d_i^2)(l_j^2 + d_i^2)}{(l_j^2 - d_j^2)(l_i^2 + d_j^2)} \right]^{1/2}. \tag{3.5}$$

Here, d_w describes the "softness" of the potential which allows for appropriate scaling of oblate spheroids and l and d are the length and diameter of each particle respectively. In general, d_w is set to 1, though it is customary in discotic models to use it to shorten the range of face–face interactions. We note that although σ_0 is commonly defined as $\sigma_0 = \sqrt{d_i^2 + d_j^2}$ for mixed-particle systems, we choose to use the arithmetic mean $\sigma_0 = (d_i + d_j)/2$ and omit a factor of $\sqrt{2}$ for like particles, in keeping with standard treatments for the diameters of identical species.

The total molecular anisotropic potential is calculated as

$$\epsilon(\hat{\mathbf{u}}_i, \hat{\mathbf{u}}_j, \hat{\mathbf{r}}_{ij}) = \epsilon_0 \epsilon_1^\nu (\hat{\mathbf{u}}_i, \hat{\mathbf{u}}_j) \epsilon_2^\mu (\hat{\mathbf{u}}_i, \hat{\mathbf{u}}_j, \hat{\mathbf{r}}_{ij}) \tag{3.6}$$

36

where ϵ_0 is the well depth of the cross configuration. The orientation dependent strength terms are calculated as follows:

$$\epsilon_1(\hat{\mathbf{u}}_i, \hat{\mathbf{u}}_j) = \left[1 - \chi^2(\hat{\mathbf{u}}_i \cdot \hat{\mathbf{u}}_j)^2\right]^{-1/2}, \tag{3.7}$$

$$\epsilon_2(\hat{\mathbf{u}}_i, \hat{\mathbf{u}}_j, \hat{\mathbf{r}}_{ij}) =$$
$$1 - \left\{ \frac{\chi'\alpha'^2(\hat{\mathbf{u}}_i \cdot \hat{\mathbf{r}}_{ij})^2 + \chi'\alpha'^{-2}(\hat{\mathbf{u}}_j \cdot \hat{\mathbf{r}}_{ij})^2 - 2\chi'^2(\hat{\mathbf{u}}_i \cdot \hat{\mathbf{r}}_{ij})(\hat{\mathbf{u}}_j \cdot \hat{\mathbf{r}}_{ij})(\hat{\mathbf{u}}_i \cdot \hat{\mathbf{u}}_j)}{1 - \chi'^2(\hat{\mathbf{u}}_i \cdot \hat{\mathbf{u}}_j)^2} \right\} \tag{3.8}$$

where

$$\chi' = \frac{1 - (\epsilon_E/\epsilon_S)^{1/\mu}}{1 + (\epsilon_E/\epsilon_S)^{1/\mu}}, \tag{3.9}$$

$$\alpha'^2 = \left[1 + (\epsilon_E/\epsilon_S)^{1/\mu}\right]^{-1}. \tag{3.10}$$

The parameters ϵ_E and ϵ_S refer to the potential well depths of the end–to–end and side–to–side configurations for prolate spheroids respectively. For oblate spheroids, ϵ_E is often replaced with ϵ_F representing a face–to–face configuration and ϵ_S is referred to as ϵ_E for the edge–to–edge configuration. For clarity and consistency, we use the former notation throughout. Variables μ and ν are adjustable parameters with typical values of 2 and 1 respectively. In keeping with Ref. [133], the terms $\chi\alpha^2$, and $\chi\alpha^{-2}$ are treated as inseparable to avoid imaginary numbers for arbitrary aspect ratios and are computed as

$$\chi\alpha^2 = \frac{l_i^2 - d_i^2}{l_i^2 + d_j^2}, \tag{3.11}$$

$$\chi\alpha^{-2} = \frac{l_j^2 - d_j^2}{l_j^2 + d_i^2}. \tag{3.12}$$

It is convenient to define the ratios $\kappa = l/d$ and $\kappa' = \epsilon_S/\epsilon_E$ which permits the use of the compact notation [122] $(\kappa, \kappa', \mu, \nu)$ to fully describe the GB model, a convention which is used throughout this paper. Reduced units are adopted, with distance r scaled as $r^* = r/\sigma_0$, density ρ as $\rho^* = N\sigma_0^3/V$, temperature T as $T^* = k_B T/\epsilon_0$, energy U as $U^* = U/\epsilon_0$, pressure P as $P^* = P\sigma_0^3/\epsilon_0$ and elastic constants k_{ii} as $k_{ii}^* = k_{ii}\sigma_0/\epsilon_0$.

3.3   Studied Models

One apparent drawback of the original $(3, 5, 2, 1)$ GB model is the narrow nematic range [134]. By choosing $\mu = 1$ and $\nu = 2$, Luckhurst et al. [135] proposed the $(3, 5, 1, 2)$ model which stabilized side–side interactions and generated nematic phases with a wider temperature rage. This parametrization has since been used as the the basis for chiral LC models [136, 137] and the subject of further characterization in bulk and under confinement [138], and is the first model we study in this work. A closely related model, the $(3, 5, 1, 3)$ model proposed by Berardi et al. [126] supports an even wider nematic range. As its elastic properties have characterized for a sampling of configurations [123, 124], this serves as further testing and validation for free-energy perturbation methods.

Explicit parameterization of the GB potential to a model mesogen, p-terphenyl was initially undertaken by Luckhurst and Simmonds [120] where the biaxiality of a site–site potential was projected out into a $(4.4, 39.6, 0.80, 0.74)$ uniaxial GB model. This was later simplified to a $(4.4, 20, 1, 1)$ potential [122] while retaining the rich isotropic, nematic, smectic A and smectic B phase behavior. Further investigations of the model have characterized the nematic–isotropic (NI) transition in detail [139], structural dynamics [140], looked at behavior under nano–confinement [141] and in an aligning field [142, 143] and importantly, studied the Fréedericksz transition of the nematic phase [125]. The explicit mapping to a mesogen and the extensive

characterization makes it a suitable model which we have chosen to study.
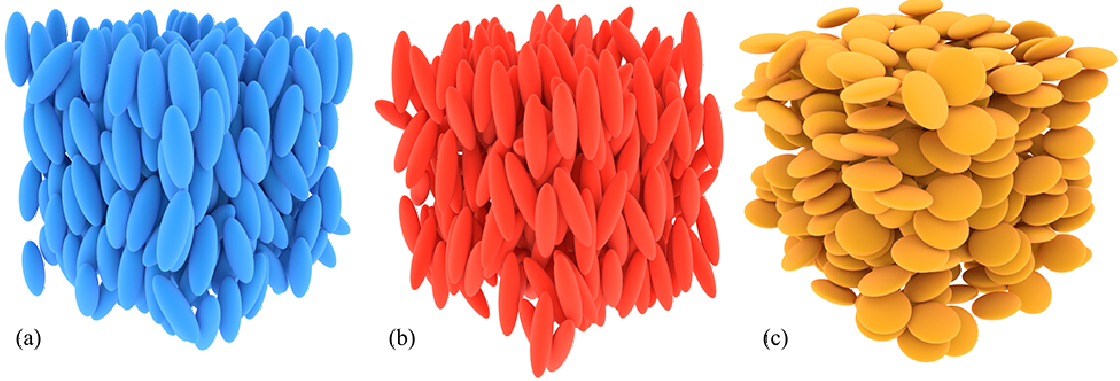
Figure 3.1. Snapshots showing representative nematic configurations for the Gay–Berne models (a) (3, 5, 1, 2) at $\rho^* = 0.301$, (b) (4.4, 20, 1, 1) at $\rho^* = 0.193$ and (c) (0.345, 0.2, 1, 2) at $\rho^* = 2.360$ with $S \approx 0.65$. The corresponding T/T_{NI} are approximately 0.87, 0.75 and 0.83 respectively. The (3, 5, 1, 3) model is visually indistinguishable from the (3, 5, 1, 2) model, and thus not shown.

A discotic GB potential was parameterized to a triphenylene core by Emerson et al. [121] with phase equilibria, structure and diffusivity exhaustively characterized more recently [128]. The system was found to exhibit isotropic, nematic, and disordered and ordered columnar phases. The resulting model was a (0.345, 0.2, 1, 2) GB potential. To our knowledge, no attempt has been made to measure the elasticities of discotic LCs in simulation. Therefore, a characterization of the elastic constants is a logical addition to the experimentally relevant model. Representative configurations for the (3, 5, 1, ν), (4.4, 20, 1, 1) and (0.345, 0.2, 1, 2) models are shown in Figure 3.1.

3.4   Methods

Density of states (DOS) flat histogram methods are a powerful class of Monte Carlo sampling algorithms capable of directly measuring free energies along defined order parameters. Examples include Wang–Landau sampling [65] which was later generalized to arbitrary expanded ensembles (ExEDOS) [72], basis function sampling [76] and more recently Green's function sampling [144]. Continuous analogs of these methods include metadynamics [145] and adaptive biasing force [146]. Utilizing the expanded ensemble formalism, the probability of observing a specific point along an order parameter ξ is proportional to $Q_\xi(N, V, T, \xi)$, the expanded canonical partition function at particular point [73]. To generate a flat histogram along ξ, we define a biasing function $\eta(\xi)$ which yields the probability

$$p(\xi) \propto Q_\xi(N, V, T, \xi) \exp[-\eta(\xi)]. \tag{3.13}$$

A choice of $\eta \equiv \ln Q_\xi = -\beta F(\xi)$, with $F(\xi)$ the associated Landau free energy, results in uniform sampling with respect to ξ. In this work we make use of an expanded–ensemble density of states (ExEDOS) generalization of the Wang–Landau scheme [72, 65] in determining $\beta F(\xi)$ where ξ is an elastic deformation coordinate chosen to extract the Frank elastic constants. Our order parameter is based on the free energy perturbation method proposed by Joshi et al. [75] who used metadynamics to measure the elastic constants of the (3, 5, 2, 1) GB model. However, we perform our simulations in Monte Carlo utilizing the expanded ensemble formalism previously described. Our current approach is similar to other Monte Carlo adaptations used to measure elastic coefficients of the lattice-based Lebwohl–Lasher model in pure [76] systems and binary mixtures [147].

Several other methods have been proposed to measure elastic constants in simulation. Cleaver and Allen [77] determined the elastic constants of the Lebwohl–Lasher

model using long wavelength director fluctuations and by direct simulation of the Fréedericksz transition. The latter method is noted [77] to be unreliable, subject to relatively high errors, and particularly sensitive to inhomogeneous finite size effects. The fluctuation approach is much more reliable but requires accurate statistics from large simulation boxes. Allen and co-workers adopted this method in Refs. [123] and [124] to measure elasticities of the (3, 5, 2, 1) and (3, 5, 1, 3) GB models. Stelzer et al. [148, 149] used orientation dependent direct correlation functions to infer the elastic constants of the (3, 5, 2, 1) GB model. However, the numerical complexity involved in performing the exact calculation limits the versatility of this method [150]. Luckhurst et al. [125] simulated the Fréedericksz transition for the (4.4, 20, 1, 1) GB model and extracted the elastic constant at a single state condition. The method is difficult to control, with potential inaccuracies due to confinement induced effects on the scalar order paramter, S. By contrast, the DOS method of Ref. [75] has excellent agreement with previously published works, and permits accurate determination of elastic coefficients in relatively small systems.

The DOS method requires definition of a suitable coordinate to sample deformations relevant to the Frank–Oseen free energy (see Eq. 1.1). For small deformations applied to a system aligned in the z–direction, we choose the DOS order parameter ξ as follows [75]:

$$
\begin{aligned}
\text{splay} &: \xi := \partial n_x / \partial x \\
\text{twist} &: \xi := \partial n_y / \partial x \\
\text{bend} &: \xi := \partial n_x / \partial z
\end{aligned}
\tag{3.14}
$$

where n_x, n_y and n_z are the Cartesian components of the local nematic director. In practice, we define a DOS sampling region of finite length βL_i, where L_i corresponds to the box vector along the deformation, in the plane orthogonal to that direction. An

equally sized region spanning the periodic box edge is used to restrict orientations of the global director, $\hat{\mathbf{n}} = \hat{\mathbf{z}}$. For example, the sampling region for splay would include all mesogens within the region $x \in [L_x/2(1 - \beta), L_x/2(1 + \beta)]$ and the restriction region would be $x \in [0, \beta L_x/2] \cup [L_x(1 - 1/2\beta), L_x]$; we take $\beta = 0.2$ in all of the following work. To compute the appropriate gradient from Eq. 3.14, we calculate the nematic director in the sampling region using the tensor order parameter

$$\mathbf{Q} = \frac{3}{2N} \left[\sum_{i=1}^{N} \hat{\mathbf{u}}_i \hat{\mathbf{u}}_i - \frac{\boldsymbol{\delta}}{3} \right], \tag{3.15}$$

where N is the number of mesogens in the sampling region; for this representation $\hat{\mathbf{n}}$ is the eigenvector associated with largest eigenvalue S, which quantifies the degree of nematic ordering within the system. This allows us to define the splay order parameter as

$$\xi = \frac{n_x}{L_x/2}. \tag{3.16}$$

An important distinction between our implementation and that described in Ref. [75] is the explicit use of the local nematic director in sampling the order parameter, and the slight difference in choice of anchoring, facilitated by Monte Carlo sampling. Our application of the restriction region involves using a penalty function defined using the second Legendre polynomial $P_2(x)$,

$$U_{\text{restrict}} = U_0 P_2(\hat{\mathbf{n}} \cdot \hat{\mathbf{d}}), \tag{3.17}$$

with $\hat{\mathbf{d}} = (0, 0, 1)$, and $\hat{\mathbf{n}}$ computed over the entire restriction region. This contrasts with the Lagrange multiplier restrictions on Q_{xz} and Q_{yz} implemented previously by Refs. [123] and [75]. With the appropriate choice of anchoring coefficient U_0, this approach is equally valid.

For each GB model, we begin by selecting an appropriate pressure and correspond-

ing density at which to measure the elastic constants. Our aim is to select conditions with a wide nematic range over which the elastic constants may be probed. NPT Monte Carlo simulations are carried out to equilibrate the systems. Translations, rotations and volume scaling moves are performed with the standard Metropolis acceptance criteria [69], optimized to achieve $\approx 60\%$ acceptance which we found to be optimal for enhanced DOS sampling. After stabilization of ρ and S, an additional 1 million sweeps are carried out to fully relax the system. The final configurations are used as initial conditions for restriction-free NVT simulations measuring S. These simulations are run for 10 million MC sweeps each at different temperatures across the nematic range after an equilibration period of 1 million MC sweeps. The nematic order parameter thermodynamic average S is calculated from independent configurations as the largest eigenvalue of Eq. 3.15.

Each DOS simulation is then carried out at constant NVT starting from a state obtained from the output of the previous calculation, and utilize 12 independent walkers [80]. The chosen order parameter (see Equation 3.14) is discretized into 500 bins. An equilibration period of 3×10^5 sweeps, during which no updating of the bias occurs, permits equilibration of the global orientation $\hat{\mathbf{n}}$ to $\hat{\mathbf{z}}$. After equilibration, in accordance with Eq. 3.13, the biased acceptance rule becomes

$$P_{\text{acc}} = \min\left(1, \exp[-\beta \Delta U - \Delta \eta(\xi)]\right). \tag{3.18}$$

After each trial move, the estimator $\ln \eta(\xi)$ is updated with the final state $\ln \eta(\xi) \to \ln \eta(\xi) + \ln f$ where f is a convergence factor. Each walker synchronizes with the global bias and histogram at 200 sweep intervals. This proceeds until a running histogram $H(\xi)$ of visited states achieves a chosen flatness, defined as $\min(H(\xi))/\langle H(\xi) \rangle_\xi$, of 0.90, after which the histogram is reset. The initial value of f is set to 10^{-5} for all systems studied, and simulations are complete when f reaches $\mathcal{O}(10^{-9})$. The average

43

number of MC sweeps required to achieve convergence for the systems studied was
$\approx 15 \times 10^6$.
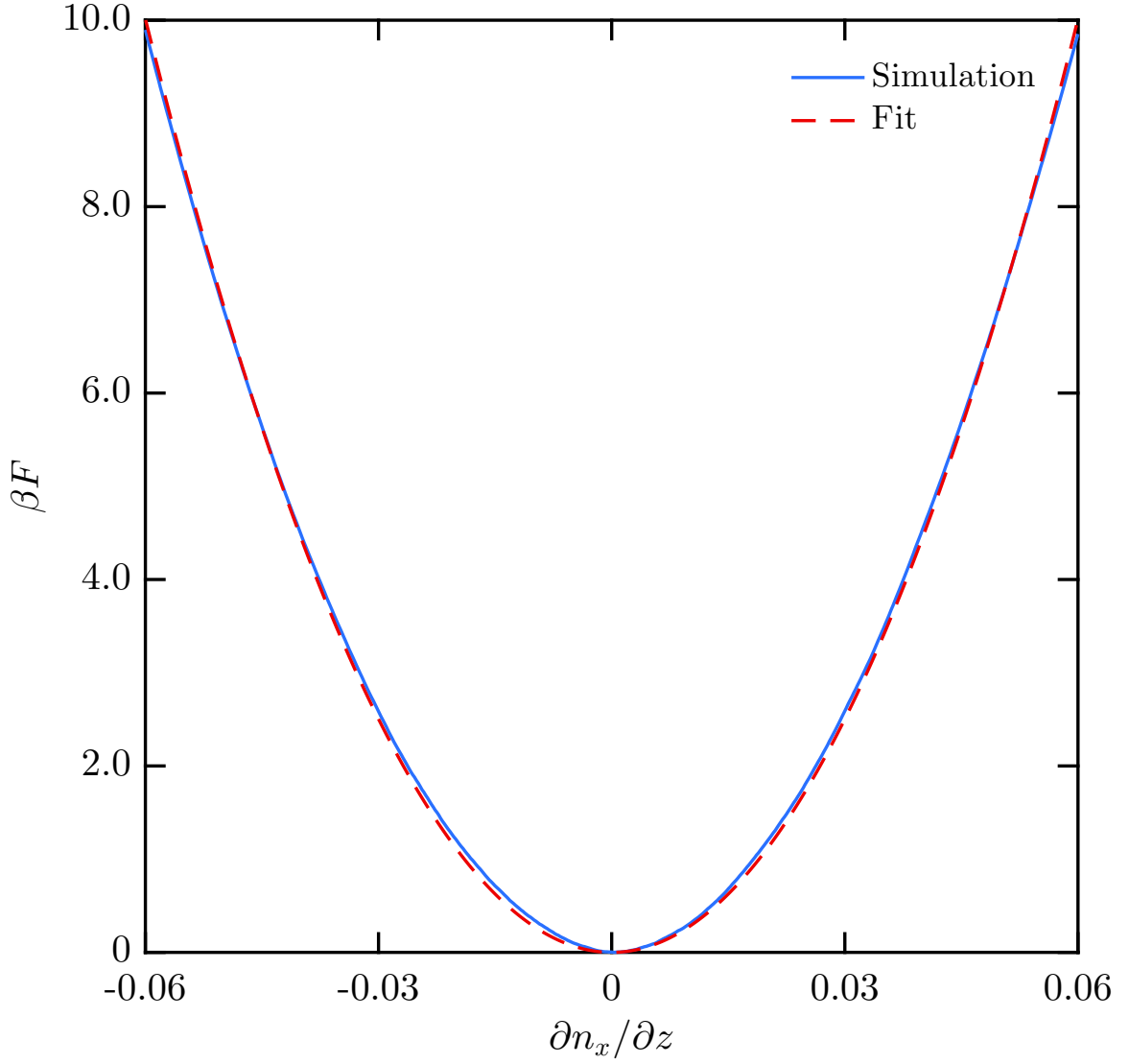
Figure 3.2. Representative parabolic free energy profile obtained using the DOS method described compared to a least squares fit. The bend elastic constant (cf. Eq. 3.14) is calculated using Eq. 3.12. This measurement was performed on the (3, 5, 2, 1) GB model at $\rho^* = 0.338$ and $T^* = 1.0$.

The resulting estimator $\ln \eta(\xi)$ corresponds to a high fidelity approximation of the parabolic free energy profile $\beta F(\xi)$ of the splay, bend or twist order parameter. Figure 3.2 shows a typical parabola derived via the aforementioned method. The elastic constant k_{ii} is then obtained by a least squares fit of the following expression, representing the excitation of a single elastic mode,

$$F = \frac{1}{2} k_{ii} \left(\frac{1}{1 - 2\beta} \right) \left(\frac{\partial n_i}{\partial x_j} \right)^2 V. \tag{3.19}$$

Here k_{ii} is the elastic constant of interest, $1/(1 - 2\beta)$ is a correction factor for the finite restriction region and V is the box volume [75]. A detailed discussion of finite region effects can be found in Ref. [75]. We use the value specified earlier, $\beta = 0.2$, to define our restriction region. To ensure that the anchoring coefficient is sufficiently large, we measure k_{33} of the (3, 5, 2, 1) GB model with a cutoff radius of $5\sigma_0$ at $T^* = 1.00, \rho^* = 0.338$ for increasing values of U_0. Figure 3.3 shows the evolution of k_{33} as a function of Monte Carlo sweep. It is apparent that the k_{33} value saturates for U_0 between 10^3 and 10^4, thus the latter was chosen for the remainder of the simulations. The measured k_{33} is also in good agreement with the results obtained in Ref. [75] near the smectic–nematic transition where we obtain $k_{33} = 3.3$ compared to ≈ 3.8 at $T^* = 1.0$ and $k_{33} \approx 3.2$ at $T^* = 1.05$ reported there. This small difference is likely due to the use of a different cutoff radius; Ref. [75] used the larger value $r_{\text{cut}} = 6\sigma$, which would slightly enhance cohesive forces (and thus elastic constants) relative to our calculation.
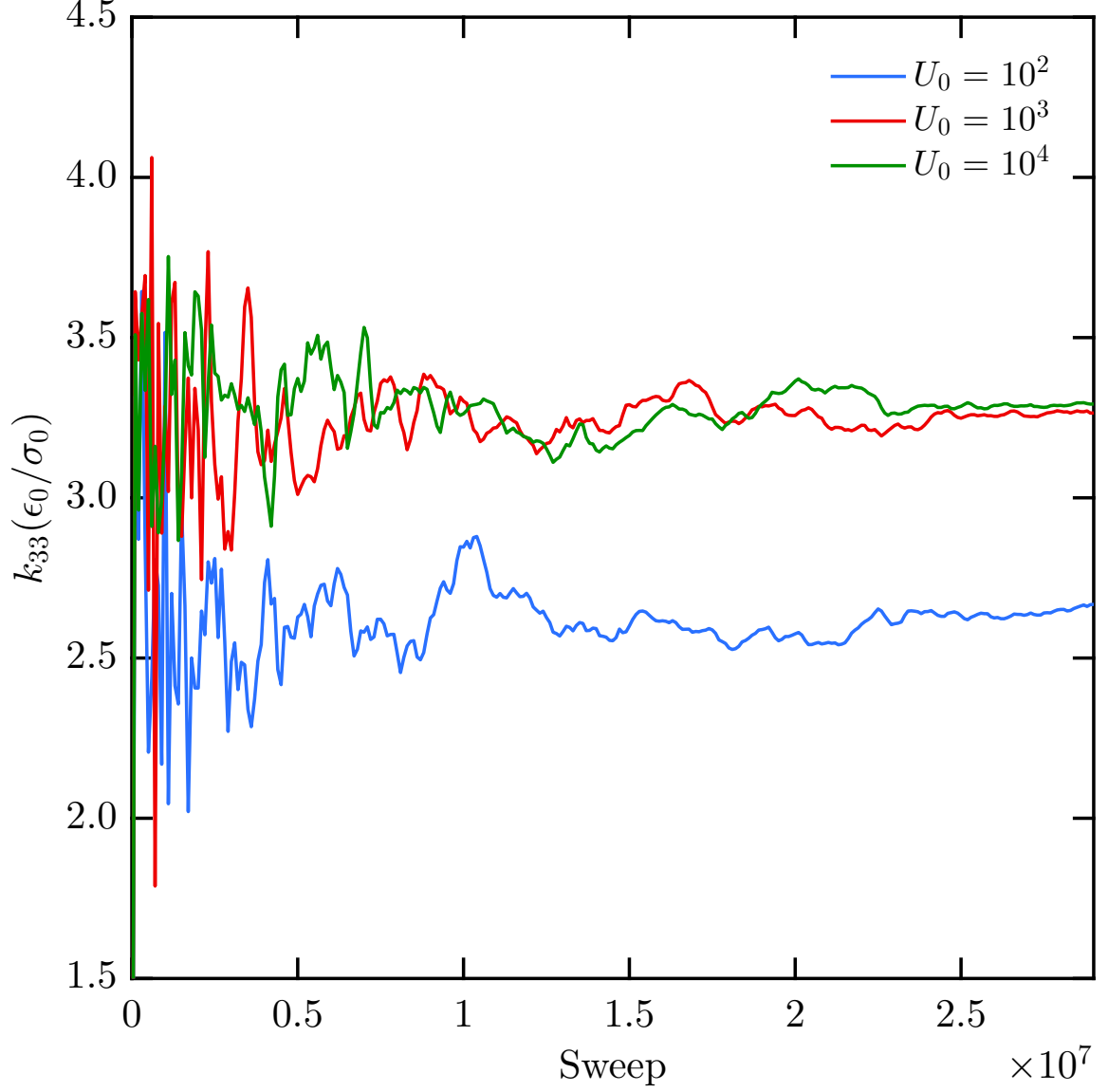
Figure 3.3. Evolution of k_{33} over time for various anchoring strengths, U_0. The measured elastic constant stabilizes between 10^4 and 10^5 indicating that the mesogens in the slab region are sufficiently constrained. Data was collected for the (3, 5, 2, 1) GB model at $\rho^* = 0.338$ and $T^* = 1.0$, and is in good agreement with Ref [75].

We chose $N = 338$ for all measurements carried out unless otherwise stated. Joshi

et al. [75] previously investigated finite size effects and determined that they are minimal for elastic constant measured in the nematic phase, which is the focus of this study. Uncertainties in the elastic constants are obtained by computing the standard deviation of the averaged k_{ii} over the sweeps at the final convergence factor. Independent values are taken every 10,000 sweeps to ensure de–correlated measurements.

3.5 Results and Discussion

After verifying our methods against the (3, 5, 2, 1) GB model, we turn our attention to four other GB models previously described: the (3, 5, 1, 2) model of Luckhurst et al. [135], the (3, 5, 1, 3) model of Berardi et al. [126], the (4.4, 20, 1, 1) parameterization of p-terphenyl [120, 122] and the (0.345, 0.2, 1, 2) triphenylene core discotic model [121]. Table 3.1 lists the densities and temperature ranges at which the elastic constants were measured for each potential. All simulations were performed using SAPHRON, [151] an open–source Monte Carlo molecular simulation engine.

TABLE 3.1

DENSITIES AND TEMPERATURES OF GAY–BERNE MODELS
STUDIED IN THIS WORK.

GB potential	ρ^*	T^*_{min}	T^*_{max}	Reference(s)
(3, 5, 1, 2)	0.301	1.50	2.50	Ref. [135]
(3, 5, 1, 3)	0.300	2.80	3.70	Refs. [126, 124]
(4.4, 20, 1, 1)	0.193	3.00	7.00	Ref. [122]
(0.345, 0.2, 1, 2)	2.360	2.60	5.00	Refs. [121, 128]

47

The (3, 5, 1, 2) model ($r_{cut} = 5.0\sigma_0$) is studied at a density of $\rho^* = 0.301$, which is close to the previous elastic studies [75, 123, 124] of the (3, 5, 2, 1) potential. However, this model presents a broad smectic phase which transitions into a nematic at a much higher temperature. The volumetric phase diagram in Ref. [138] shows the presence of smectic–A and smectic–B phases near the nematic at the density investigated here, but at lower temperatures. Elastic constants for this model at $\rho^* = 0.301$ are presented in Figure 3.4. They appear to exhibit a linear temperature dependence throughout the nematic phase, dropping off at the NI transition. The measured k_{11} and k_{22} are largely indistinguishable with k_{33} being significantly larger in magnitude. The k_{33}/k_{11} ratio, and by extension k_{33}/k_{22}, narrows as S decreases, not unlike the observed behavior for the (3, 5, 2, 1) [75] model. In fact, the general trends between the two models are similar, though the temperature dependence of the elastic constants in the (3, 5, 1, 2) model is more pronounced.
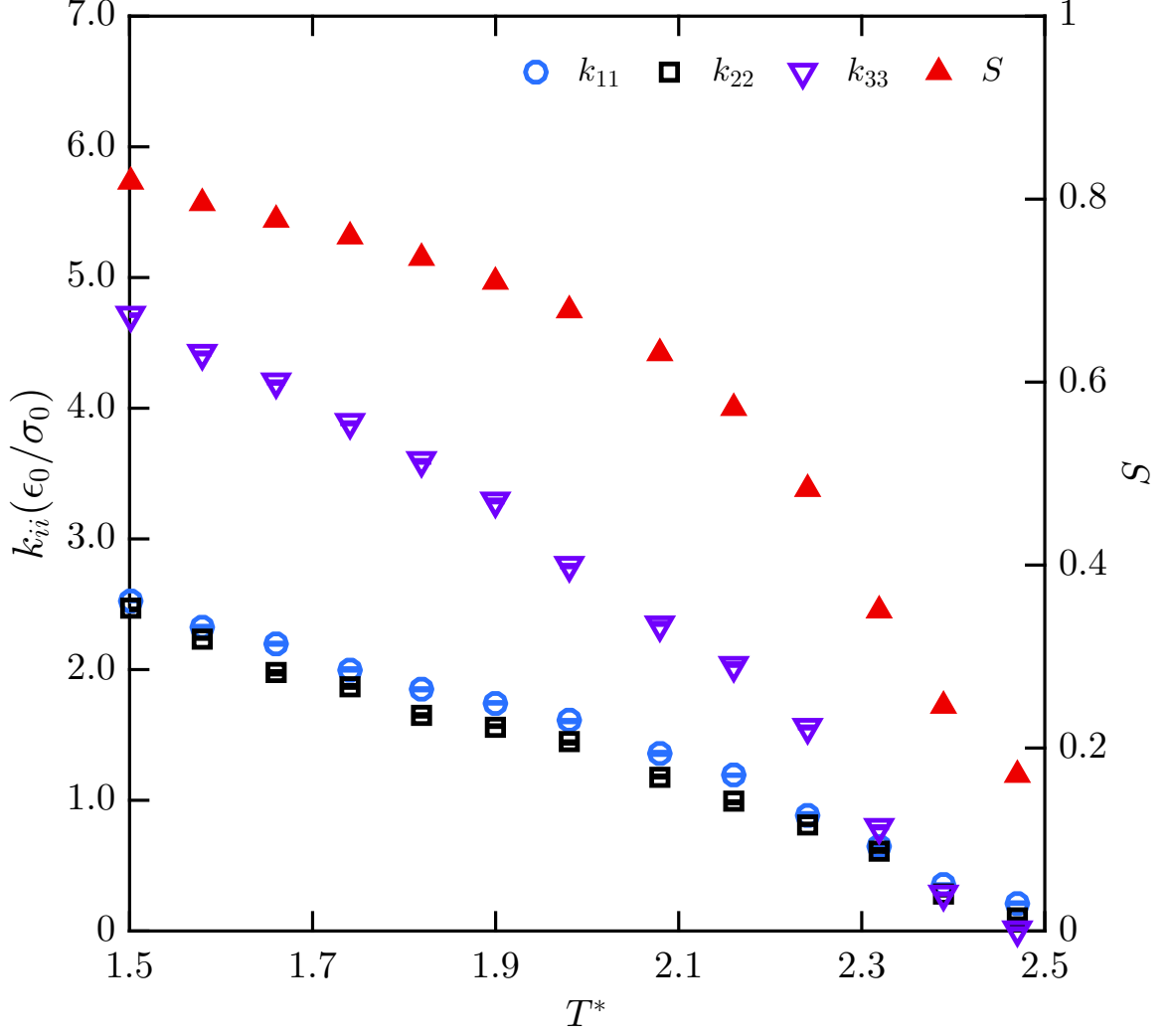
Figure 3.4. Splay, bend and twist elastic constants for the (3, 5, 1, 2) GB model at $\rho^* = 0.301$ plotted alongside S. The elastic constants appear to vary linearly with temperature in the nematic region with a more significant drop at the NI transition, an effect which is most prominent in k_{33}.

We proceed then to the (3, 5, 1, 3) model at $\rho^* = 0.30$, which is the density examined in Refs. [123] and [124]. Both report elastic measurements at $T^* = 3.40$ and $T^* = 3.45$ using long wavelength director fluctuations. Finite size effects were

analyzed in Ref. [124] by carrying out measurements at two system sizes, $N = 512,000$ and $N = 8,000$. Using the same $r_{cut} = 5\sigma_0$, we measure the elastic constants over a wide range of temperatures encompassing the previous measurements. Figure 3.5 compares our results to these earlier measurements [124]. Values for k_{11} and k_{22} are in excellent agreement with their results for $N = 8,000$, though our reported k_{33}'s are measurably lower. This is perhaps unsurprising, as the bend deformation is measured along the axis of alignment, effectively resulting in less nematogens per unit length. The result is an increased sensitivity to finite size effects compared to k_{11} and k_{22}. Ref. [124] also notes the largest drop in k_{33} from $N = 512,000$ to the smaller system at $N = 8,000$. Nonetheless, the results are remarkable as they highlight the strength of the free energy perturbation method. Our systems contain only $N = 338$ mesogens yet are capable of accurately capturing the elastic constants with limited impact of finite size scaling. This facilitates rapid and accurate determination of elastic constants for a large set of conditions as demonstrated in this work. As with Ref. [124], we make no direct comparison to the results of Ref. [123] due to the use of a different r_{cut} which has a non–negligible impact on the measured elastic constants [124]. The change in ν from 2 to 3 appears to result in a slight but noticeable separation of k_{11} and k_{22} across all studied temperatures. This is a slight improvement in terms of expected elastic ratios for cyanobiphenyls, though not quantitatively accurate [152]. This same model is reported to match birefringence data for 5CB closely [126], highlighting the nontrivial relationship between key liquid crystalline properties.
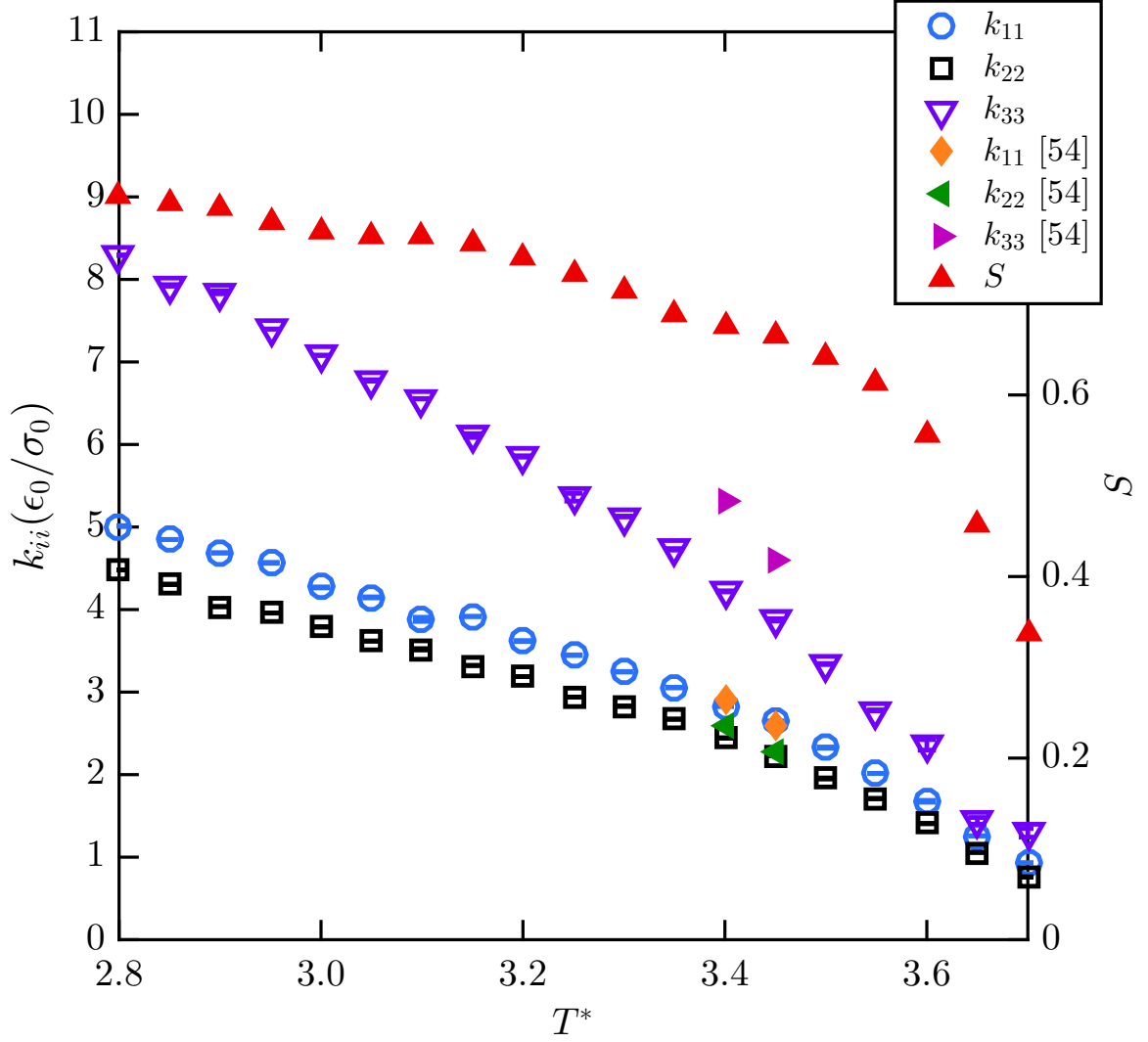
Figure 3.5. Measurements of the elastic constants for the (3, 5, 1, 3) GB model at $\rho^* = 0.30$ compared to reported values by Humpert and Allen [124] for $N = 8000$. We see good agreement for k_{11} and k_{22} but measure a significantly lower value for k_{33}. The bend elastic constant is likely to be the most sensitive to finite size effects.

The (4.4, 20, 1, 1) model is perhaps the most realistic model in common use, having been formulated to represent p-terphenyl. Bates and Luckhurst [122] provide

S–*T* diagrams at two pressures, $P^* = 1.0$ and $P^* = 2.0$, for the (4.4, 20, 1, 1) model (using the alternate notation $\langle P_2 \rangle$ for *S*). The $P^* = 2.0$, $T^* = 1.40$ state corresponding to $\rho^* = 0.1932$ is used as the starting condition for our investigation. We use a cutoff $r_{\text{cut}} = 6.0\sigma$, which differs slightly from the original study. After NPT equilibration, the final configuration is used to obtain *S* and k_{ii}. Figure 3.6 shows the measured elastic constants for the model. Separation of the k_{11}, k_{22} is immediately apparent and distinct from other models. Examination of the elastic ratios (cf. Figure 3.7) shows them to be constant across the entire nematic regime. We compare these values to those for *p*–azoxyanisole (PAA) reported in de Gennes and Prost [153] and find excellent agreement. This is a remarkable result given that the original model was coarse–grained to represent *p*-terphenyl. The semi–rigid nature and shape equivalence of PAA may be a contributing factor to the similarity of the elastic ratios.
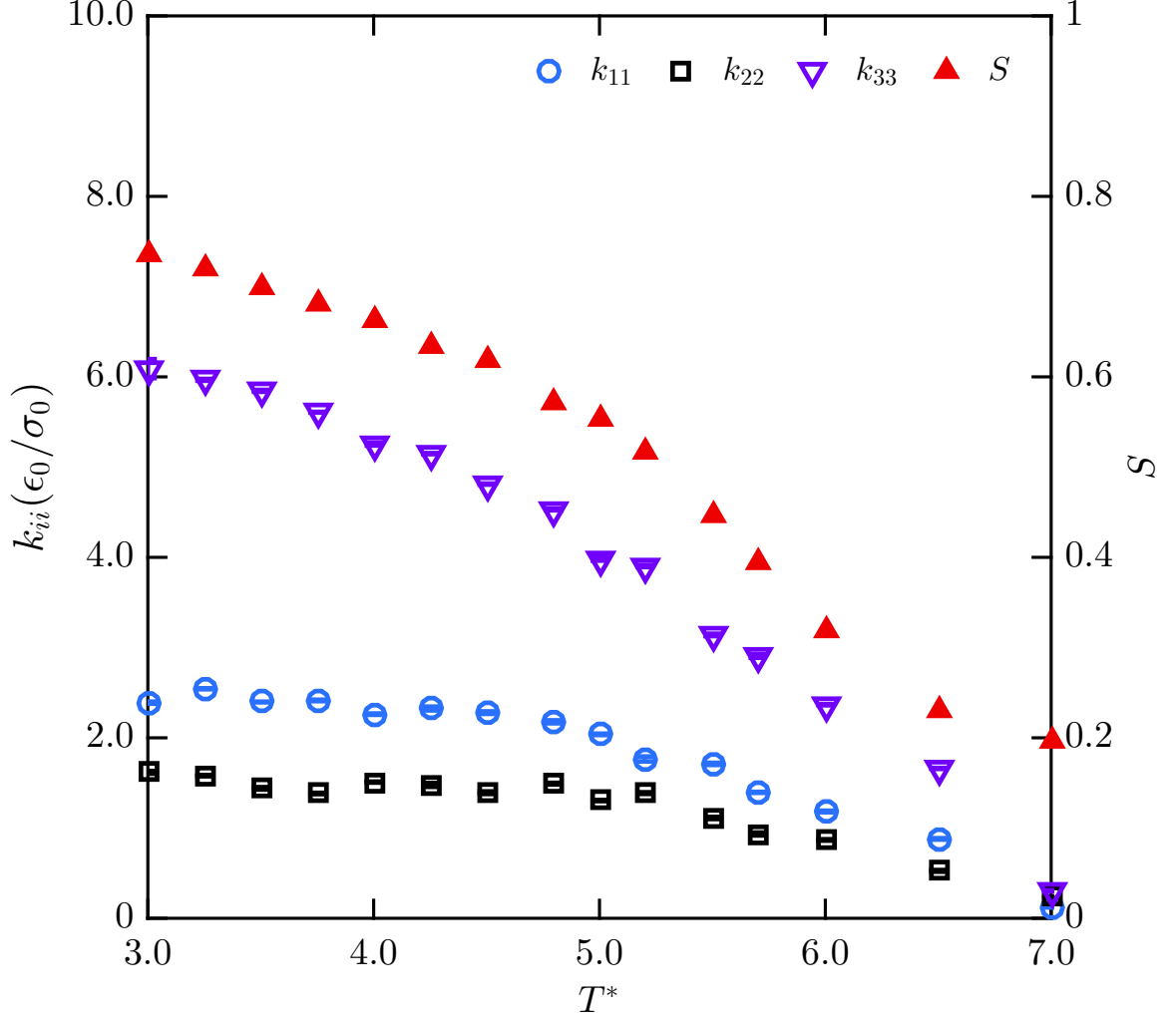
Figure 3.6. Elastic constants and order parameter S for the (4.4, 20, 1, 1) GB model at $\rho^* = 0.193$. Unlike the (3, 5, 2, 1) and (3, 5, 1, 2) models, this shows significant k_{11}, k_{22} separation. Both k_{11} and k_{22} also remain nearly constant until the onset of the NI transition with k_{33} roughly tracking S.

Ref. [125] also measured k_{22} for this model using the Fréedericksz transition method at $T^* = 1.65$, $P^* = 2.0$ with $N = 1728$ mesogens, obtaining $k_{22} = 4.7$. For comparison, we carry out the same measurement at the equivalent NVT conditions with $r_c = 5.5\sigma_0$, but slightly reducing T^* to 1.62 to match their reported

S in the Fréedericksz cell. We obtain a value of $k_{22} = 0.70$ which is substantially lower than their reported value. Luckhurst and Satoh [125] note that that based on data from Allen et al. [123], the elastic constants of a GB fluid should decrease with decreasing volume fraction. Given that Ref. [123] reports $k_{22} = 0.676$ for the (3, 5, 2, 1) model, measured at a higher volume fraction, one should expect that k_{22} for the (4.4, 20, 1, 1) be somewhat smaller. In contrast to the observation of Ref. [125], our recorded value is more in line with expectations, though not strictly lower than the (3, 5, 2, 1) value. The choice of volume fraction here (0.45) is also consistent with that studied for the $\kappa = 3$ models (0.47). Both k_{11} and k_{22} for our $\kappa = 4.4$ measurements are equal-to or smaller than those in the $\kappa = 3$ models. However, k_{33} is noticeably larger, likely due the dramatically increased anisotropy. This observation is an important one; the role of shape and potential anisotropies are not immediately clear and result in complex behavior. We also note that the value of k_{22} at the conditions in Figure 3.6 commensurate with S in Ref. [125] is larger, affirming the basic density–elasticity relationship for the same model. It is difficult to ascertain precisely why our measured k_{22} is so different from that reported in Ref. [125]. The Fréedericksz transition is an approximate measurement [124] that involves a heterogeneous system with boundaries. The threshold field which is related to k_{22} is approximated from a series of discrete field strengths. We also note that their measurement was carried out in the NPT ensemble while ours was in the NVT ensemble. Furthermore, a slab must be chosen from which the director orientation is used to deduce the threshold field.
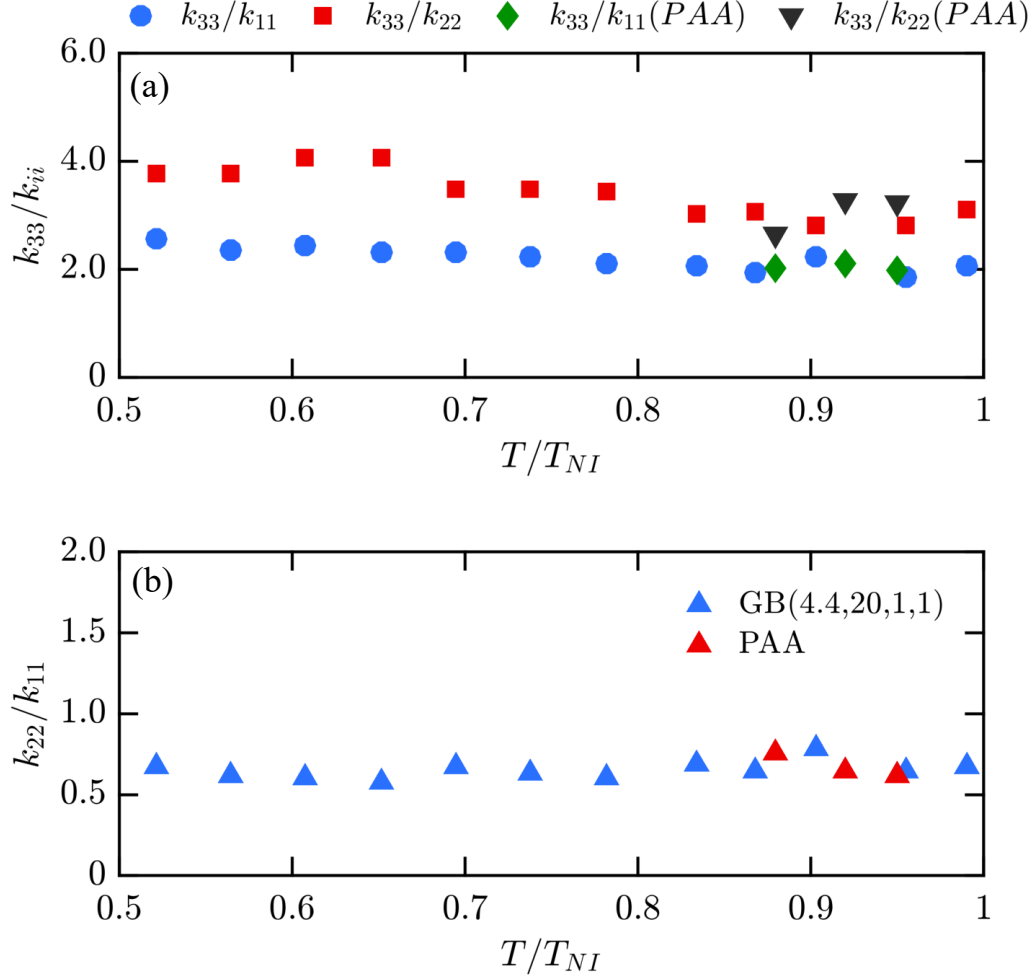
Figure 3.7. Ratio of elastic constants for the (4.4, 20, 1, 1) GB model in the nematic phase compared to PAA [153]. All three ratios, (a) k_{33}/k_{11}, k_{33}/k_{22} and (b) k_{22}/k_{11} are approximately constant for the GB model. Excellent agreement between the GB model and PAA for all three elastic ratios.

Using our computed k_{22} of 0.70, we calculate the unscaled twist elastic constant to be 5.6×10^{-12} N for PAA which compares favorably to the actual value of 4.3×10^{-12} N [125]. This, in addition to excellent matching of the elastic ratios, shows that in fact the (4.4, 20, 1, 1) GB model may well be an exceptional uniaxial coarse–grained model

both in phase and elastic behavior of a real LC mesogen—an objective of the original development. In contrast, the (3, 5, 2, 1) model was not explicitly parameterized to a real molecule, but rather chosen to be the minimum shape anisotropy that exhibited liquid crystalline behavior [122].

Finally, we also examine the discotic (0.345, 0.2, 1, 2) model [121], parameterized initially for a triphenylene core. The model has been shown the exhibit isotropic, nematic and hexagonal columnar phases [154, 128], a sequence of phases which has been observed in experiment for some benzoate esters of triphenylene [155]. A systematic variation of the shape and potential aniosotropy of the original potential also showed energy induced orthorhombic phases [154]. Here we set the softness of the GB potential, d_w, to 0.345, corresponding to the GBDII classification [156], with $r_{cut} = 1.6\sigma_0$. Cienega-Cacerez et al [128] studied the phase behavior of this model in great detail, and we carried out an initial NPT simulation to match the system density at $P^* = 30$, $T^* = 2.70$, in the discotic–nematic phase. Measurements of the elastic constants are shown in Figure 3.8.
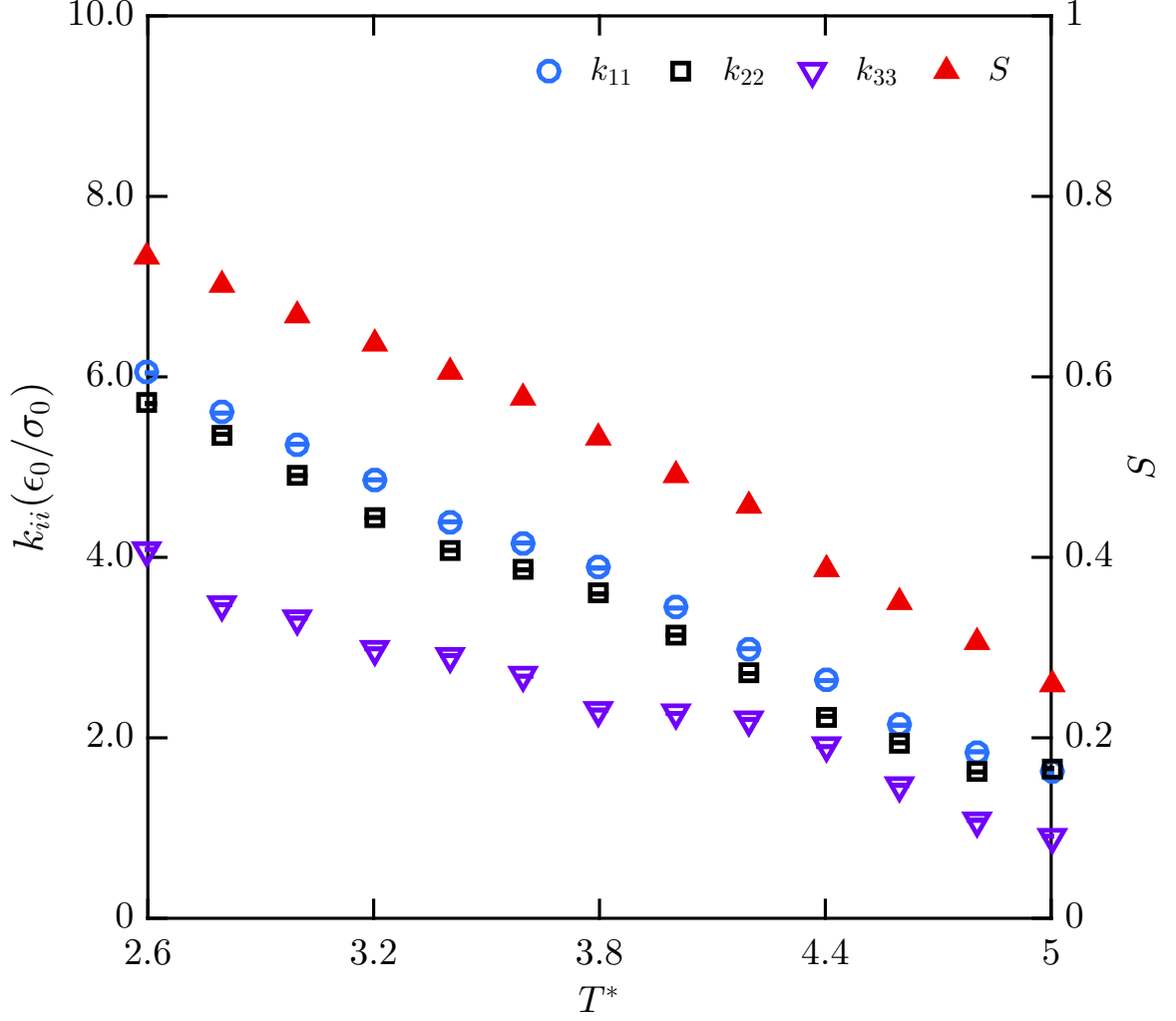
Figure 3.8. Elastic constants and order parameter S for the $(0.345, 0.2, 1, 2)$ GB model at $\rho^* = 2.360$. k_{33} is smaller than k_{11}, k_{22} which is in line with expectations for the discotic–nematic phase.

The most striking feature of the measured elastic constants is that bend deformations become the cheapest elastically, in stark contrast to the prolate GB models. This agrees with predictions which state that $k_{11} \approx k_{22} > k_{33}$ [157]. Theoretical predictions for perfectly ordered plate–like molecules show $k_{33} < k_{22}$ and $k_{22} > k_{11}$

but only marginally so [158] depending on the ratio of S and the fourth-rank scalar order parameter $\langle P_4 \rangle$. Our measurements do not definitively counter this, and are generally consistent with the model predictions. A more complex relationship exists between the elastic constants for real discotics. Benzene and naphthalene-based discotics typically have $k_{11}/k_{33} > 1$ [159]. This can also be the case for truxene derivatives though depending on the location of the nematic phase relative to the columnar phases, the ratio may be inverted [159, 160]. Additional k_{11}, k_{33} measurements for a homologous series of non–polar nematic discotics show a decrease in k_{11}/k_{33} with increasing temperature or increasing alkyl chain length [161]. We also see a similar trend in the temperature dependence of the elastic constant ratio for the (0.345, 0.2, 1, 2). Although the temperature dependence of splay and bend elastic constants of the discotic–nematic have not been widely studied, a recent report measuring them for a pentalkynylbenzene derivative shows similar mild convexity in k_{33} temperature dependence [162].

Of particular interest is how well the model reproduces the elastic properties of triphenylene based discotics since the original model was developed to represent a triphenylene core [121]. The elastic properties of two triphenylene derivatives were characterized by Phillips and co-workers [163] who observed a rather high value for k_{11}/k_{33} (> 3) in both cases. Intriguingly, for those systems the temperature dependence is unusual with the anisotropy increasing as the nematic–isotropic temperature is approached. They attribute this behavior to short range columnar order and antiparallel dipole correlations. The (0.345, 0.2, 1, 2) model may require explicit inclusion of dipolar behavior [164] or distributed point charges to capture such behavior. However, it appears to do a good job of representing nonpolar discotic nematic liquid crystals.
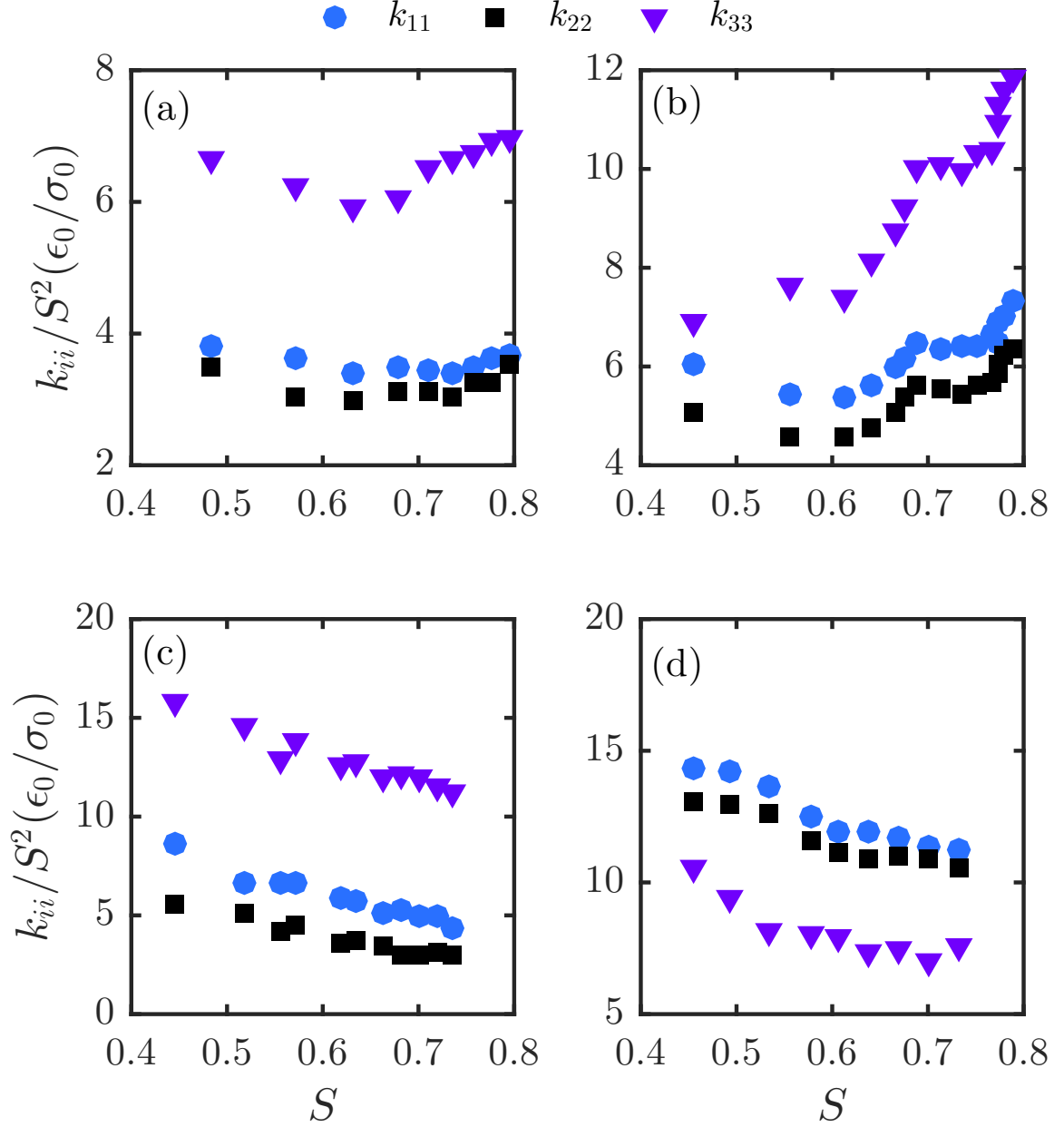
Figure 3.9. Elastic constants scaling with S for (a) (3, 5, 1, 2) (b) (3, 5, 1, 3) (c) (4.4, 20, 1, 1) and (d) (0.345, 0.2, 1, 2) Gay–Berne models. Mean field theory predicts $k_{ii} \propto S^2$. There is markedly different behavior for each GB model, but a general lack of agreement with theory. Similar observations have been made for other GB models and in experimental LC systems.

For each of these models, we also examine the S dependence of the elastic constants. Maier–Saupe mean field theory predicts $k_{ii} \propto S^2$ [19, 165], though both simulation [123] and experiment [162] have also observed otherwise. In the previous free-energy perturbation study of the (3, 5, 2, 1) model [75], the elastic constants for values of S between 0.6 and 0.75 were found to satisfy this dependence. In Figure 3.9 we plot k_{ii}/S^2 vs S for all four models studied. The (3, 5, 1, 2) model shows fairly constant values for k_{11} and k_{22} with a slight increase as T_{NI} is approached. This is consistent with what Allen et al. [123] observed for the (3, 5, 2, 1), which is an increasing k_{ii}/S^2 ratio with decreasing S. The trend for the bend elastic constant is more pronounced with a drop after the smectic–nematic transition and a subsequent increase as the nematic–isotropic transition is approached. Results are quite prominent for the (3, 5, 1, 3) GB model where k_{ii}/S^2 for all three elastic constants experiences a dramatic drop after the smectic–nematic transition, after which obeys mean field theory until the onset of the isotropic–nematic transition.

An opposite trend is found for GB(4.4, 20, 1, 1); k_{ii}/S^2 decreases linearly with increasing S. It is clear from our observations that there is significant deviation from mean field theory, changing substantially with not just shape anisotropy, but with interaction anisotropy as well, as the differences between the (3, 5, 1, ν) models demonstrate. Finally, the (0.345, 0.2, 1, 2) discotic GB potential conforms well to mean field theory within the nematic range, $S \approx 0.55$ to $S \approx 0.75$. Crossing through the nematic–isotropic transition however, k_{ii}/S^2 increases substantially. In fact, this is noticeable for all the models studied, with the exception of k_{33} for the (3, 5, 1, 3) potential. It is perhaps unsurprising as the mean field prediction is only valid within the nematic region.

3.6   Conclusion

The elastic constants of four Gay–Berne models, including one discotic system, are measured using density–of–states simulations. We find that for the (3, 5, 1, ν) model, $k_{22} \lesssim k_{11} < k_{33}$. Splitting of the k_{11}, k_{22} elastic constants occurs for the (4.4, 20, 1, 1) model which offers a much more realistic picture of the elastic constants to a real mesogen. Comparison of the elastic constant ratios to PAA [153] yields surprisingly good agreement. Direct mapping of a single k_{22} value to PAA is also within 30% of the experimental value. The (4.4, 20, 1, 1) model proves to be not only a good model in terms of phase behavior, but also in representing the elastic behavior of real liquid–crystals. For the first time, elastic constant measurements in simulation for of a discotic liquid crystal are reported. The (0.345, 0.2, 1, 2) discotic model shows unusual k_{33} temperature dependence, with $k_{11} \approx k_{22} > k_{33}$. The elastic constant ratios are commensurate with theoretical [158, 157] and experimental [160, 161] observations. The interesting temperature dependence is not unlike recent experimental results for room temperature discotic liquid crystals [162].

A comparison of the elastic constants for the (3, 5, 1, 3) model measured in this work using small systems ($N = 338$) to published values [124] for large ($N = 8 \times 10^4, 5.12 \times 10^5$) systems shows excellent agreement for k_{11} and k_{22}, given the disparity in system sizes. The deviation in k_{33} is attributed to enhanced finite size effects along the long axis of the nematogens. Nevertheless, this free energy perturbation technique proves to be an accurate and powerful tool in efficiently measuring elastic constants in simulation using small to moderate system sizes. Our results provide a systematic look into the elastic properties of common Gay–Berne mesogens, which is a cornerstone of any successful quantitative coarse–graining of real liquid crystalline media. In particular, we note that two common models capture very well the elastic ratios and the temperature-dependent elasticity of real mesogens. Further, our work on the (3, 5, 1, 2) makes possible systematic investigation of the interplay of k_{22}

and chiral pitch terms often incorporated into that model. Such investigations will allow a quantitative understanding of the role of molecular interactions in determining the onset of cholesteric and blue phases. We expect DOS techniques to facilitate the explicit accounting for elastic properties in future LC model development, yielding accurate potentials that can capture complex ordering phenomena, LC–collodial interactions and naonconfined morphologies.

CHAPTER 4

THE EMERGENT NEMATIC PHASE IN IONIC CHROMONIC LIQUID
CRYSTALS

4.1   Introduction

Liquid crystalline (LC) materials encompass a wide array of molecular systems
and mixtures with structural properties midway between a solid and a liquid. The
nematic phase in particular, which is liquid-like, yet exhibits orientational ordering
of molecular or supramolecular structures, enables many technological applications
due to its ability to act as a dynamic, responsive polarizer for impinging light. [34]
The response of the LC is determined by a curvature elasticity for orientational or-
dering in the nematic phase, whose elastic constants determine the energetic cost of
local reorganization. [34, 153] Traditionally, applications have centered on optics, in
particular in the display industry, where LCs have been utilized to manipulate the
passage of light. [166] More recent applications utilize mesoscale ordering in liquid
crystal defects to self-assemble functional materials, [167, 25] to create artificial elas-
tomeric muscles, [168] and to detect harmful agents. [7] In each of these applications,
it is important to finely control surface interactions and elastic properties.

Liquid crystals come in two primary flavors—*thermotropic* LCs experience or-
dering transitions in response to changes in the temperature, while *lyotropic* LCs
order as a system becomes more concentrated. [153, 34] Ionic lyotropic chromonic
liquid crystals (iLCLCs) are a unique subset of LCs consisting of flat disc or blade-
like molecules that self-assemble into stacks which themselves form ordered nematic

phases. While these phases have been known for decades, the full process of stacking into LC phases remains mysterious, and has been the subject of considerable theoretical and computational investigations discussed at length in a recent review. [169] It is becoming apparent that the there can be significant differences in the self–assembly process and the resulting aggregate distributions across different LCLCs. One of the primary assumptions involved in describing said process is the *isodesmic* nature of the stacking, where each additional molecule added to a stack is accompanied by a constant free energy change. [170] However, a growing body of experimental and computational evidence seems to indicate that this is only strictly the case in dilute systems [169, 171]. Furthermore, recent computer simulations, where theoretical expectations can be directly validated, have required conflicting modifications [171, 172] to isodesmic stacking models in order to explain observations. While this remains a useful model, it is unclear as yet if isodesmic stacking remains accurate in dense systems.

Here, we demonstrate a model for iLCLCs which captures all essential features of the LCLC phase through a competition of charge-like long-range repulsion and anisotropic attraction. Such a model exhibits self-limiting stacking behavior in dilute conditions due to the buildup of electrostatic repulsion along the stacking direction. In what follows, we present the results of extensive testing in the dilute and concentrated regimes to demonstrate that the model presents features which closely mirror those of experimental LCLCs, including the expected stack distributions, and near-isodesmic behavior in early formation. Further, utilizing advanced free-energy algorithms, [75, 76, 147, 151] we calculate the elastic properties of the nematic phase in iLCLCs and demonstrate explicitly how elastic anisotropy is intimately tied to the stack length in dense systems. This model presents a fundamental step toward a comprehensive understanding of microscopic structure–property relationships in ionic lyotropic liquid crystals.

4.2 Computational Details

While the process of self-assembly in lyotropic chromonic liquid crystals is not explicitly known, it has been hypothesized to be isodesmic. [173, 169, 174] Chromonic behavior arises in both ionic and non-ionic materials. One of the key features unifying many chromonic materials is the presence of stiff cores containing aromatic groups that allow for π–π stacking. The isodesmic behavior, however, should primarily apply to small-N aggregates, where N is the number of molecules in a stack, as some free-energetic mechanism must exist whereby stacking is self-limited under sufficiently dilute conditions. If the free energy of stacking is always favorable, one would expect large, extended aggregates to form at even the most dilute conditions, quickly approaching the Onsager limit and resulting in nematic ordering. Kinetic limitations could play a role, as suggested by a previous study [175] which examined energetic barriers to stacking; such features were seen to stabilize chromonic stacks. This is suggestive of a potential role that entropic or enthalpic repulsions can play in the formation of the phase. Here, we build on previous works exploring self-limiting clustering arising from interplay of short-range and long-range interactions [176] to develop a model which captures the salient features of ionic LCLCs (iLCLCs) through a combination of directional stacking interactions and long-range charge-like repulsions. Importantly, we aim to demonstrate that simply through the competition of these two interactions, a phase arises which includes all of the salient features of iLCLC phases.

Our model builds on the well-known Gay–Berne (GB) ellipsoidal model for discotic liquid crystals. We start with a GB pair potential [119, 20, 121] whose dimensions are chosen to mimic that of a typical iLCLCs (see Fig. 4.2). The form of the GB potential used is presented previously in Chapter 3, which overcomes numerical difficulties often found when modeling oblate ellipsoids. The key addition we make in this model is the inclusion of a long-ranged isotropic repulsion using the damped-

shifted force (DSF) potential. [177] This has the effect of penalizing long stacking through cumulative effects arising from the long-ranged repulsions. This repulsion potential [177] has the form:

$$U_{SF} = q_i q_j \left[\frac{1}{r} - \frac{1}{R_c} + \left(\frac{1}{R_c^2} \right) (r - R_c) \right] \tag{4.1}$$

where q_j and q_j are the nominal charges on particles i and j respectively, and R_c represents the cutoff radius for the potential. This repulsive interaction is applied to a virtual site placed at the center of each GB disc described above. It is intended to describe a fast–decaying electrostatic repulsion in an aqueous dielectric medium, without the need to explicitly account for counterions. The potential is thus seen as a coarsening of the charge neutral chromonic stacks in which net repulsion within the ionic chromonic stack core is enveloped in stabilizing oppositely–charged counterions. In the process of developing our model, we also tried the Debye–Hückel potential which mimics the screening effect of a polar solvent and saw qualitatively similar behavior. However, DSF was used because the repulsive buildup along a stack is more realistically represented.

4.2.1   Model optimization

Optimization of the forcefield parameters began by factoring in the molecular requirements of chromonic mesogens. Low aspect ratios (L/D) of around 0.10 in addition to a typical stack repeat distances of approximately 3 Åare noted as being characteristic of LCLCs. We attempt to capture these features by setting our GB shape and interaction anisotropies 0.2 and 0.1 respectively. In compact notation [122] this corresponds to a $(0.2, 0.1, 1, 2)$ GB model. The geometry is scaled to a diameter of 16.27 Å representing a rigid triphenylene core. The cross interaction term, ϵ_0, is set to 0.1 kcal/mol which results in a face–face interaction of 10 $k_B T$ at 300 K.

The choice of interaction parameters are important given the expected dominance of enthalpic interactions in the self–assembly process. In the case of an ionic chromonic this naturally corresponds to charge, where the attractive π–π interaction between a mesogen residing at a stack end and new mesogen is penalized through additive long range electrostatic repulsion; the gain in free energy of adding a mesogen to a stack decreases with stack length. This is supported by the observation of partial condensation of sunset yellow counterions around chromonic stacks in atomistic simulations [22], allowing for repulsive charge accumulation in the axial direction. In our model, we embed a virtual site with effective charge of 1.4 e^- in an aqueous medium at the center of the GB disc to mimic this effect, which also weakens the face–face interaction to approximately 8.5 $k_B T$. Another important added effect is the introduction of an energy barrier to binding which will be discussed below.

The remaining parameter d_w is the softness of the potential and controls the width of the GB potential, which in turn alters the onset volume fraction of nematic order. To illustrate this, 100 nanosecond NVT simulations containing 2048 discs are carried out for d_w values ranging from 0.1 to 0.4 at 300 K between volume fractions ϕ_V of 0.1 and 0.4. Figure 4.1 shows a clear orientational phase transition as measured by S, the nematic order parameter. The onset of this transition, denoted as ϕ_{NI}, is a strong function of d_w as expected. As the softness increases, the width of the attractive well in the GB potential broadens while maintaining an approximately constant depth. This effect of tuning the nematic–isotropic transition point allows us to choose $d_w = 0.4$ which corresponds to $\phi_{NI} \approx 0.22$ - a transition volume fraction similar to that of SSY [178, 48]. Subsequently we chose to investigate all phase behavior and elasticity using $d_w = 0.4$
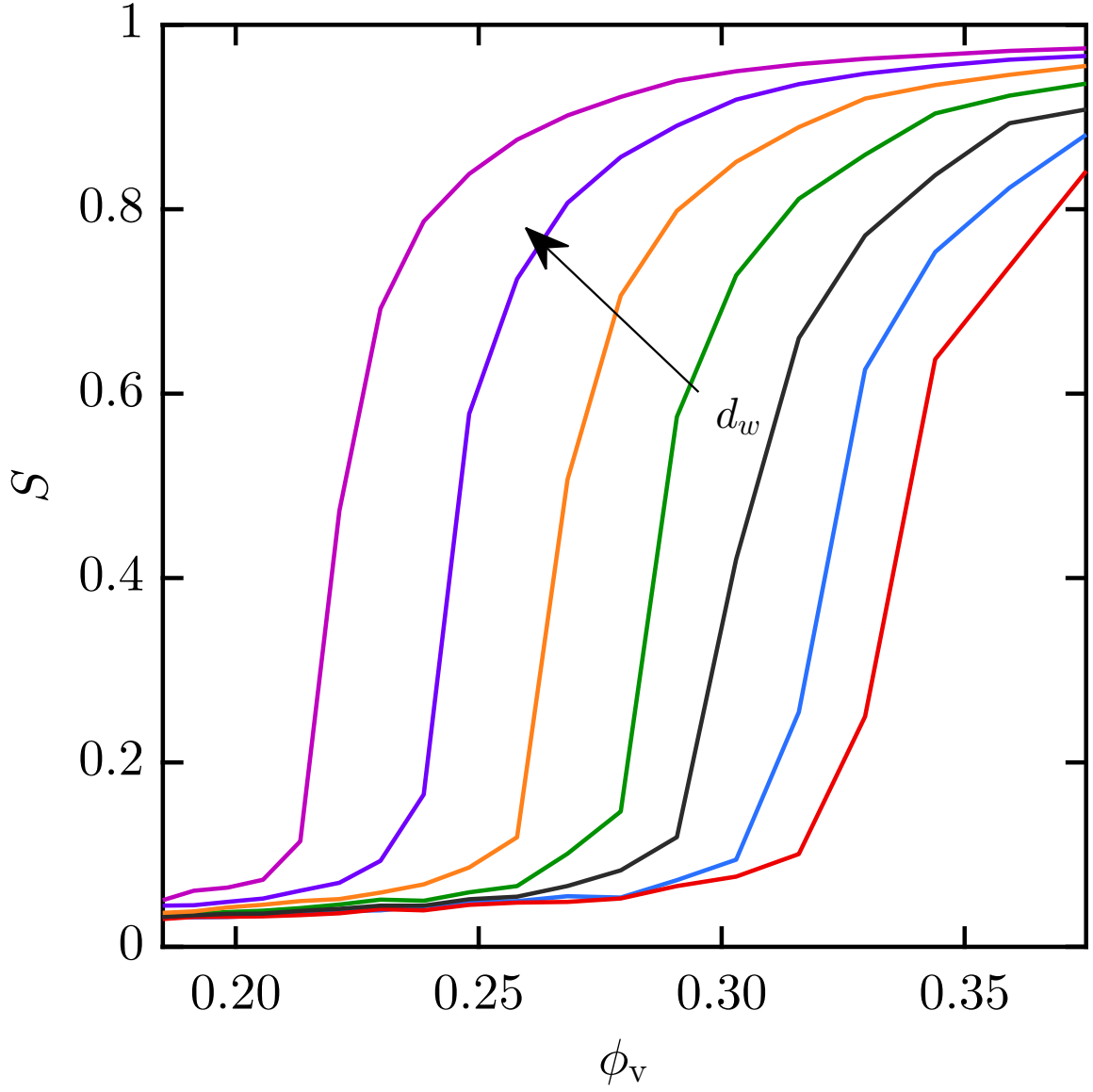
Figure 4.1. Nematic order parameter S as a function of volume fraction ϕ_v at 300 K for $d_w = 0.10, 0.15, 0.20, 0.25, 0.30, 0.35, 0.40$. The the onset of the nematic phase occurs earlier for larger d_w due to broadening of the attractive well. The ability to easily tune ϕ_{NI} allows for molecular specificity, in this case $d_w = 0.4$ approximating the transition volume fraction of SSY.

4.2.2 Potentials of mean force

The thermodynamics of aggregation are investigated by computing the free energy of stacking from a series of PMF measurements at 300 K. The order parameter ξ was the Euclidean distance between the center of mass of $N-1$ discs in a stack and an additional disc N. Stacks containing N discs are pre–assembled and allowed to equilibrate, after which the PMF measurement begins by sampling along ξ. A flatness target of 0.9 is chosen and the final converged free energy profiles βF are adjusted for the increasing volume of configurational space by adding the term $2k_B T \log(r/r_0)$ [179].

4.2.3 System preparation

Initial NPT simulations are carried out to compress the GB systems close to the desired densities. Snapshots are then scaled to the target densities and equilibrated for 5 nanoseconds under NVT conditions. Subsequent 50 nanosecond production runs are used to collect statistics. OpenMD 2.4 [180] was used for all unbiased molecular dynamics simulations while advanced sampling using expanded ensemble density of states (ExeDOS) [72] was carried out using Monte Carlo software SAPHRON. [151] Boxes in all simulations were fully periodic.
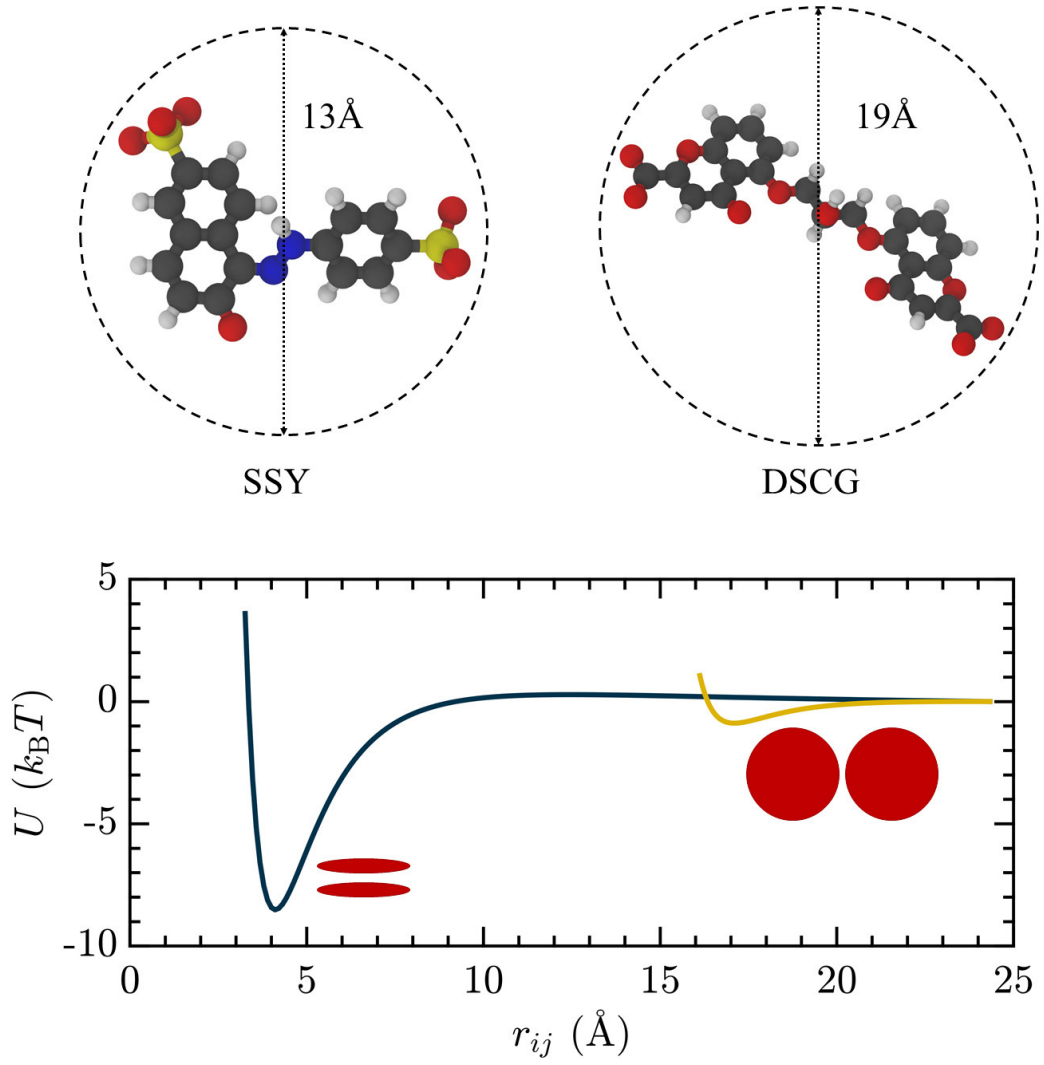
Figure 4.2. Approximate diameters of SSY and DSCG chromonic liquid crystals used to develop the Gay–Berne coarse grained model. The potential shown represents the effective interaction between two 16.27 Å diameter discs in face–face and side–side orientations.

After initial simulations are performed to calculate the nematic ordering tensor $\vec{Q}$ and scalar order parameter S associated with a given concentration, expanded

ensemble biased simulations are performed to extract elastic constants as described in Chapter 3. We have included a detailed explanation of our methods in the supporting information. Briefly, the simulation box is divided into four regions. In the "edge" region straddling a periodic boundary, an umbrella-like bias is applied to the largest eigenvector of the $\vec{Q}$-tensor, corresponding to $\hat{\mathbf{n}}$, so that it aligns with the $\hat{\mathbf{z}}$-axis. In the central region, statistics are gathered on the orientation of the eigenvector $\vec{n}$ in order to influence the system to comprehensively sample configurations with small deviations from the fixed edge orientations. Within the remaining two regions, between the edge and center, no bias is applied. This permits a linear-like deformation to be established, which can select out a single elastic deformation—bend, twist, or splay. The resulting parabolic free energy profile is used to obtain the elastic constant of interest by fitting the expression for free energy density

$$f = \frac{1}{2}k_{ii}\left(\frac{1}{1-2\beta}\right)\left(\frac{\partial n_j}{\partial x_{j'}}\right)^2,\tag{4.2}$$

where k_{ii} defines the elastic mode of interest, and j nd j' define the deformation in terms of the vector component biased, and direction along which the bias is applied. Note that the parameter β within this equation is determined by the fraction of the box occupied by the restriction region as in prior works. [76, 147]

4.3   Results and Discussion

4.3.1   Phase behavior

We initially demonstrate that this model exhibits a nematic–isotropic (NI) transition consistent with chromonic stacking. Figure 4.1 shows how the potential 'softness' d_w plays a key role in determining the location of the phase transition. After performing some exploratory simulations, we settle on the parameter $d_w = 0.4$, which induces a transition at volume fraction $\phi_{NI} \approx 0.22$, similar to experimental observations of

SSY. [178, 48] Subsequently we examine only this model.

The low computational cost of our model enables us to study stacking and phase behavior in larger systems than previous atomistic investigations have allowed [22]. As illustrated in Figure 4.4, the first observed ordered phase is identified as a chromonic N phase wherein a nematic array of columns is formed with no positional ordering. The nematic order parameter S is approximately 0.8 at 300 K - much larger than the typical degree of alignment for a typical nematogen. [181, 152] However, we find that this is commensurate with the reported value for SSY (≈ 0.75) at the same temperature. [178] Densification of the chromonic N phase gives rise to an M phase, distinguished by hexagonal alignment of the column array. The richness of the phase behavior exhibited and by this simple model indicates that the salient molecular characteristics necessary for chromonic behavior have been well represented. Stacking defects are also prevalent throughout the N and M phases, predominantly as lateral shifts of mesogens within individual columns. This is particularly interesting as such lateral shifts, referred to as a "C" or junction defects, have been proposed as a mechanism to explain a discrepancy between the length of SSY chromonic aggregates and Onsager model predictions [48] and the presence of an additional fluctuation mode detected in the bend scattering geometry of DSCG. [52]

Figure 4.3 plots a phase diagram for this system in temperature T and volume fraction ϕ_V. This is very prominent in the case of the isotropic–N transition, as shown in Figure 4.1. The N–M transition is far more subtle, with the phase boundary demarcated by a change from $S \approx 0.8$ to $S \approx 0.9$. While at 300 K, the volume-dependence of ordering in SSY is quantitatively matched well by our model, our model is not as sensitive to temperature as the experimental systems. [178, 48] Importantly, no curvature is apparent in the N–M phase boundary within the temperature range of this work.
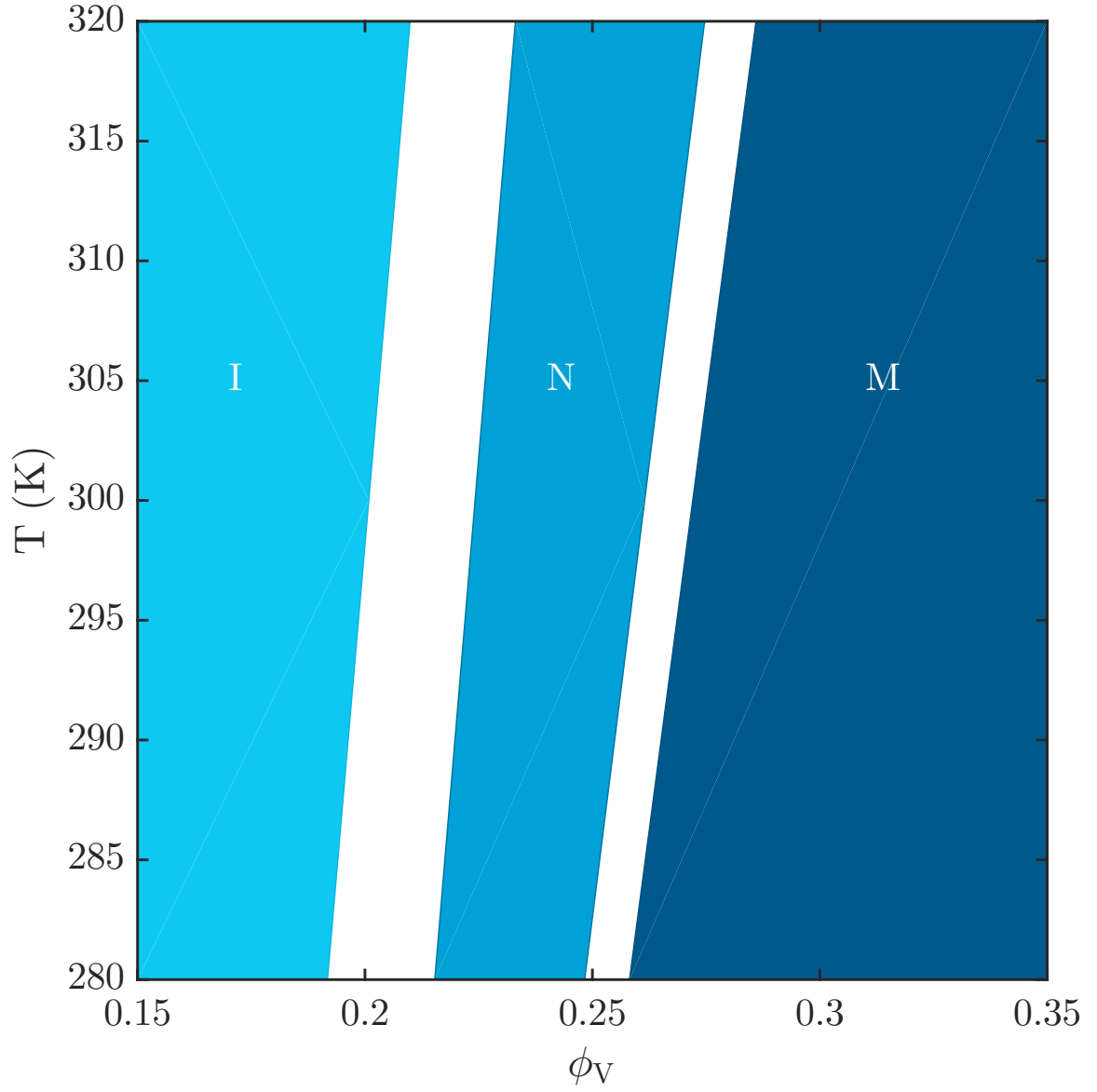
Figure 4.3. Phase diagram of the proposed minimal chromonic model as identified by S, the scalar order parameter. A 441 point grid (21×21) of NVT simulations were carried out spanning $T \in [280, 320]$ K and $\phi_V \in [0.15, 0.35]$. The phase boundaries are approximated by identifying the volume fractions at either side of a discrete jump in S. Raising the temperature has a modest impact on ϕ_v^{NI}.
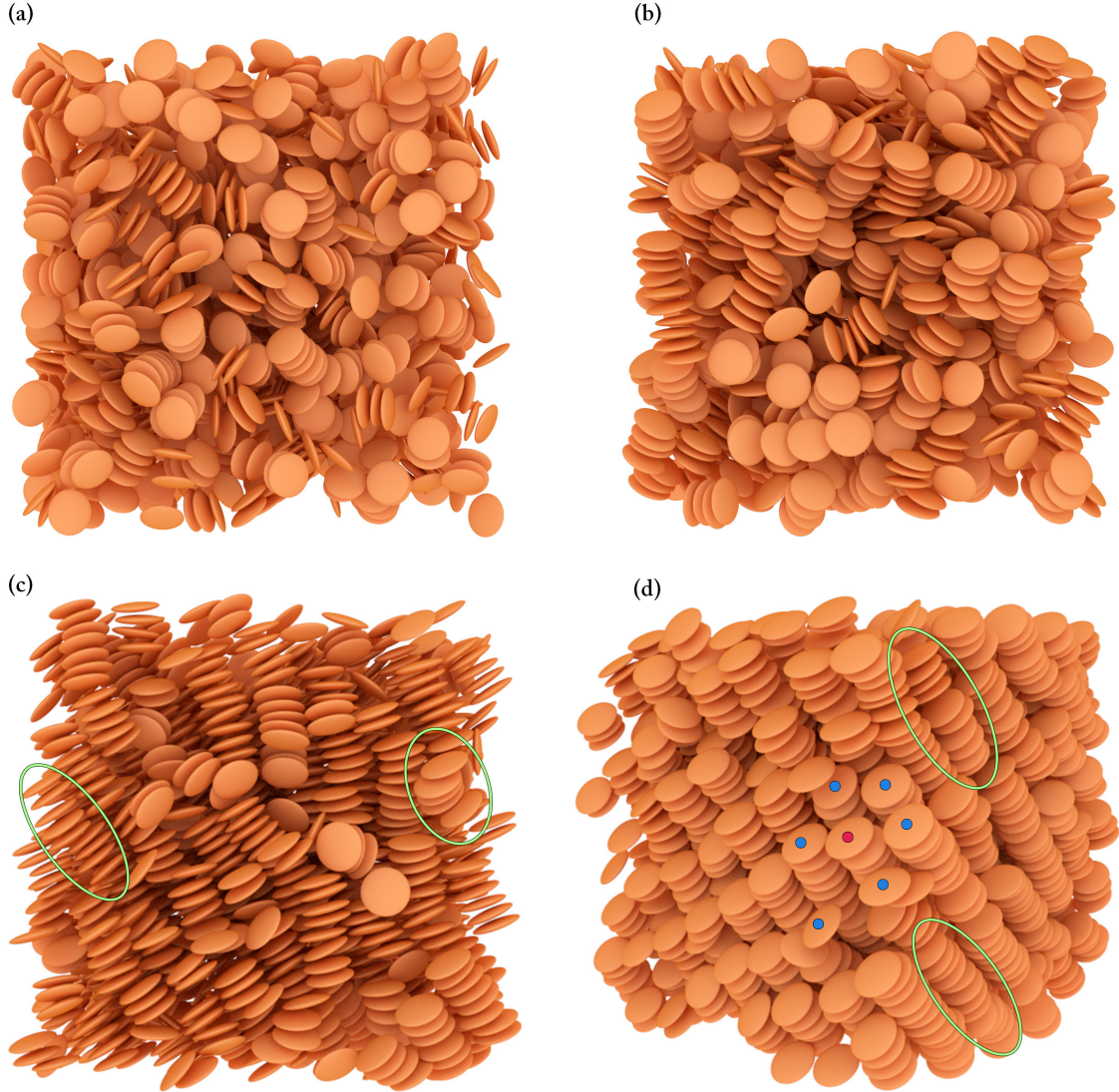
Figure 4.4. Snapshots of LCLC system at 300 K and varying volume fraction. At $\phi_V = 0.18$ (a) the system exhibits no nematic order. Monomer and dimer stacks are prevalent though aggregates of lengths between 3 and 5 are also clearly present. Through the NI transition (b) with $\phi_V = 0.22$ we observe an increase in stack length and a preferential alignment of longer aggregates towards the nematic axis. The chromonic N phase (c) shows global orientational but no positional order ($S \approx 0.8$) at $\phi_V = 0.24$. The presence of column defects are apparent with circles added to select stacks for emphasis. Hexagonal ordering in the chromonic M phase (d) is highlighted with blue dots surrounding a central red dot with defects still present at $\phi_V = 0.32$. Though stacks are significantly larger than in less dense phases, most do not persist across the periodic boundary and there remains a significant distribution of monomer and dimer aggregates.

4.3.2 Self–assembly

A striking feature of the model, demonstrated in Figure 4.4 is its tendency to self-assemble into aggregates at low volume fractions where no nematic order is present in the system. This is a key characteristic of LCLCs. [173, 47] At low volume fractions, dimers dominate the assembly landscape, with fewer aggregates consisting of more discs. As the system is densified toward ϕ_{NI}, there is a clear increase in mean stack length driven by particle crowding but no substantial increase in global orientational alignment. This is also in accordance with the expected behavior of LCLCs, [173, 47] and a key difference with standard GB discotic models. The self limiting nature of the stacking is apparent, as at such densities, a discotic columnar phase is observed in GB models not containing long–range repulsion. [156, 128]

Self-assembly within this model is distinct from prior coarse-grained works, including models based on rigid arrangements of Lennard-Jones spheres, [170] which exhibited wormlike micellar (rather than columnar) phases at high concentration, and models of sticky–ended cylinders, which form a nematic phase of linear semi–flexible chains. [182] Each of these models exhibits a deep attraction minimum, but does not include additional repulsive barriers which will arise in the assembly of iLCLCs of interest here. This repulsive barrier necessarily plays a key role the kinetics of stacks, and size limiting of aggregates. It should be noted, however, that even non–ionic LCLCs exhibit repulsions, due (e.g.) to a loss of chain entropy, which serve to penalize the formation of longer stacks. [183] Even with this barrier, stacks within our model are dynamic. Though the average stack distribution in the system is well defined, each individual aggregate is formed and reformed by the transient joining and leaving of individual discs. A prior atomistic molecular study of SSY [22] showed similar behavior where the correlation time of molecular orientation corresponding to the memory of stack arrangement was shown to be on the order of 10 nanoseconds.
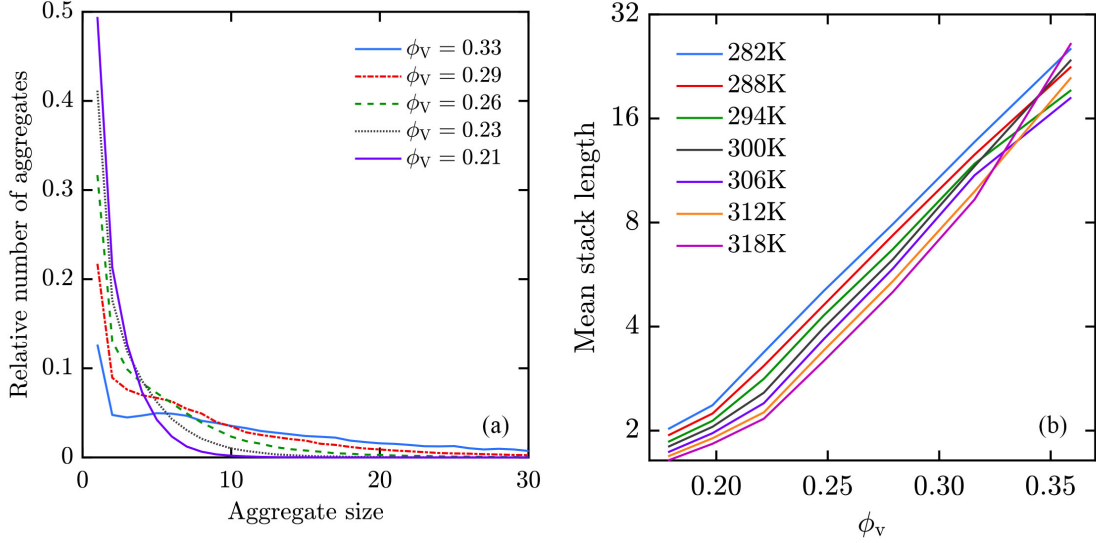
Figure 4.5. A detailed look at the distribution of stack lengths throughout the system shows (a) an exponential–like distribution across volume fractions immediately before, near and after ϕ_v^{NI} at a fixed temperature of 300 K. This seems to agree with proposed isodesmic stacking models. [169, 48] This exponential gives way to a bimodal distribution with a small preference for moderate stack lengths $N \approx 5$ approaching the M phase. Mean stack lengths as a function of volume fraction ϕ_v at various temperatures (b) show increased growth of mean stack length when passing through the I–N transition as indicated by the logarithmic axis. The equal spacing between lines at low volume fractions demonstrates stack length grows exponentially as temperature is lowered.

Using distance $|\vec{r}_1 - \vec{r}_2|$ and orientational thresholds $(\hat{\mathbf{n}}_1 \cdot \hat{\mathbf{n}}_2)^2$ of 7.0Å and 0.8Å respectively between the locations $\vec{r}$ and orientations $\hat{\mathbf{n}}$ of two mesogens, we obtain the probability distribution of nematic stack lengths within each studied system. Figure 4.5 (a) highlights the distribution of aggregates containing a given number of discs at 300 K for various volume fractions. Our distributions are distinctly exponential at low volume fractions, with a slight enhancement in aggregate size occurring

as the system is densified toward the M phase. Our distributions contrast notably with prior studies of non-ionic LCLCs, [183, 171] where isodesmic behavior is apparently violated by a relative lack of free mesogens in solution. Our model exhibits a pronounced probability for free particles at all concentrations studied, even as the exponential character of the distribution is lost approaching the M phase through an enhancement in stacks of length $N \approx 5$ relative to smaller aggregates; some temperature dependence is observed in the relative distributions, as typified by the mean stack length plotted in Figure 4.5 (b).

To examine this more deeply, we investigate the thermodynamics of aggregation by computing the free energy of stacking from a series of PMF measurements at 300 K. Beginning with a stack of N discs, we compute the stacking free energy as a function of the Euclidean distance $r_{ij} = \sqrt{\vec{r}_{N-1} - \vec{r}_N}$ between the centers of mass of $N-1$ discs and the Nth disc; this is given in Figure 4.6.

The free energy of dimer and trimer formation are approximately equal at 6 $k_{\mathrm{B}}T$, which is comparable to the experimentally measured and simulated values of 7 $k_{\mathrm{B}}T$ for DSCG and SSY, [184, 22] though it contrasts with the stacking free energies obtained from atomistic simulations of non-ionic TP6EO2M, which are significantly higher, depending on the forcefield. [183] These differences are not of particular concern as stacking energies for chromonic LCs are known to vary within the range of 7 to 12 $k_{\mathrm{B}}T$. [184] Ref. 183 points out that the stacking free energy is roughly proportional to the size of the aromatic core, and given our choice of molecular dimensions and interaction well depth our result fits in nicely within this trend of reported stacking free energies; our discogens expose less cross sectional surface area compared to the simulated non-ionic LCLCs (cf. Fig. 4.2) hence the lower stacking free energy.
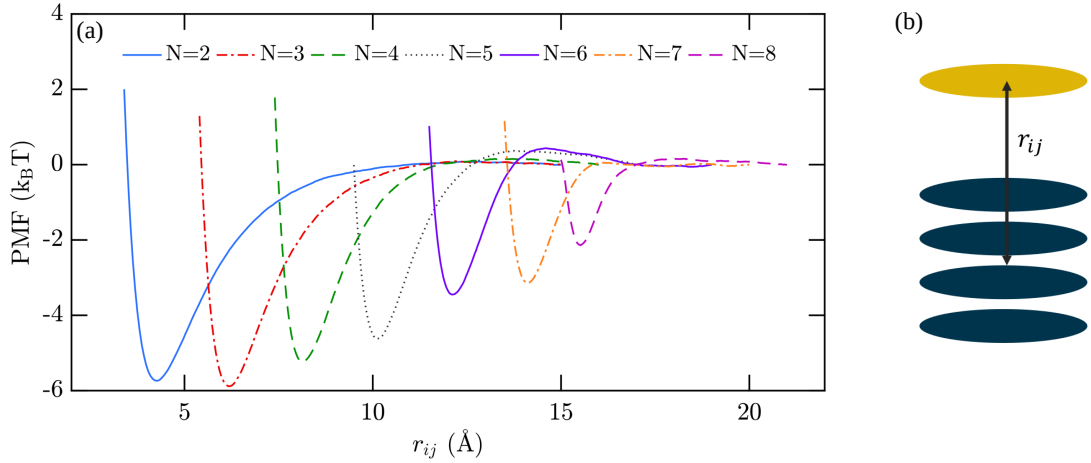
Figure 4.6. Free energy of stacking (a) obtained through PMF measurements for $N = 2$–8 stacks at 300 K as a function of center of mass distance between a stack and new disc (b). Dimer and trimer free energies are approximately equal and show no barrier to association. Larger stacks both exhibit an energetic and entropic penalty ($\propto 2\log(r_{ij})$) for the addition of a new disc to an existing stack.

Importantly, beginning with $N = 4$, we observe a marked decrease in the free energy of stacking. Concomitantly, a small energy barrier to binding begins to appear, peaking at $N = 6$. These striking features offers some partial validation of isodesmic stacking in the dilute limit as has often been argued, [169] and helps explain the large proportion of small aggregates in solution at all densities (cf. Fig. 4.5(a)). Both the decrease in free energy and the barrier arise from interplay between short and long-ranged interactions in the stack. As with the proposed two–dimensional corona model, [175] this energetic barrier increases the penalty to de–stacking despite the shallower well, effectively mimicking the on-off kinetics of shorter stacks. The result is an appearance of quasi–isodesmic stacking manifest in the stack size distribution (see Figure 4.5(a)). In the large stack limit however, the net free energy of binding

decreases in such a way that the effective energy scale is commensurate with thermal fluctuations and prevents further aggregation.

It is important to note that the PMF measurements in Figure 4.6 were carried out under dilute conditions. Consequently, it does not represent the environment in which the N and M phases occur, which can exhibit substantial crowding. Undoubtedly, the entropic cost to de–stacking will play a larger role in the resulting PMF, which would lead to larger equilibrium stack lengths, as witnessed. However, the mechanism elucidated by the PMF measurements at low concentrations is vital in understanding the self–limiting behavior of chromonic stacking. In a two–rate model, [171, 169] there would effectively be nothing to prevent the precipitation of long stacks from solution, even in dilute conditions. Our results point to a systematic decrease in binding energy with thermal fluctuations playing an increasingly important role in limiting the stack sizes and thus controlling the onset of the nematic phase.

Figure 4.5(b) shows the mean stack length as a function of volume fraction for various temperatures. As expected, the mean stack length at low volume fractions in the isotropic phase is insensitive to temperature. At higher volume fractions, an increase in enthalpic interactions leads to a greater temperature-dependent effect as witnessed. This is unlikely to be due solely to increased orientational ordering alone due to the weak temperature dependence of the order parameter. In fact, the data in Fig. 4.5(b) is remarkable in two ways. First, the rate at which the mean stack length grows displays a sharp change at the respective NI transition points for the each temperatures. Second, and perhaps more interesting, is that the rate of growth in the ordered phase is exponential. This enormous rate of growth has been observed previously in a highly idealized LCLC model. [170] What is peculiar here is that this growth rate is belied by the fact that the mean stack size is limited by the finite size of the box, yet there appear to be no signs of slow–down even in the very dense case. Such behavior hints at an intrinsic underlying thermodynamic equilibrium governing

the stack size distribution.

To rule out the role of system size on the equilibrium stack distribution we perform two additional simulations containing fewer ($N = 1024$) and greater ($N = 4096$) number of particles. Figure4.7 shows a near–identical mean stack length across the entire range of volume fractions for the system sizes studied, which signifies approaching the thermodynamic limit. It is also an important result for the purpose of characterizing the elastic properties. Given the prominent elastic anisotropy observed in real–world LCLCs, in particular with both DSCG [52] and SSY [53], the equilibrium aspect ratio of the stacks will likely play a key role in determining k_{ii}/k_{22}.
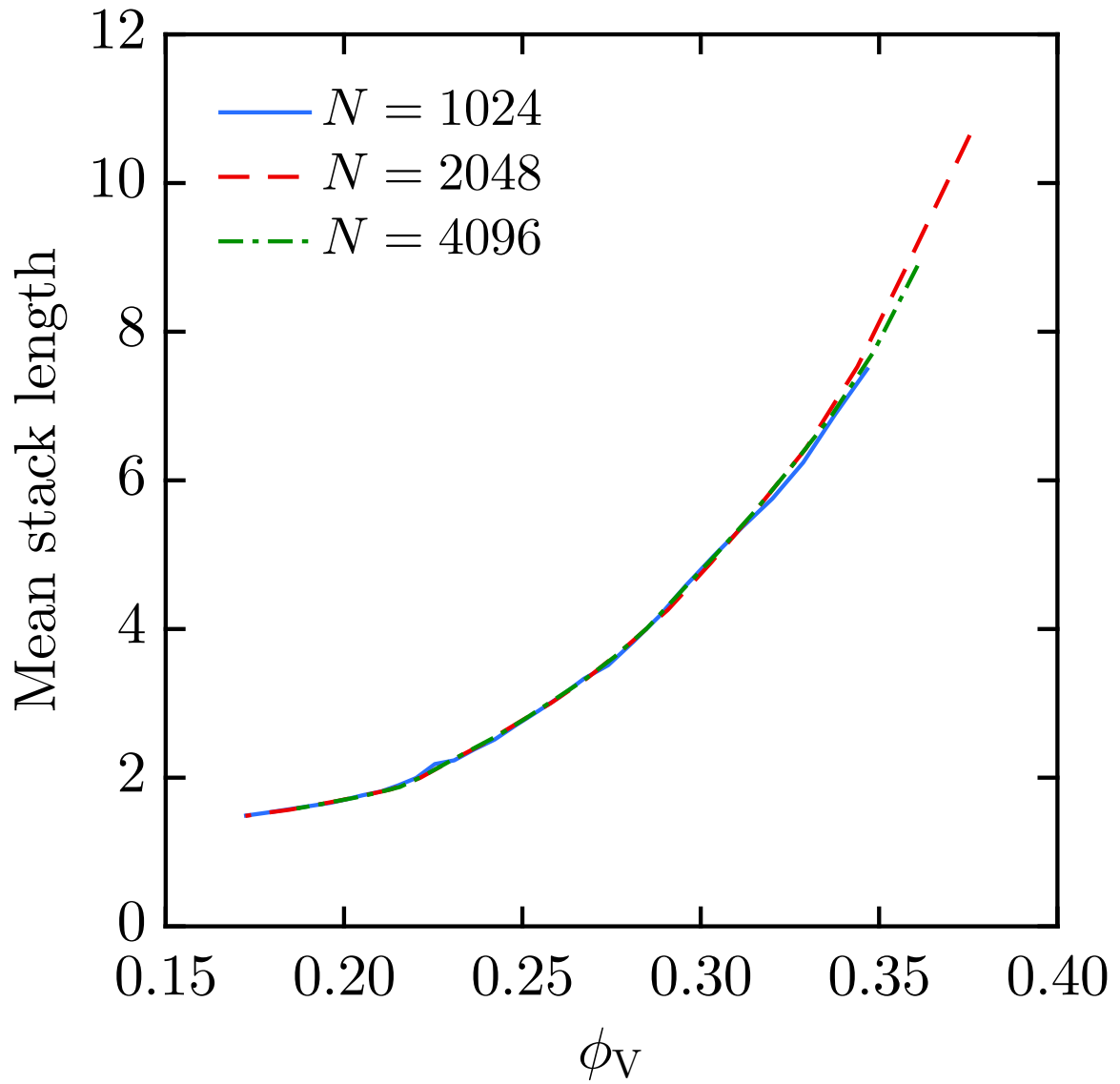
Figure 4.7. Mean stack length as a function of volume fraction ϕ_v for three different system sizes at 300 K. Near–perfect agreement suggests that by $N = 1024$ there are little finite size effects involved in the equilibrium stack distribution.

4.3.3 Elastic properties

One of the most prominent features of chromonic liquid crystals is the dramatic elastic anisotropy present in systems that have been experimentally studied. In particular, both SSY [53] and DSCG [52] have $k_{11} \approx k_{33} >> k_{22}$ where k_{22} is approximately an order of magnitude smaller than k_{11} and k_{33}. A common theoretical reasoning for this odd relationship is that twist deformations result in minimal disruption of flexible stacks by arranging aggregates into layers [52, 55]. The flexibility of the stacks allows their deformation to accommodate their bending, while splay deformations necessarily create vacancies between existing stacks requiring new stacks to intercalate; each of these modes comes at significant free-energetic cost.

Our work represents the first attempt at characterizing the elastic properties of a model chromonic liquid crystal system. Figure 4.8 shows the measured Frank elastic constants for the model in the chromonic N phase at 300 K. Obvious is the lack of significant anisotropy in k_{22}, although it is smaller than splay and bend. A plot of the elastic ratios (see Fig. 4.9) demonstrates this further, with k_{ii}/k_{22} increasing at higher concentrations, but never exceeding 1.3. Furthermore, k_{33}/k_{11} remains approximately constant though this is clearly not the case in SSY [53] and DSCG. [52] The absolute magnitudes of the elastic constants we calculate are reasonable and within experimental bounds.
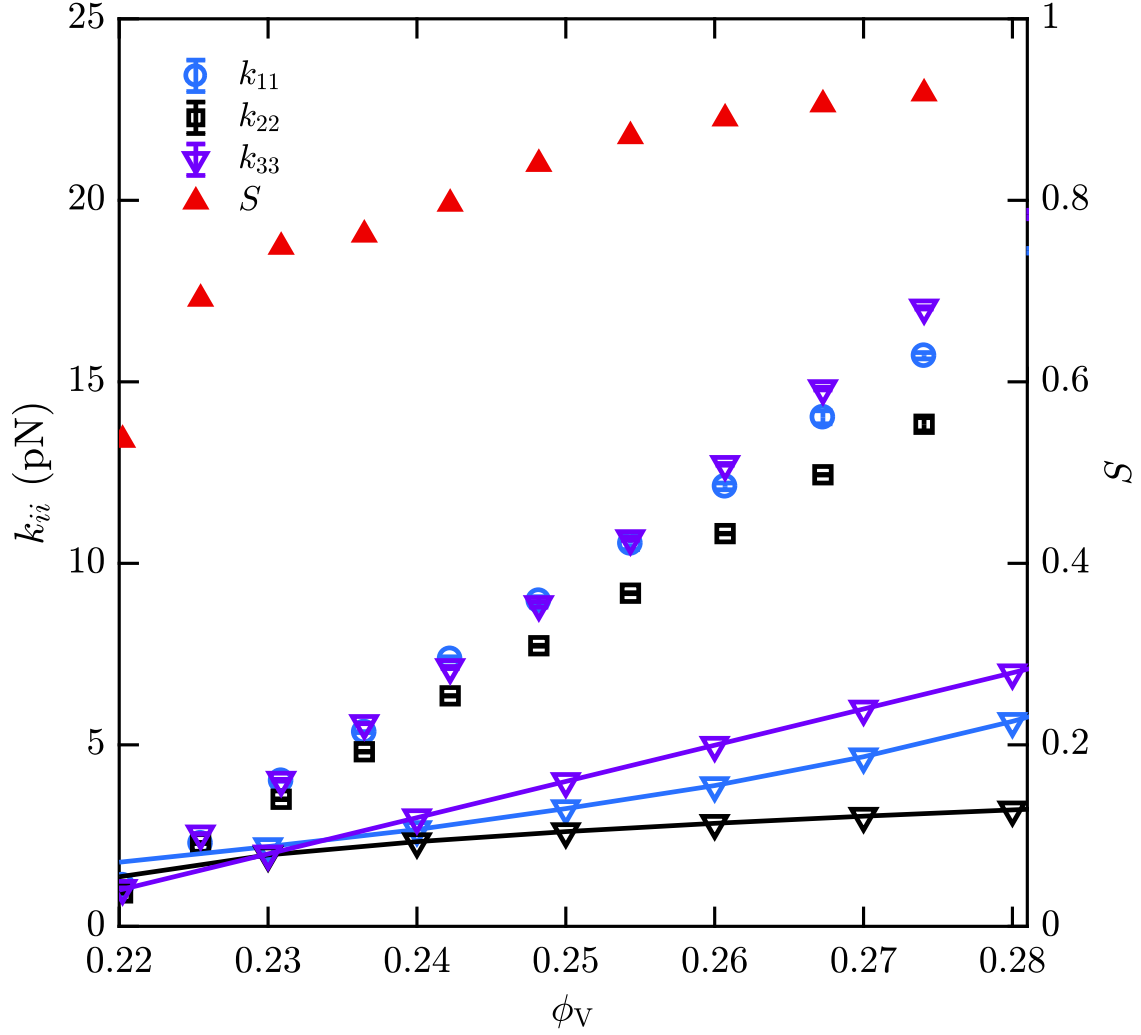
Figure 4.8. Frank elastic constants of our chromonic minimal model (open symbols) in the N phase at 300 K compared to the theory of Meyer et al. [55] for long polymer chains (solid lines). The twist (k_{22}) elastic constant of our is lower than splay and bend, but not to the degree seen in experiment for DSCG [52] and SSY. [53] There is qualitative agreement in the general trend predicted via Meyer's theory, with $k_{33} \gtrapprox k_{11} > k_{22}$. Note that the data for S here comes directly from elastic simulations and thus differs marginally with that in Figure 4.1, though the values are consistent
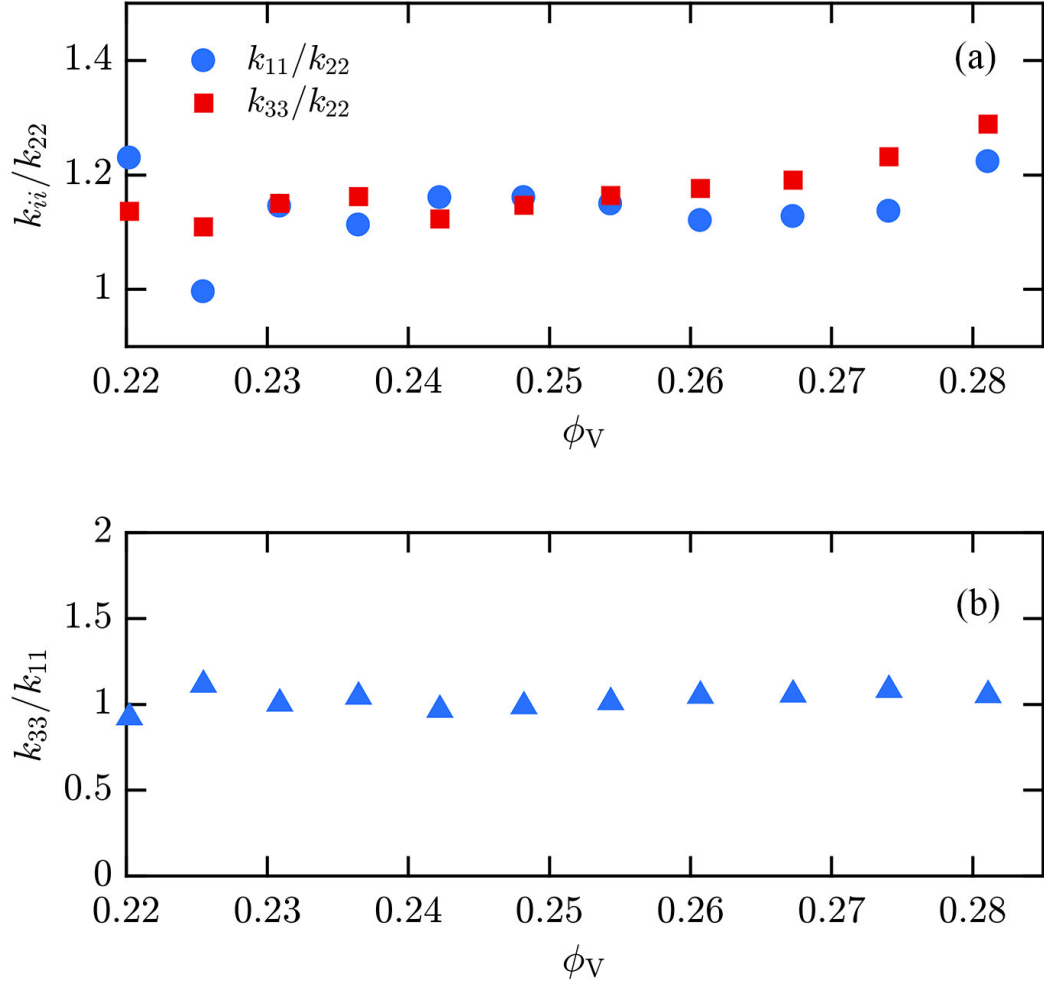
Figure 4.9. Elastic ratios for our model showing significantly less elastic anisotropy than observed experimentally. k_{11}/k_{33} is also nearly flat across concentrations which is unexpected.

The semi-flexible chain theory due to Meyer and co-workers [55] is the prevailing theory utilized to describe the elastic behavior of LCLCs. [53, 52] Comparing our measured elastic constants to those predicted, as shown in Figure 4.8, demonstrates qualitative agreement in the concentration dependent trends, but not the absolute

values or ratios. This is not surprising as the limitations of this theory in the context of LCLCs have been discussed at length elsewhere. [52] Nonetheless, our results run counter to expectations for a chromonic system. We may draw on similar geometric arguments to those stated previously and propose a new hypothesis for our results, which could help elucidate the behavior of LCLCs in the limit of smaller aggregates. The system in question exhibits a large distribution of small aggregates across a broad concentration range. This results in a significant proportion of stacks having sufficiently large L/D aspect ratios such that they can be treated as individual calamitic-like mesogens. Then, our system can be thought of as a mixture of said nematogens and discotic LCs. Comparing to extensive prior elastic measurements of Gay–Berne models, [147] $k_{22} < k_{11} \lesssim k_{33}$ is seen in calamitic systems. However, k_{33} is also typically much larger in those systems than what we observe here. For discotic systems of similar aspect ratio however, $k_{33} < k_{22} \approx k_{11}$. As the chromonic system is necessarily a mixture of these two regimes, a system exhibiting ideal mixing properties [151] should admit elastic properties which are similar to those seen here. This does not, however, necessarily violate the theory of Meyer, [55] as sufficiently long stacks may be well-approximated by the semi-flexible chain. Therefore, we hypothesize that there is an enthalpically driven crossover between the mixture-like behavior observed in our model to semi-flexible chain behavior when longer stacks may be achieved in dilute solution.

It is interesting to put this model in the context of recent experimental measurements by Nayani and co-workers, [185] who observed interesting behavior in the scalar order parameter and in the elastic constants of SSY solutions just below the nematic transition. Importantly, below the NI transition temperature appropriate for each concentration of SSY, universality is observed in measurements of the nematic order parameter S (P_2 in Ref. 185), and the higher moment P_4. We also observe universality in P_2 as illustrated in Figure 4.10, which further supports the validity of

85

our model. Interestingly, in that paper it is claimed that adoption of particular configurations by LCLC tactoids is driven by the relative scaling of splay with aggregate length L rather than persistence length λ_p, as outlined by Meyer. For our model, all three elastic constants grow as the length of aggregates grows, which would appear to disagree with these results. It is important to note that aggregates must be larger than the persistence length for the predictions of Meyer to hold, a limit which is not reached by the aggregates in our model. The persistence length of aggregates in our model may be calculated from the correlation function $\hat{\mathbf{n}}_i \cdot \hat{\mathbf{n}}_j$ correlation function along the axial direction of each stack in the chromonic N phase ($\phi_v \approx 0.25$). As an illustrative example, at $300K$ such a calculation yields a value of 12.06 which well exceeds the mean stack length at those conditions (cf. Fig. 4.5).
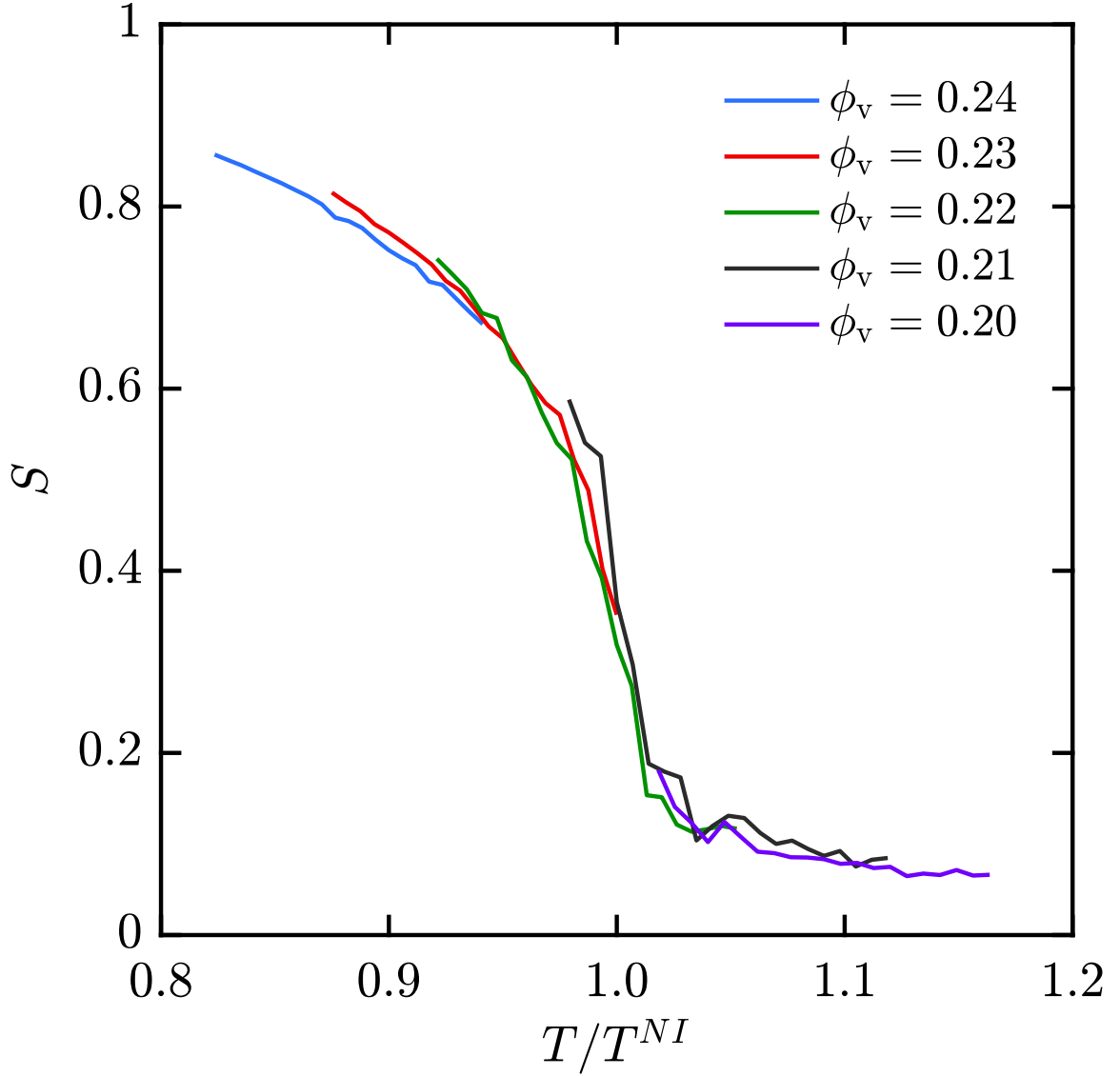
Figure 4.10. Nematic order parameter as a function of scaled temperature for various volume fractions at $300K$ illustrates universality in P_2. This is consistent with observations in Ref. 185. Due to finite size effects, P_2 does not equal zero in the isotropic regime.

4.4 Conclusion

We present a minimal model capturing the salient features of ionic chromonic liquid crystals. The interaction potential involves an anisotropic short range attraction and long range isotropic repulsion, which produces complex thermodynamic behavior consistent with experiments on lyotropic chromonic liquid crystals, including self–assembly at low concentrations into self–limiting stacks, isodesmic aggregation in dilute conditions and both chromonic N and M phases. Our model is capable of demonstrating the stacking defects in the chromonic phase which have been theorized to be present in real systems. This is particularly powerful given the simplicity of the proposed model. Importantly, we have shown the stack-size distribution to be broadly consistent with assumptions underlying many experiments, predicting a significant number of free mesogens exist within each phase, even at high densities.

Our work represents an important advancement in understanding the precise molecular requirements which give rise to chromonic phases. Importantly, through application of advanced free-energy sampling algorithms to obtain stacking free energies and elastic constants, our work has shown microscopically how a system can be both self-limiting *and* approximately isodesmic. The interplay of attractive forces, charge repulsion, and entropy implores further study and refinement of this model, particularly the inclusion of counterion models. We additionally have demonstrated how anisotropy of elastic constants begins to arise as stack length increases, presenting a base-line measurement for LCLCs which are dominated by small aggregates. As stack length is seen to be system-size agnostic, this is clearly a feature of the assembly properties of each mesogen and solvent conditions. Building on our basic model through tuning of these interactions, future work will fully unravel the molecular processes influencing stack structure and elasticity, enabling quantitative prediction of the response and phase behavior of LCLCs.

CHAPTER 5

IN SILICO MEASUREMENT OF ELASTIC MODULI OF NEMATIC LIQUID
CRYSTALS

5.1 Introduction

Though liquid crystals[32] (LCs) have long been central components of display
technologies,[102] their optically responsive and highly controllable nature has lead
to a host of emerging applications in nanoscale and colloidal templating,[186] or-
ganic electronics,[187] biosensing [188, 3], compact lenses,[168] and switchable diffrac-
tion gratings.[189] These applications rely on their ordering elasticity, which through
competition with applied fields and surface interactions can lead to topological de-
fects whose nature and structure is governed by a precise interplay.[41, 43, 190] The
balance between these different contributions to the free energy is apparent in the
morphologies adopted by confined liquid crystals,[114, 8, 191] where it is possible
to manipulate different variables to develop exquisitely sensitive systems for sensing
applications;[7, 3] a properly chosen liquid crystal can in fact be balanced on a knife's
edge, ready for a vanishingly small concentration of analyte to induce a mesoscopic
transformation, visible under standard crossed-polarizer optics. Precision engineer-
ing of such new devices requires an in-depth understanding of the elastic behavior of
the underlying liquid crystalline phases.

Here, we demonstrate that it is possible to rely on detailed molecular simulations
to predict the elastic moduli of nematic liquid crystals. By extending methods that
rely on real-space free-energy perturbations[75, 151] to utilize an accurate atomistic

force field,[192] we are able to characterize the elastic coefficients and their temperature dependence, including the elusive k_{24}. Our results lead to values consistent with Ericksen's bounds and in agreement with a subset of the experimental literature, implying that previously observed morphological instabilities in confined 5CB[35, 36] could have been due to inappropriate ansätze, surface effects or higher-order elastic moduli.

For the common case of apolar, achiral, and uniaxial nematic liquid crystals, the phase may be described by a local orientation vector $\hat{\mathbf{n}}$. In the absence of boundaries and external fields, this is a global vector. The local order, however, can be perturbed, leading to small distortions that incur a free energy penalty and a corresponding elastic restoring force. To order $(\nabla \hat{\mathbf{n}})^2$, the elastic free energy can be written as[32]

$$
\begin{aligned}
f = {} & \frac{1}{2}k_{11}\left(\nabla \cdot \hat{\mathbf{n}}\right)^2 + \frac{1}{2}k_{22}\left(\hat{\mathbf{n}} \cdot \nabla \times \hat{\mathbf{n}}\right)^2 + \frac{1}{2}k_{33}\left(\hat{\mathbf{n}} \times \nabla \times \hat{\mathbf{n}}\right)^2 \\
& + \frac{1}{2}\left(k_{22} + k_{24}\right)\left[\operatorname{Tr}\left(\nabla \hat{\mathbf{n}}\right)^2 - \left(\nabla \cdot \hat{\mathbf{n}}\right)^2\right] .
\end{aligned}
\tag{5.1}
$$

This expression contains the three most commonly used terms and their corresponding coefficients, or elastic moduli: splay (k_{11}), twist (k_{22}) and bend (k_{33}). The additional, divergence-like term ($\propto k_{22} + k_{24}$) is referred to as "saddle-splay". It penalizes bidirectional deformations, and can be defined so that the free energy is positive definite to quadratic order for all deformations as outlined by Ericksen.[39] An illustration of these elastic modes is presented in Figure 5.1. While originating from bulk interactions,[40] the saddle-splay may be transformed into a surface-like term in a global free energy integral by invoking Gauss's Law. For that reason, it has generally been overlooked in elastic studies,[32, 193] and it is only recently that studies of confined nematic LCs have unearthed its relevance. It likely contributes far more than initially believed, to the point where under some conditions it is suggested to lie outside the Ericksen bounds,[35, 37] a feature that hints at an incomplete understanding of elasticity within the framework of a Frank–Oseen description.

One implication of this is a spontaneous twisting of toroidal[36] or cylindrical[75] geometries, as depicted in Figs. 5.1 (d,e). It should be noted that for k_{24}, all published measurements have been indirect, and have relied either on elastic instability thresholds in various geometries or a fit to a continuum model that matches polarized microscope measurements.[41–43, 36, 37] This has lead to disagreements in the values of k_{24} reported in the literature.

It should be noted that the questions that surround elastic deformations go beyond k_{24}. Published values of k_{ii} reported in the literature are often in conflict, even for some of the most commonly studied nematic materials, such as 5CB.[194, 152, 195] Reported values were historically measured using the Fréederickz transition technique,[196] where elastic properties may be extracted from an instability threshold triggered by competitions between field-induced and surface-induced ordering. Such measurements may be coupled to optical measurements of the director distribution in order to determine both elastic ratios and the magnitudes of individual modes.[152] Direct torsional measurements have also been reported for k_{22},[194] and optical methods have been utilized for other elastic terms.[195] Importantly, for the particular case of k_{24}, all published measurements have been indirect, and have relied either on elastic instability thresholds in various geometries or a fit to a continuum model that matches polarized microscope measurements.[41–43, 36, 37] This has lead to wide disagreement for the values of k_{24} in the literature.
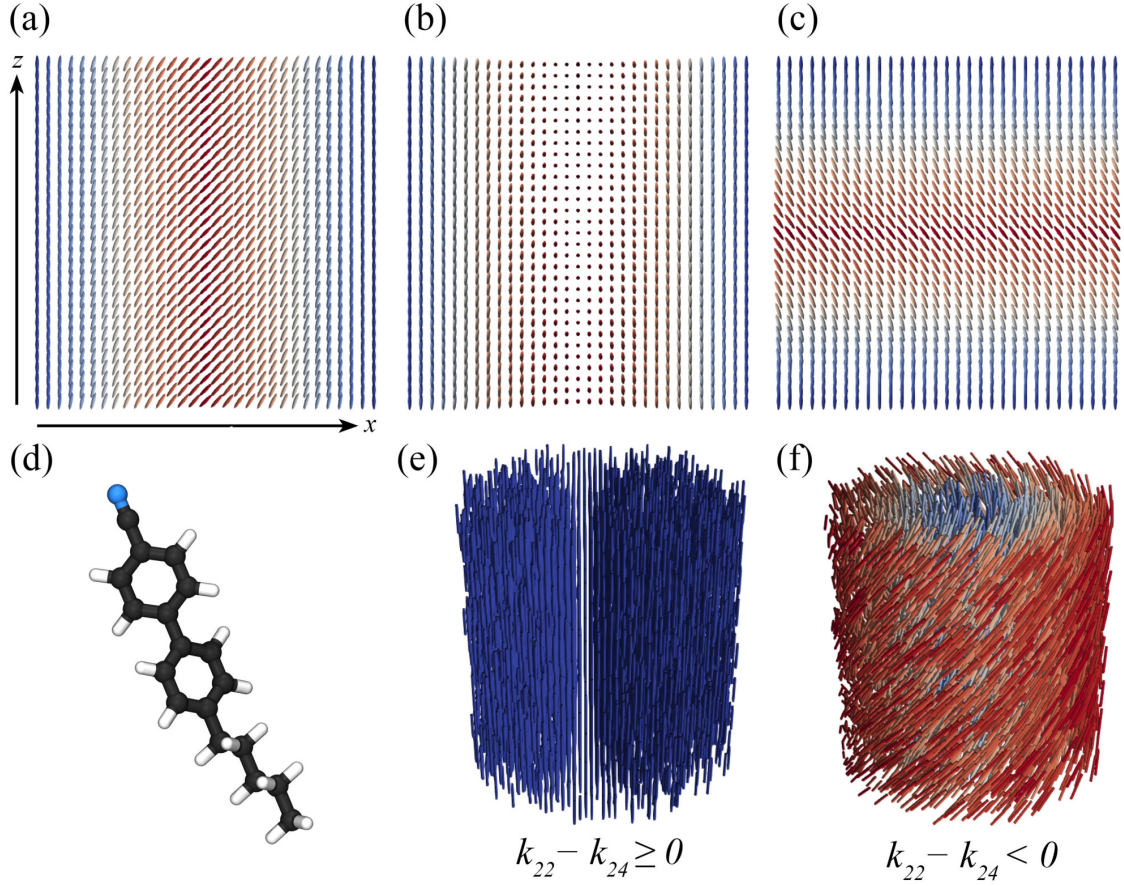
Figure 5.1. Top row shows idealized bulk elastic modes (a) splay (b) twist and (c) bend, which can be directly probed in experiment. Bottom row shows the 5CB molecule (d) and cylindrical twist deformations, which rely on the saddle-splay elastic constant k_{24}, in stable (e) and unstable (f) configurations under conditions of degenerate planar anchoring representative of the commonly studied 5CB–water interface. Saddle-splay is not directly measurable through experiment but can be inferred indirectly. The positive-definiteness of the elastic free energy expressed through the Ericksen bound $k_{22} - k_{24} \geq 0$ is thought to be violated for 5CB, though experiments are not conclusive.

The goal of this chapter is to present a direct method for calculation of the elastic moduli of nematic materials from molecular simulations of atomistically detailed

models, where predictions can be directly compared to experimental measurements. In such systems, the average orientation $\hat{\mathbf{n}}$ and degree of nematic alignment S are known and, as shown in this work, one can apply nanoscopic deformations to the material in order to excite distinct modes with extraordinary precision, thereby leading to direct, unambiguous characterization of all elastic moduli, including k_{24}. We hasten to note that past efforts to determine elastic coefficients of liquid crystals have focused on coarse-grained models.[62, 20] Certain features underlying liquid crystalline ordering,[197–199] however, are inaccessible without molecular specificity, and thus a set of experimentally-tuned atomistic force fields have been developed for in particular for the widely studied cyanobiphenyls,[192] as well as more general systems.[200] With such force fields, it has been possible to describe liquid crystal ordering with an extraordinary degree of precision, as revealed by comparison to x-ray reflectivity[199, 198] and NMR data [201], and by studies of the molecular structure within nematic disclinations.[197]

Building on the pioneering work of Cleaver and Allen,[77] several methods have been proposed to calculate the elastic constants of coarse-grained LC systems from molecular simulations. As useful as they have been, past methods have been hampered by limited accuracy, numerical complexity, or significant finite-size effects.[77, 148, 124] These limitations have prevented applications to atomistic systems without invoking theoretical assumptions that limit the reliability of the calculations. Indeed, in one of the few studies that considered a bulk model of 5CB, elastic constants were obtained using three different approaches, leading to significantly different elastic coefficients.[202] Though one set of predictions was found to be in good agreement with experimental measurements, it was regarded as "fortuitous" by the authors due to the crudeness of the underlying assumptions.[202] Another notable effort utilized a hybrid molecular field theory [203] to account for molecular flexibility from structures predicted by density functional theory (DFT) and geometry optimizations.

Good agreement with experiment was reported for the k_{ii} elastic constants of several 4-n-alkyl-4'-cyanobiphenyls (nCBs) and *para*–azoxyanisole. Unfortunately, that method cannot capture all molecular conformations and, in particular, the mutual arrangements that nearby molecules adopt in response to bi-directional deformations, which are essential to capturing k_{24}.

Recently, we proposed a new method [75] in which orientational perturbations and free energy sampling techniques are coupled to obtain elastic constants by exciting distinct modes within the Frank free energy formulation (Eqn. 5.1). The proposed method was shown to exhibit minimal sensitivity to finite size effects [75, 151], and was successfully applied to a broad range of Gay–Berne ellipsoids [151] and Lebwohl–Lasher lattice models.[76, 147] Here, we demonstrate the ability to directly predict *in silico* the elastic constants of an atomistic model of 5CB. This molecule is amongst the most widely studied and well characterized LCs. Despite its individual asymmetry, 5CB behaves largely as a uniaxial nematic. For the following investigations, we employ the force field of Tiberio and coworkers,[192] which has been validated against experimental data in a variety of situations.[199, 198, 201, 197] From our elastic measurements, we aim to gain additional insight into the relationship between molecular geometry and elasticity. More generally, we outline a computational methodology that in the future may be used for reliable screening of the elasticity of liquid crystalline materials for specific applications.

5.2 Computational Methods

5.2.1 Simulation details

All 5CB molecules were represented using the united atom forcefield parameterized by Tiberio et al. [192] to match experimental densities and nematic transition temperature. The model represents each non-hydrogen atom in 5CB using a

Lennard-Jones site. Partial charges are included in each atom, and torsional potentials are included to impart a conformation to the molecule that was inferred from electronic structure calculations. For raw parameters and a discussion of the methods utilized to obtain the forcefield, readers are referred there. To assist readers in reproducing the results within this paper, we have posted all Gromacs runfiles, topologies, and forcefields, in addition to the SSAGES advanced sampling input files and Python scripts used to generate all runs in a free online repository located at `https://github.com/hsidky/atomistic_elastics`. Further descriptions of the simulation protocols followed here are below.

Systems containing 400 5CB molecules are prepared for bulk elastic measurement by running 400 nanosecond NPT simulations at 1 atm in GROMACS [204] 5.1.3 from the reported transition temperatures [192] to $T_{NI} - 20$. A Langevin thermostat and Parrinello-Rahman barostat with $\tau_p = 5$ picoseconds were used with a time step of 2 femtoseconds for all simulations. The final average volumes at the respective temperatures are used to initiate a second set of NVT simulations with edge restrictions applied using a harmonic restraint with $k = 10^5$ kJ/mol in order to align the molecules along the $\hat{\mathbf{z}}$ axis. Four replicas of each point with different seeds are used to generate de-correlated trajectories for later use. Parabolic free energy profiles resulting from Basis Function Sampling are used to extract the desired elastic constant as $f = \frac{1}{2}\gamma k_{ii}\xi^2$, where γ is a geometric factor accounting for the finite restriction region.

The free energy perturbation approach requires an order parameter, ξ, to select for deformations that excite a particular elastic mode. We take ξ to be $\partial n_x/\partial x$ for splay, $\partial n_y/\partial x$ for twist, and $\partial n_x/\partial z$ for bend in a system that is constrained to orient along the $\hat{\mathbf{z}}$ axis at the periodic boundary. The director at the center of the box is then tilted using a bias applied to the chosen order parameter to produce chevron-like patters, resulting in a uniform- magnitude gradient between the restriction and bias

regions. Figures 5.2 (a)–(c) illustrate this approach in practice. A stiff harmonic potential is used to maintain alignment to the $\hat{\mathbf{z}}$ direction at the periodic boundaries of the box. A second region in the box center is actively biased along a chosen deformation ξ using an adaptive sampling method. Here we choose basis function sampling [76] (BFS), which is constructed in way such that material properties are easily extracted from the converged parabolic simulation bias. A similar approach is adopted for k_{24} by imposing a cylindrical geometry with degenerate planar anchoring and selecting ξ as $\partial n_\theta/\partial r$.[75]

For k_{24} measurements, we generate an initial cylinder containing 1600 5CB molecules using Packmol [205] with a diameter of approximately 12 nm and a height of 8.5 nm. Degenerate planar anchoring is also necessary to avoid spontaneous twist. This is accomplished by submerging the cylinder in water, as the 5CB-water interface is known to impart the requisite degenerate planar anchoring. 42,000 SPC/E water molecules are packed surrounding the cylinder corresponding to the appropriate density at 298 K. As with the bulk elastic measurements, a range of temperatures were chosen below the transition temperature and equilibrated for 200 ns at NPT conditions. The final averaged volumes were used to initiate single-walker simulations probing the $\partial n_\theta/\partial r$ deformation for 1 μs, utilizing 4 Nvidia 1080 Ti GPUs each.

5.2.2 Free energy perturbation

The free energy perturbation approach requires an order parameter, ξ, to select for deformations that excite a particular elastic mode. We take ξ to be $\partial n_x/\partial x$ for splay, $\partial n_y/\partial x$ for twist, and $\partial n_x/\partial z$ for bend in a system that is constrained to orient along the $\hat{\mathbf{z}}$ axis at the periodic boundary. The director at the center of the box is then tilted using a bias applied to the chosen order parameter to produce chevron-like patters, resulting in a uniform- magnitude gradient between the restriction and bias regions. Figures 5.2 (a)–(c) illustrate this approach in practice. A stiff harmonic

potential is used to maintain alignment to the $\hat{\mathbf{z}}$ direction at the periodic boundaries of the box. A second region in the box center is actively biased along a chosen deformation ξ using an adaptive sampling method. Here we choose basis function sampling [76] (BFS), which is constructed in way such that material properties are easily extracted from the converged parabolic simulation bias. A similar approach is adopted for k_{24} by imposing a cylindrical geometry with degenerate planar anchoring and selecting ξ as $\partial n_\theta / \partial r$.[75]

The elastic constants are measured by implementing the order parameter in the advanced sampling software suite, SSAGES.[206] Basis function sampling [76] is used with $N = 14$ Legendre polynomials to measure the free energy of director deformation over the interval $[-0.5, 0.5]$. Using the final de-correlated trajectories from the previous simulations, four walkers contribute to the overall free energy estimate. Simulations are carried out at NVT conditions for 1 μs at which point the polynomial coefficients converge to within $\mathcal{O}(10^{-6})$. The elastic constants are computed from the final free energy surface as previously described.

5.2.3 Liquid crystalline order parameter

For a uniaxial nematic, $\hat{\mathbf{n}}$ can be calculated as the eigenvector corresponding to the largest eigenvalue S of the $\mathbf{Q}$ tensor, where S is the scalar nematic order parameter. Using index notation, where Greek variables imply summation over the dimension,

$$Q_{\alpha\beta} = \frac{3}{2N} \sum_{i=1}^{N} u_\alpha^i u_\beta^i - \frac{1}{3}\delta_{\alpha\beta}. \tag{5.2}$$

Here, N is the number of molecules contributing to $\mathbf{Q}$ and u_α^i is orientation vector of molecule i and $\delta_{\alpha\beta}$ is the Kronecker delta operator. We choose to define u_α as the primary principal axis of each molecule, which is the eigenvector of the molecule inertial tensor ($\mathbf{I}$) with the highest degree of symmetry. This selection corresponds

to the eigenvector pair to the smallest eigenvalue of $\mathbf{I}$,

$$I_{\alpha\beta} = \sum_{i=1}^{M} m^i (\delta_{\alpha\beta} x_\gamma^i x_\gamma^i - x_\alpha^i x_\beta^i), \tag{5.3}$$

where M is the number of atoms in a molecule and x_γ^i are the Cartesian coordinates of atom i in the inertial frame. From this representation, the overall nematic director $\hat{\mathbf{n}}$ and order parameter S are easily determined. We note that while other definitions for the orientation vector could be used in our simulation [192], this definition has the benefit of applying torque to the molecule as a whole rather than to specific sites on the molecule, and thus avoids applying unphysical stretching to molecular conformations which could affect our measurements.

Biasing on flexible molecules, rather than the rigid bodies or rotors utilized in prior applications to coarse-grained systems [123, 75] necessitates a few important extensions. This has consequences for the precise definition of the biasing order parameter ξ and the application of bias and restriction forces. The original work [75] used a harmonic constraint on elements of the nematic $\mathbf{Q}$ tensor such that $Q_{xz}^2 + Q_{yz}^2 = 0$, an approach adapted from early studies by Allen et al. [123] intended to maintain the nematic director along $\hat{\mathbf{z}}$. However, such a restriction is unstable and may spontaneously split into a biaxial orientation while still satisfying the constraint [123]. Though no issues appear in standard simulations of Gay–Berne particles, molecular systems proved in practice to be highly susceptible to this phenomenon, resulting in insufficient orientational stability to sample the elastic free energy. Additionally, while in previous work orientations of the nematic vector could be obtained from averages over the molecular orientations in the regions of interest,[75] this is an approximation which requires correction after a converged surface is obtained.

Importantly, both of these compromises were introduced due to the difficulty of applying a bias directly to $\hat{\mathbf{n}}$. Molecular Dynamics requires that an order parameter

be differentiable with respect to the atomic coordinates enabling calculation of bias forces via the chain rule. Here, we address these issues by biasing on $\hat{\mathbf{n}}$ directly after obtaining it from the $\mathbf{Q}$ tensor [153]. Since we have connected the molecular orientations to the $\mathbf{Q}$ tensor elements in the previous section, what remains is to use this relation to connect molecular configurations to the force gradients in $\hat{\mathbf{n}}$ imposed by the bias potential. In the context of molecular dynamics, this necessitates the explicit gradient of $\hat{\mathbf{n}}$ with respect to the contributing atomic coordinates $\mathbf{x}^i$. We begin by deriving the gradient of an eigenvector v_α with respect to a symmetric matrix $A_{\gamma\delta}$, which is applicable to both $\mathbf{Q}$ and $\mathbf{I}$ tensors. The eigenvalue problem can be defined as follows:

$$A_{\alpha\beta}v_\beta^i = \lambda^i v_\alpha^i, \tag{5.4}$$

where $\lambda^i, \mathbf{v}^i$ are the ith eigenvalue/eigenvector pair. Taking $\mathbf{A}$ to be some function of $\mathbf{x}$ and differentiating, gives

$$\frac{\partial A_{\alpha\beta}}{\partial x_\gamma}v_\beta^i + A_{\alpha\beta}\frac{\partial v_\beta^i}{\partial x_\gamma} = \frac{\partial \lambda^i}{\partial x_\gamma}v_\alpha^i + \lambda^i\frac{\partial v_\alpha^i}{\partial x_\gamma}. \tag{5.5}$$

Recalling that the eigenvectors of a real symmetric matrix form an orthonormal basis, $v_\alpha^i \partial_{x_\beta} v_\alpha^i = \mathbf{0}$. Taking the inner product of Equation 5.5 w.r.t. v_γ^i reveals,

$$A_{\alpha\beta}\frac{\partial v_\beta^i}{\partial x_\gamma}v_\alpha^i = A_{\alpha\beta}\frac{\partial v_\alpha^i}{\partial x_\gamma}v_\beta^i = \lambda^i\frac{\partial v_\alpha^i}{\partial x_\gamma}v_\alpha^i = \mathbf{0},$$

which gives $\partial_{x_\gamma}\lambda^i = \partial_{x_\gamma}A_{\alpha\beta}v_\beta^i v_\alpha^i$. Repeating the inner product with $v_\alpha^j, j \neq i$, taking advantage of symmetry and using Equation 5.4 gives,

$$\frac{\partial A_{\alpha\beta}}{\partial x_\gamma}v_\beta^i v_\alpha^j + \lambda^j\frac{\partial v_\beta^i}{\partial x_\gamma}v_\beta^j = \lambda^i\frac{\partial v_\alpha^i}{\partial x_\gamma}v_\alpha^j. \tag{5.6}$$

Rearranging gives the final expression,

$$\frac{\partial v_\eta^i}{\partial x_\gamma} = \sum_{j \neq i} \frac{1}{\lambda^i - \lambda^j} \frac{\partial A_{\alpha\beta}}{\partial x_\eta} v_\beta^i v_\alpha^j v_\gamma^j. \tag{5.7}$$

The gradient of $\mathbf{Q}$ with respect to each orientation vector is

$$\frac{\partial Q_{\alpha\beta}}{\partial u_\gamma^i} = \frac{3}{2N} \left(u_\alpha^i \delta_{\gamma\beta} + u_\beta^i \delta_{\gamma\alpha} \right), \tag{5.8}$$

and $\mathbf{I}$ with respect to the atomic coordinates is

$$\frac{\partial I_{\alpha\beta}}{\partial x_\gamma^i} = m^i \left(2x_\gamma^i \delta_{\alpha\beta} - x_\alpha^i \delta_{\beta\gamma} - x_\beta^i \delta_{\alpha\gamma} \right). \tag{5.9}$$

Sorting the three eigenvalues for both tensors in ascending order, $j = 1, 2, 3$, and applying the chain rule to Equations 5.7 and 5.8 and 5.7 and 5.9 gives

$$\begin{aligned}
\frac{\partial n_\alpha^{(3)}}{\partial u_\beta^i} =& (\lambda^{(3)} - \lambda^{(1)})^{-1} \frac{3}{2N} \left(u_\gamma^i n_\gamma^{(1)} n_\alpha^{(3)} + u_\gamma^i n_\gamma^{(3)} n_\alpha^{(1)} \right) n_\beta^{(1)} + \\
& (\lambda^{(3)} - \lambda^{(2)})^{-1} \frac{3}{2N} \left(u_\gamma^i n_\gamma^{(2)} n_\alpha^{(3)} + u_\gamma^i n_\gamma^{(3)} n_\alpha^{(2)} \right) n_\beta^{(2)}
\end{aligned} \tag{5.10}$$

and

$$\begin{aligned}
\frac{\partial u_\alpha^{(1)}}{\partial x_\beta^i} =& (\lambda^{(3)} - \lambda^{(1)})^{-1} m^i \left(x_\gamma^i u_\gamma^{(3)} u_\alpha^{(1)} + x_\gamma^i u_\gamma^{(1)} u_\alpha^{(3)} \right) u_\beta^{(3)} + \\
& (\lambda^{(2)} - \lambda^{(1)})^{-1} m^i \left(x_\gamma^i u_\gamma^{(2)} u_\alpha^{(1)} + x_\gamma^i u_\gamma^{(1)} u_\alpha^{(2)} \right) u_\beta^{(2)}
\end{aligned} \tag{5.11}$$

respectively. Finally we define an function $\phi(\hat{\mathbf{n}})$ which selects out the appropriate deformation and represents the collective variable. For example, for the twist elastic mode k_{22}, $\phi(\hat{\mathbf{n}}) = n_\alpha \delta_{\alpha 2}$. Thus the complete gradient of ϕ with respect to the atomic

coordinates becomes:

$$\frac{\partial \phi}{\partial x_\alpha^i} = \frac{\partial \phi}{\partial n_\beta^{(3)}} \frac{\partial n_\beta^{(3)}}{\partial u_\gamma^{(1)}} \frac{\partial u_\gamma^{(1)}}{\partial x_\alpha^i}. \qquad (5.12)$$
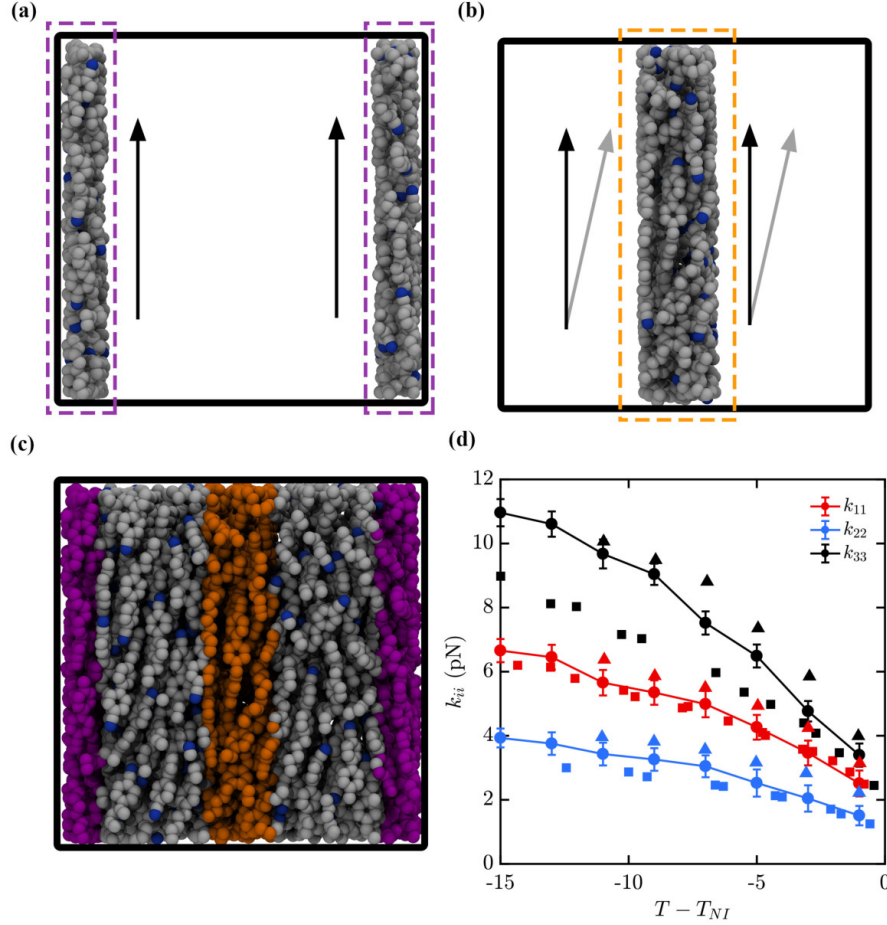
Figure 5.2. (a) A harmonic restraint is applied to the periodic edges of a simulation box in order to align the molecules in the $\hat{\mathbf{z}}$ direction. (b) Molecule orientations in the central region of the simulation box are biased using basis function sampling [76] according to the appropriate order parameter to excite the desired elastic mode. Shown here are arrows representing splay deformations from the non-perturbed state. (c) Over the course of a simulation, molecules enter and exit the respective regions. Only those molecules which lie within the regions shown in purple (edges) and orange (center) are biased. A gradient is produced across the box dimension as a result of the sampling and the corresponding free energy is calculated. The resulting bulk elastic coefficients (k_{ii}) for 5CB (d) are compared to experimental data from Madhusudana and Pratibha [152] (squares) and Chen and coworkers [195] (triangles). Connected circles represent elastic constant calculations using the methodology outlined in this work. Uncertainties are calculated using 1500 bootstrap cycles on the collected decorrelated samples.

5.3 Results and Discussion

We begin our studies by examining the standard bend, twist and splay elastic constants of 5CB, for which multiple measurements exist in the literature. We choose, for comparison, the results of Madhusudana and Pratibha [152] and Chen and coworkers,[195] which represent the span of available experimental elastic measurements for 5CB. After locating the nematic–isotropic transition temperature T_{NI}, we proceed to measure elastic coefficients at a range of temperatures down to 15°C below T_{NI}. The 5CB model in question has been parameterized to accurately represent the thermodynamics of the nematic–isotropic transition, including appropriate densities and orientational order. Strikingly, though elastic behavior is not included in this parameterization, the measured coefficients we obtain (see Figure 5.2 (d)) lie directly on top of the experimental data range, intercalating the high and low estimates, when plotted as a function of $T - T_{NI}$. It should be noted that the actual transition temperature predicted by this model is slightly higher (by two degrees) than the experimental value. This is suggestive that elasticity of a molecular model may be accurately obtained from modest thermodynamic parameterizations, and may be controlled primarily by molecular topology and flexibility, as is presumed in single-molecule in mean-field models.[203]

Having established the validity of the proposed method, we proceed to apply the free energy perturbation technique to obtain k_{24}. It is convenient to work in a cylindrical geometry to isolate the *normal* twist mode,[40] which is directly analogous to double-twist arrangements observed in blue phases and toroidal geometries. Here, a larger system is required to achieve a stable cylinder with sufficient diameter to probe the normal twist mode. To ensure that only this mode is probed, one must remove the effects of surface interactions from the free energy profile. It is sufficient to choose a system that has degenerate planar anchoring, so that any preferred surface orientations are imposed only by the bulk nematic order. It is well known, and

has been validated in simulations,[198] that aqueous interfaces impose exactly this type of anchoring. Hence, we embed a periodic cylinder of liquid crystal within a solvent of SPC/E water.[207] A typical configuration of this cylindrical geometry is given in Fig. 5.3(a). The presence of an interface, while not affecting orientation, nevertheless imposes order on the 5CB cylinder, effectively shifting T_{NI} by ≈ 5 K (see Fig 5.3(b)) while retaining similar ordering behavior [plotted as $S(T)$ in Fig. 5.3(b)] as a function of relative temperature. Hence, to relate these measurements to bulk elastic constants, we compare values at equivalent $T - T_{NI}$.
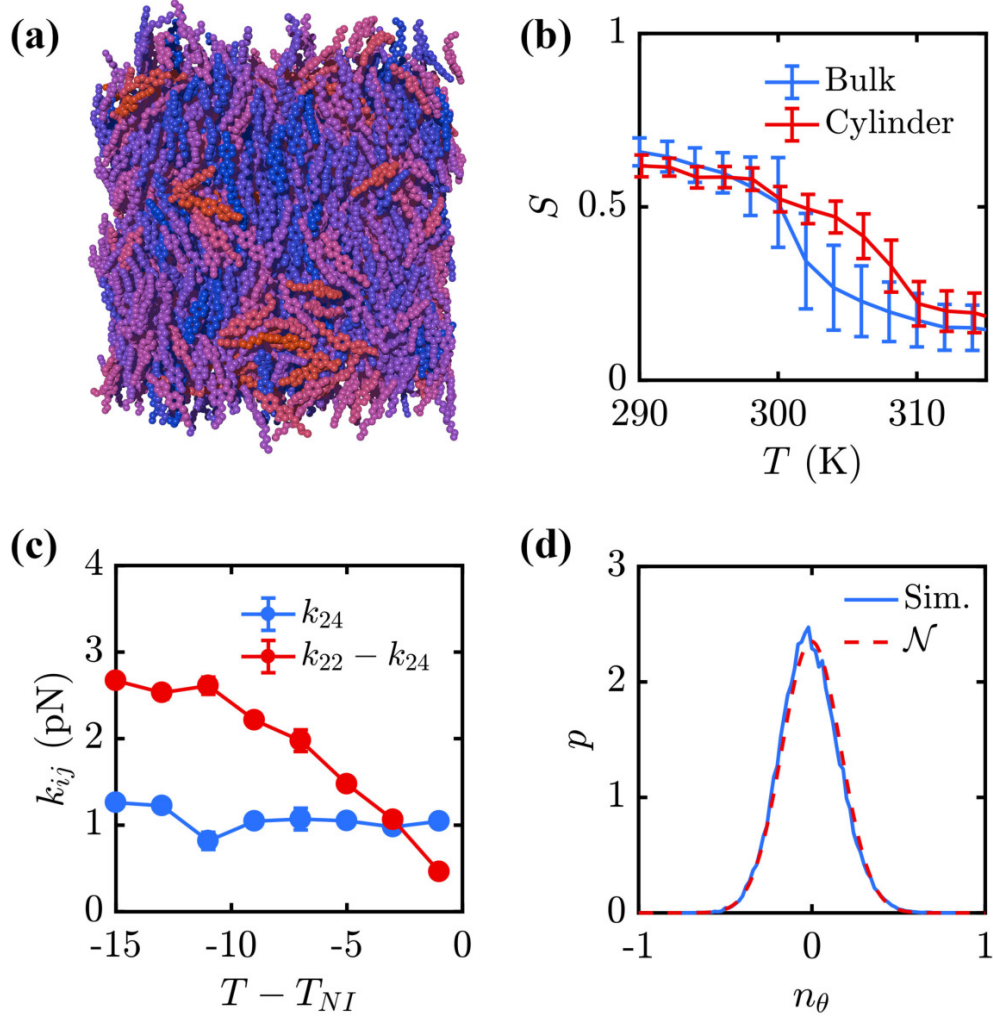
Figure 5.3. Snapshot of 5CB cylindrical system (a) with solvent removed. Due to finite anchoring-induced ordering within cylinder, the transition temperature T_{NI} is shifted slightly (b) by ≈ 5K. Calculated saddle-splay surface-like elastic constant (k_{24}) for 5CB (c) shows no violation of the Ericksen bound, delineated by $k_{22} - k_{24} \geq 0$. To validate k_{24} stability, we test the unbiased director probability distribution $p(n_\theta)$ against the normal distribution (d) using a Kolmogorov–Smirnov test (representative data at 296 K shown; distributions obtained at other temperatures are plotted in Figure 5.4) Uncertainties in the elastic measurements are estimated using 1500 bootstrap cycles on the collected decorrelated samples, yielding error bars comparable to the size of the points. Roughness in trendlines is not due to statistical uncertainty of each measurement, but instead due to underlying fluctuations in nematic order and volume that arise under NPT preparation.

105

The measured k_{24} elastic constants are shown in Figure 5.3(c). It is apparent that the Ericksen bound $k_{22} - k_{24} \geq 0$ remains valid across the nematic range. This is a striking result, as indirect measurements in toroidal droplets,[36] escaped radial morphologies,[43] and aperiodic nematic films [42] yield a value for k_{24} for which the normal modes of deformation[40] are either nearly zero or in violation of the Ericksen bound. From our calculations, saddle-splay retains a finite value throughout the nematic range that is, surprisingly, essentially constant. While this appears to be at odds with the behavior of most elastic coefficients near the nematic–isotropic transition, it is important to note that k_{24} never appears by itself within expressions for bidirectional modes,[40] and that the cost of the bidirectional twist does trend toward zero, as one expects, when disorder is approached. Importantly, the approach of $k_{22} - k_{24}$ to zero may help explain some experimental observations, which are typically conducted at temperatures near T_{NI}. Our measurements also contradict the predictions made for 5CB using a hybrid molecular field theory [203] (MFT), which suggested that k_{24} varies significantly over the nematic range, and even predicted the value to switch sign at a crossover temperature of $T - T_{NI} \approx -7$. Since that theory predicts k_{22} commensurate with experiments, this indicates *non-vanishing* normal twist as the transition temperature is approached. The differences in the present work and MFT predictions could be due to to the underlying assumptions of MFT, which does not capture spatial dependencies and mutual deformations that play an important role in k_{24}. The k_{24} calculations reported here are significant in that saddle-splay contributions to the free energy play a critical role in stabilizing defects[190] and affect morphological transitions.[114] That we observe no lack of positive-definiteness in our measurement suggests that the origin of spontaneous radial[35] and double-twist[36] morphologies observed in experiments on 5CB must be revisited.
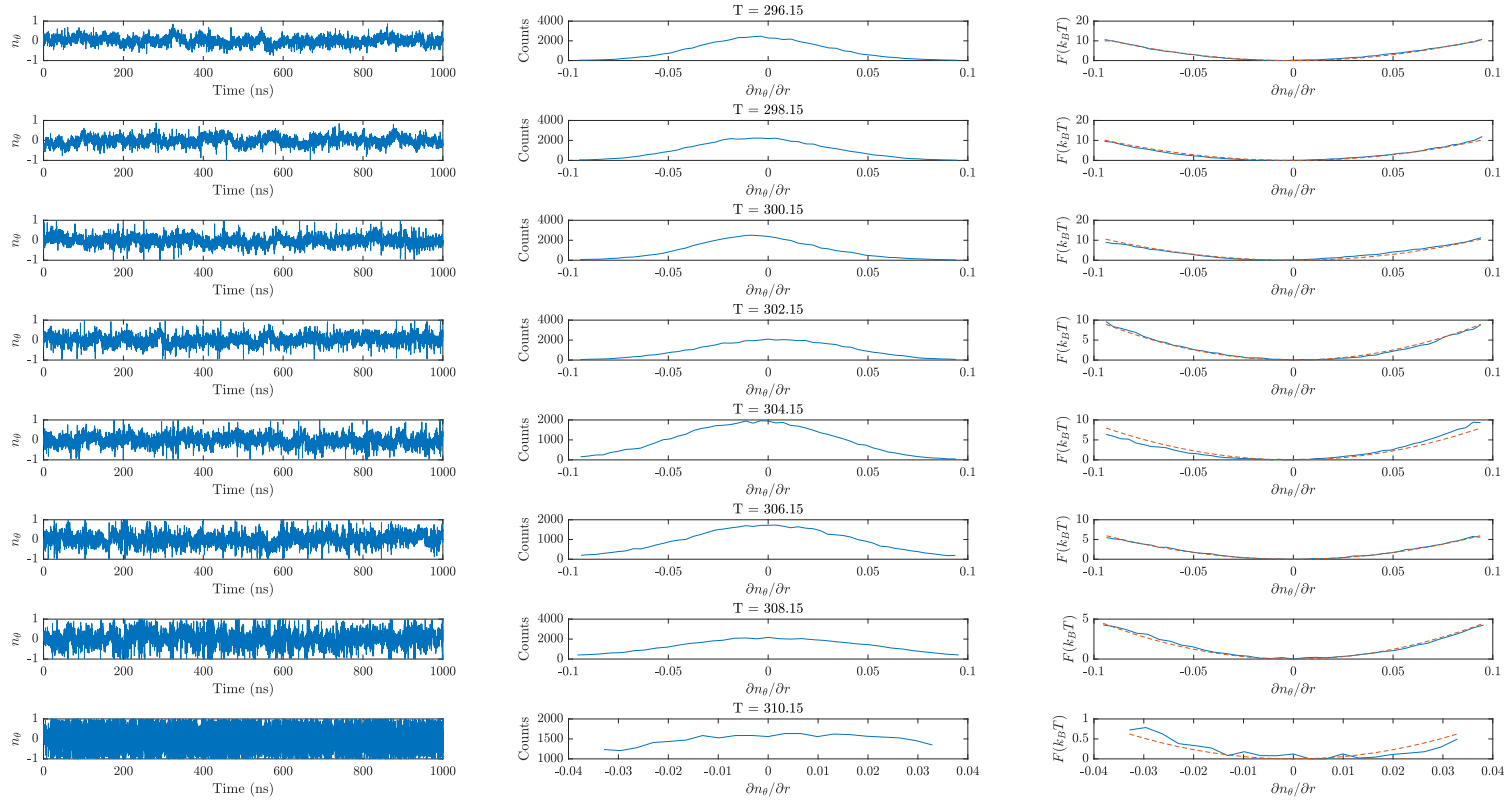
Figure 5.4. Data from simulations probing the k_{24} elastic coefficient. The three columns show: evolution of the order parameter n_θ over the course of the simulation (left), the unbiased histogram acquired over $\partial_r n_\theta$ (center), and the resulting free energy and P_2 projection (right).

We emphasize again that, to our knowledge, published experimental measurements of k_{24} are indirect, and utilize an ansatz to extract a result. In contrast, we directly simulate 5CB using a molecular model that has been parameterized to match experimental densities and orientational order, and report bulk (k_{ii}) elastic constants that are in full agreement with experiment. Hence, we were able to use the predictive power of molecular simulations to obtain a quantity that has proved elusive experimentally. As this prediction contradicts mechanisms hypothesized in experiment, it is important that we rigorously support the results of our simulations. To rule out the possibility that pre-transitional ordering induced by anchoring or spatial inhomogeneity result in misleading measurements, we also plot the radial profiles of the nematic director within each cylinder at all studied temperatures in Fig. 5.5 and show that they are linear. We also generate unbiased distributions of the director fluctuations in the outer annulus of each cylinder and perform a one-sample Kolmogorov–Smirnov test at a 1% significance level against a centered normal distribution. A representative data set at $T = 296$K is shown in Fig. 5.3(d). All samples reject the null hypothesis, which indicates that there is no statistically detectable metastability at non-zero deflection. We include all director time profiles, resulting distributions, and parabolic free energy profiles with P_2 projections in Figure 5.4.

One might also object to our k_{24} measurements on the basis of finite size effects. The free energy perturbation approach adopted here has been shown [75, 151] to be insensitive to finite size effects, particularly in bulk measurements.[151] This is supported by the striking agreement of our k_{ii} measurements with experiment. However, k_{24} is measured in cylindrical confinement, which may exhibit different scaling behavior. While an explicit study of finite size effects on k_{24} is currently intractable due to immense computational costs, we propose that it is not relevant for the broader observation that Ericksen's equalities are satisfied. Finite-size scaling may change the absolute magnitude of the reported values, but will not change
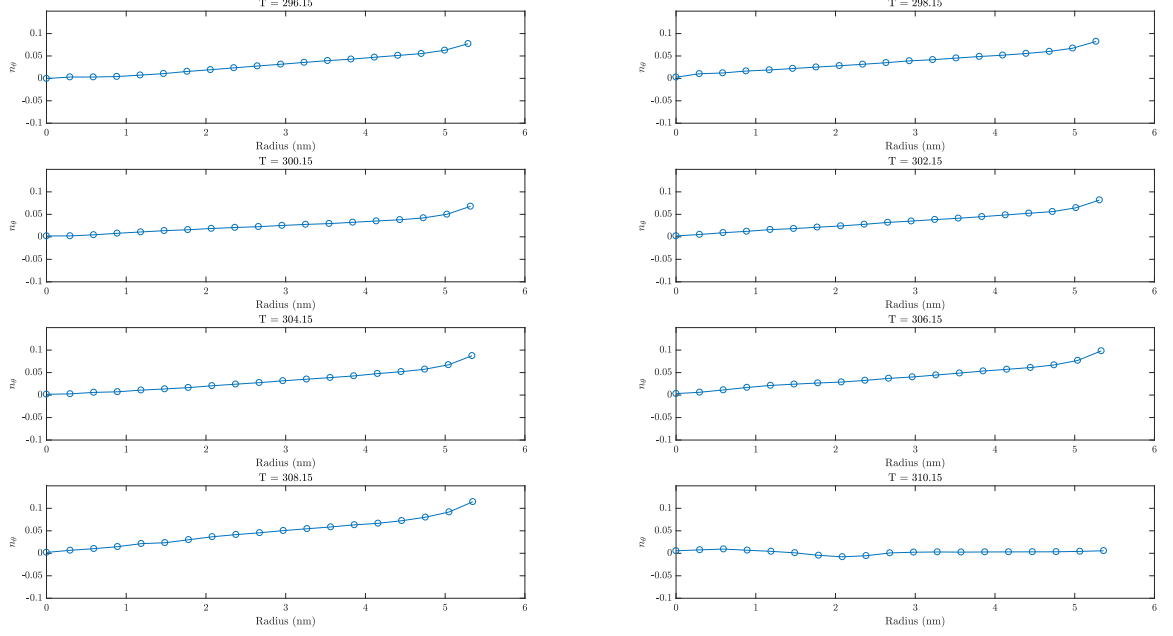
Figure 5.5. Radial profile of n_θ averages in 5CB cylinders show approximately linear behavior across the sample region.

the stable morphology—the cylinder either is or is not unstable to twisting. Unlike prior coarse-grained studies, which found no appreciable free energy penalty to twisting[75], and experiments and theory demonstrating twisting in toroidal geometries is similarly not penalized[36, 38], these results demonstrate that k_{24}-containing modes have a positive-definite free energy for 5CB.

5.4   Conclusions

Our methods and calculations serve to shed light into some long-standing concerns about the experimental value of k_{24} and its role in driving morphology transitions in confined systems.[191, 36, 42, 35, 43] However, in doing so, we have opened up new questions about the true reason for such striking morphologies. If k_{24} is not responsible, then what is? Perhaps there are important third or fourth-order terms that

arise to stabilize spontaneous deformations. Perhaps anchoring and explicit solution chemistry play a larger role than previously appreciated. Regardless, our calculations represent a useful milestone in material property prediction. We demonstrate that it is possible to predict bulk elastic constants in agreement with experiment for a molecular system from simulation, and we provide the only direct measurements of saddle-splay k_{24} for the otherwise extensively characterized 5CB. With these new developments, the tools are in place to begin unraveling the role of higher order elastic coefficients and subtle anchoring behaviors across the landscape of liquid-crystalline materials. A key challenge will be the calculation of the L_{ij} elastic coefficients utilized in the Landau–de Gennes $\mathbf{Q}$-tensor formalism, which are not directly accessible to experiment, and are not directly mappable onto the Frank elastic theory.[208] In each of these arenas, the methodology and framework employed here provide a foundation for computer-aided characterization and design of novel mesogenic compounds.

CHAPTER 6

CONCLUDING REMARKS AND FUTURE OUTLOOK

The work in this dissertation represents the development and extension of new methods which combine advanced sampling and molecular simulation to predict the elastic properties of liquid crystals. Existing techniques utilizing molecular simulation often rely on equilibrium simulations and numerical analyses which are inherently inaccurate or scale poorly with system size. As a consequence, systematic studies of coarse-grained systems or any realization of a molecular system were intractable. Enhanced sampling methods accelerate the occurrence of rare events, thus providing a means by which free energetic perturbations can be applied and measured. By correcting and expanding the formalism proposed by Joshi et al. [75], it becomes possible to directly estimate the bulk elastic moduli of liquid crystals using both Monte Carlo and molecular dynamics. Furthermore, the surface-like saddle-splay elastic constant k_{24}, which is not directly measurable in experiment, can be estimated in cylindrical geometries. This dissertation develops this methodology through a series of increasingly complex coarse-grained and atomistic simulations.

The first study in this dissertation begins with a comprehensive study of binary liquid crystal mixtures represented by the multicomponent Lebwohl-Lasher lattice model. Density-of-states simulations are used to characterize the complete binary phase diagram, including nematic-nematic phase separation predicted by mean-field theories, but previously not observed in simulations. Mapping this phase diagram permits detailed study of elastic properties across the miscible nematic region. Importantly, we observe local phase separation and disordering driven by the application

111

of small linear perturbations near the transition temperature and more significantly through nonlinear stresses. These findings are of key importance in systems of blended nematics which contain particulate inclusions, or are otherwise confined.

The second study uses density-of-states simulations to systematically study the elastic properties of four common Gay–Berne nematogenic models; two with a length-to-diameter ratio $\kappa = 3$ [(3, 5, 1, 2) and (3, 5, 1, 3)], a model with $\kappa = 4.4$ parameterized for p-terphenyl (4.4, 20, 1, 1), and a discogen with $\kappa = 0.345$ (0.345, 0.2, 1, 2). In accordance with previous measurements, we find that for $\kappa = 3$, models, $k_{22} \lesssim k_{11} < k_{33}$. We find the latter two models in particular accurately capture the experimentally measured elastic ratios in apolar achiral systems. The (4.4, 20, 1, 1) model reproduces the elastic constant ratios of p–azoxyanisole remarkably well, and maps to within 30% of the absolute. The (0.345, 0.2, 1, 2) model elastic constants exhibits an unusual temperature dependence similar to recent experimental studies. We find $k_{11} \approx k_{22} > k_{33}$, in line with theoretical predictions. All models deviate from the mean-field expectation $k_{ii} \propto S^2$. These results represent a crucial first step toward quantitatively accurate coarse-grained liquid crystalline models of self-assembly and response, enabling one to choose a Gay–Berne model based its measured elastic ratios rather than just its shape and energy anisotropy.

The third study investigates chromonic liquid crystals which exhibit a unique self–assembly process that is of both theoretical and practical interest. A characteristic feature of chromonics is the occurrence of molecular association through stacking at extremely low concentrations. Concomitantly, these phases exhibit a separation of energy scales for elastic deformations that leads to novel bulk morphologies and defect arrangements. Experimental evidence has suggested that this process is approximately isodesmic across a broad concentration range. To date, only a handful of computational studies have managed to reproduce crucial aspects of chromonic phases, with ionic chromonics treated only by expensive fully atomistic

simulations. We present a simple model based on the competition between long-range repulsions and short range anisotropic attractions capable of capturing all features of the chromonic phase. Molecular simulations of coarse-grained mesogens are used to map out the phase behavior and explore how structural and energetic anisotropies influence their ordering and response. This study also presents the first computational investigation into the nematic elasticity of these phases, and demonstrates key correlations between elastic response and stack growth.

Finally, the fourth study challenges experiments on confined droplets of the nematic liquid crystal 5CB, which have questioned long-established bounds imposed on the elastic free energy of nematic systems. This elasticity, which derives from molecular alignment within nematic systems, is quantified through a set of moduli which can be difficult to measure experimentally and, in some cases, can only be probed indirectly. This is particularly true of the surface-like saddle-splay elastic term, for which the available experimental data indicate values on the cusp of stability, often with large uncertainties. We demonstrate that all nematic elastic moduli, including the saddle-splay elastic constant k_{24}, may be calculated directly from atomistic molecular simulation. Importantly, results obtained through *in silico* measurements of the 5CB elastic properties demonstrate unambiguously that saddle-splay elasticity alone is unable to describe the observed confined morphologies.

Much work remains to be done in the domain of elastic property prediction from molecular simulation. Our binary mixture studies were performed using a model potential and would certainly benefit from molecular specificity. Elastic segregation effects are known to have profound implications for systems with a small component of 'dopant' species exhibiting stronger or weaker elasticity added to alter response behavior in many industrial blends. Further, we expect induced compositional differences to be particularly relevant for nanoparticle self-assembly or templated polymerization where defects may be used to guide the formation of complex heterostructures.

Molecular simulation provides an ideal way to control mixture composition and system geometry while elastic properties are estimated.

The techniques presented also facilitate explicit accounting for elastic properties which can be used in future LC model development, yielding accurate potentials that can capture complex ordering phenomena, LC–collodial interactions and naonconfined morphologies. In principle, it becomes possible to combine machine learning techniques with elastic property prediction to engineer, *in silico*, new LC molecules that exhibit chosen elastic properties. Achieving this may dramatically improve the ability to design highly responsive and selective LC devices, as a broad chemical space can be explored with minimal human intervention. Of course, such large-scale simulations are only possible if the cost of elasticity measurements is substantially reduced. Currently, up to 4 μs of simulation runtime is required to generate a reliable estimate of a single elastic mode at a single temperature. Using newer advanced sampling algorithms or utilizing transfer learning techniques may significantly reduce this time.

There remain a wide variety of systems that can be explored using the methods developed in these studies. Our coarse–grained studies of chromonic LCs indicate that a large elastic anisotropy is not necessary for LCs to display the hallmarks of the chromonic phase. However, the reason for this remains unclear. Studying the elastic properties of chromonic LCs using an atomistic model may provide new insight into the precise molecular underpinnings behind the elastic anisotropy and its role in chromonic self-assembly — a longstanding question in the field. Other exotic liquid crystals such as bent-core mesogens or polar compounds that give rise to novel mesophases are of great interest and can be studied. In particular, the apparent inability of the Frank elastic free energy formalism to predict a stable ground state for these phases can be quantified in detail. A key challenge will also be the calculation of the L_{ij} elastic coefficients utilized in the Landau–de Gennes $\mathbf{Q}$-tensor formalism,

which are not directly accessible to experiment, and are not directly mappable onto the Frank elastic theory.

The studies presented in this dissertation are only the beginning of what we anticipate will be a very fruitful endeavor. The techniques and software now exist which position molecular simulation as a first-class tool for the study of liquid crystal elasticity. What remains is for the algorithms to be optimized and applied to new and more interesting systems.

BIBLIOGRAPHY

1. M. Schadt. Liquid crystal materials and liquid crystal displays. *Annu. Rev. Mater. Sci.*, 27(1):305–379, 1997.

2. K.-H. Kim and J.-K. Song. Technical evolution of liquid crystal displays. *NPG Asia Mater.*, 1(1):29–36, 2009.

3. R. J. Carlton, J. T. Hunter, D. S. Miller, R. Abbasi, P. C. Mushenheim, L. N. Tan, and N. L. Abbott. Chemical and biological sensing using liquid crystals. *Liq. Cryst. Rev.*, 1(1):29–51, 2013.

4. S. J. Woltman, G. D. Jay, and G. P. Crawford. Liquid-crystal materials find a new order in biomedical applications. *Nat. Mater.*, 6(12):929–938, 2007.

5. M. Khan, Y. Kim, J. H. Lee, I.-K. Kang, and S.-Y. Park. Real-time liquid crystal-based biosensor for urea detection. *Anal. Methods*, 6:5753–5759, 2014.

6. H. Tan, X. Li, S. Liao, R. Yu, and Z. Wu. Highly-sensitive liquid crystal biosensor based on {DNA} dendrimers-mediated optical reorientation. *Biosens. Bioelectron.*, 62(0):84–89, 2014.

7. I.-H. Lin, D. S. Miller, P. J. Bertics, C. J. Murphy, J. J. de Pablo, and N. L. Abbott. Endotoxin-induced structural transformations in liquid crystalline droplets. *Science*, 332(6035):1297–1300, 2011.

8. D. S. Miller and N. L. Abbott. Influence of droplet size, ph and ionic strength on endotoxin-triggered ordering transitions in liquid crystalline droplets. *Soft Matter*, 9:374–382, 2013.

9. H. K. Bisoyi and S. Kumar. Liquid-crystal nanoscience: an emerging avenue of soft self-assembly. *Chem. Soc. Rev.*, 40:306–319, 2011.

10. J. A. Moreno-Razo, E. J. Sambriski, N. L. Abbott, J. P. Hernández-Ortiz, and J. J. de Pablo. Liquid-crystal-mediated self-assembly at nanodroplet interfaces. *Nature*, 485(7396):86–89, 2012.

11. I. Mušević, M. Škarabot, U. Tkalec, M. Ravnik, and S. Žumer. Two-dimensional nematic colloidal crystals self-assembled by topological defects. *Science*, 313 (5789):954–958, 2006.

12. M. Cavallaro Jr, M. A. Gharbi, D. A. Beller, S. Čopar, Z. Shi, R. D. Kamien, S. Yang, T. Baumgart, and K. J. Stebe. Ring around the colloid. *Soft Matter*, 9(38):9099–9102, 2013.

13. D. A. Beller, M. A. Gharbi, and I. B. Liu. Shape-controlled orientation and assembly of colloids with sharp edges in nematic liquid crystals. *Soft matter*, 11 (6):1078–1086, 2015.

14. M. Rahimi, T. F. Roberts, J. C. Armas-Pérez, X. Wang, E. Bukusoglu, N. L. Abbott, and J. J. de Pablo. Nanoparticle self-assembly at the interface of liquid crystal droplets. *Proc. Natl. Acad. Sci.*, 112(17):5297–5302, 2015.

15. M. B. Pandey, P. J. Ackerman, A. Burkart, T. Porenta, S. Žumer, and I. I. Smalyukh. Topology and self-assembly of defect-colloidal superstructure in confined chiral nematic liquid crystals. *Phys. Rev. E*, 91:012501, 2015.

16. X. Wang, D. S. Miller, E. Bukusoglu, J. J. de Pablo, and N. L. Abbott. Topological defects in liquid crystals as templates for molecular self-assembly. *Nat. Mater.*, 15(1):106–112, 2016.

17. L. Onsager. The effects of shape on the interaction of colloidal particles. *Ann. N. Y. Acad. Sci.*, 51(4):627–659, 1949.

18. W. Maier and A. Saupe. Eine einfache molekular-statistische Theorie der nematischen kristallinflüssigen Pase. Teil 1. *Z. Naturforsch.*, 15A(10):882–889, 1959.

19. W. Maier and A. Saupe. Eine einfache molekular-statistische T h e o r i e der nematischen kristallinflüssigen Phase . Teil II. *Z. Naturforsch.*, 14A:287–292, 1960.

20. J. G. Gay and B. J. Berne. Modification of the overlap potential to mimic a linear sitesite potential. *J. Chem. Phys.*, 74(6):3316–3319, 1981.

21. J. Pelaez and M. Wilson. Molecular orientational and dipolar correlation in the liquid crystal mixture e7: a molecular dynamics simulation study at a fully atomistic level. *Phys. Chem. Chem. Phys.*, 9:2968–2975, 2007.

22. F. Chami and M. R. Wilson. Molecular order in a chromonic liquid crystal: A molecular simulation study of the anionic azo dye sunset yellow. *J. Am. Chem. Soc.*, 132(22):7794–7802, 2010.

23. A. V. Komolkin, A. Laaksonen, and A. Maliniak. Molecular dynamics simulation of a nematic liquid crystal. *J. Chem. Phys.*, 101(5):4103–4116, 1994.

24. G. R. Luckhurst and S. Romano. Computer simulation study of a nematogenic lattice model based on an elastic energy mapping of the pair potential. *Liq. Cryst.*, 26(6):871–884, 1999.

25. J. K. Whitmer, X. Wang, F. Mondiot, D. S. Miller, N. L. Abbott, and J. J. de Pablo. Nematic-field-driven positioning of particles in liquid crystal droplets. *Phys. Rev. Lett.*, 111(22):227801, 2013.

26. S. I. Hernandez, J. A. Moreno-Razo, A. Ramirez-Hernandez, E. Diaz-Herrera, J. P. Hernandez-Ortiz, and J. J. de Pablo. Liquid crystal nanodroplets, and the balance between bulk and interfacial interactions. *Soft Matter*, 8(5):1443–1450, 2012.

27. G. Skacej and C. Zannoni. Molecular simulations elucidate electric field actuation in swollen liquid crystal elastomers. *Proc. Natl. Acad. Sci.*, 109(26): 10193–10198, 2012.

28. M. R. Wilson. Progress in computer simulations of liquid crystals. *Int. Rev. Phys. Chem.*, 24(3-4):421–455, 2005.

29. J. Karjalainen, J. Lintuvuori, V.-V. Telkki, P. Lantto, and J. Vaara. Constant-pressure simulations of Gay-Berne liquid-crystalline phases in cylindrical nanocavities. *Phys. Chem. Chem. Phys.*, 15:14047–14057, 2013.

30. L. D. Landau and E. Lifshitz. *Course of Theoretical Physics Vol 7: Theory of Elasticity.* Pergamon Press, 1959.

31. F. C. Frank. I. liquid crystals. on the theory of liquid crystals. *Discuss. Faraday Soc.*, 25:19–28, 1958.

32. I. Stewart. *The static and dynamic continuum theory of liquid crystals : a mathematical introduction.* Taylor & Francis, London New York, N.Y, 2004. ISBN 9780748408962.

33. C. Oseen. The theory of liquid crystals. *Trans. Faraday Soc.*, 29(l):883–889, 1933.

34. M. Kleman and O. D. Lavrentovich. *Soft Matter Physics: An Introduction.* Springer-Verlag New York, 1 edition, 2003. ISBN 978-0-387-95267-3.

35. J. Gupta, S. Sivakumar, F. Caruso, and N. Abbott. Size-dependent ordering of liquid crystals observed in polymeric capsules with micrometer and smaller diameters. *Angew. Chem. Int. Ed.*, 48(9):1652–1655, 2009.

36. E. Pairam, J. Vallamkondu, V. Koning, B. C. van Zuiden, P. W. Ellis, M. A. Bates, V. Vitelli, and A. Fernandez-Nieves. Stable nematic droplets with handles. *Proc. Natl. Acad. Sci.*, 110(23):9295–9300, 2013.

37. Z. S. Davidson, L. Kang, J. Jeong, T. Still, P. J. Collings, T. C. Lubensky, and A. Yodh. Chiral structures and defects of lyotropic chromonic liquid crystals induced by saddle-splay elasticity. *Phys. Rev. E*, 91(5):050501, 2015.

38. V. Koning, B. C. van Zuiden, R. D. Kamien, and V. Vitelli. Saddle-splay screening and chiral symmetry breaking in toroidal nematics. *Soft Matter*, 10 (23):4192–4198, 2014.

39. J. Ericksen. Inequalities in liquid crystal theory. *Phys. Fluids (1958-1988)*, 9 (6):1205–1207, 1966.

40. V. H. Schmidt. Normal-distortion-mode approach to liquid crystal elastic energy. *Phys. Rev. Lett.*, 64(5):535–538, 1990.

41. D. W. Allender, G. P. Crawford, and J. W. Doane. Determination of the liquid-crystal surface elastic constant k_{24}. *Phys. Rev. Lett.*, 67:1442–1445, 1991.

42. A. Sparavigna, O. D. Lavrentovich, and A. Strigazzi. Periodic stripe domains and hybrid-alignment regime in nematic liquid crystals: Threshold analysis. *Phys. Rev. E*, 49(2):1344–1352, 1994.

43. R. D. Polak, G. P. Crawford, B. C. Kostival, J. W. Doane, and S. Žumer. Optical determination of the saddle-splay elastic constant k_{24} in nematic liquid crystals. *Phys. Rev. E*, 49:R978–R981, 1994.

44. M. Ravnik and S. Žumer. Landau–de Gennes modelling of nematic liquid crystal colloids. *Liq. Cryst.*, 36(10-11):1201–1214, 2009.

45. J. Lydon. Chromonic mesophases. *Curr. Opin. Colloid Interface Sci.*, 8(6): 480–490, 2004.

46. H.-S. Park and O. D. Lavrentovich. *Lyotropic Chromonic Liquid Crystals: Emerging Applications*. John Wiley & Sons: Hoboken, NJ, 2012.

47. J. Lydon. Chromonic liquid crystalline phases. *Liq. Cryst.*, 38(11-12):1663–1681, 2011.

48. H. S. Park, S. W. Kang, L. Tortora, Y. Nastishin, D. Finotello, S. Kumar, and O. D. Lavrentovieh. Self-assembly of lyotropic chromonic liquid crystal sunset yellow and effects of ionic additives. *J. Phys. Chem. B*, 112(51):16307–16319, 2008.

49. H.-S. Park, S.-W. Kang, L. Tortora, S. Kumar, and O. D. Lavrentovich. Condensation of Self-assembled Lyotropic Chromonic Liquid Crystal Sunset Yellow in Aqueous Solutions Crowded With Polyethylene Glycol and Doped With Salt. *Langmuir*, 27(7):4164–75, 2011.

50. L. Tortora, H.-S. Park, S.-W. Kang, V. Savaryn, S.-H. Hong, K. Kaznatcheev, D. Finotello, S. Sprunt, S. Kumar, and O. D. Lavrentovich. Self-assembly, Condensation, and Order in Aqueous Lyotropic Chromonic Liquid Crystals Crowded With Additives. *Soft Matter*, 6(I):4157, 2010.

51. J. Jeong, Z. S. Davidson, P. J. Collings, T. C. Lubensky, and A. G. Yodh. Chiral symmetry breaking and surface faceting in chromonic liquid crystal droplets with giant elastic anisotropy. *Proc. Natl. Acad. Sci.*, 111(5):1742–1747, 2014.

52. S. Zhou, K. Neupane, Y. A. Nastishin, A. R. Baldwin, S. V. Shiyanovskii, O. D. Lavrentovich, and S. Sprunt. Elasticity, Viscosity, and Orientational Fluctuations of a Lyotropic Chromonic Nematic Liquid Crystal Disodium Cromoglycate. *Soft Matter*, 10(34):6571–81, 2014.

53. S. Zhou, Y. A. Nastishin, M. M. Omelchenko, L. Tortora, V. G. Nazarenko, O. P. Boiko, T. Ostapenko, T. Hu, C. C. Almasan, S. N. Sprunt, and et al. Elasticity of Lyotropic Chromonic Liquid Crystals Probed by Director Reorientation in a Magnetic Field. *Phys. Rev. Lett.*, 109(3):037801, 2012.

54. J. Jeong, L. Kang, Z. S. Davidson, P. J. Collings, T. C. Lubensky, and A. Yodh. Chiral structures from achiral liquid crystals in cylindrical capillaries. *Proc. Natl. Acad. Sci.*, 112(15):E1837–E1844, 2015.

55. R. B. Meyer. Macroscopic phenomena in nematic polymers. In A. Ciferri, W. Krigbaum, and R. B. Meyer, editors, *Polymer Liquid Crystals*, pages 133 – 163. Academic Press, 1982. ISBN 978-0-12-174680-3.

56. J. L. West. Phase separation of liquid crystals in polymers. *Mol. Cryst. Liq. Cryst. Incorporating Nonlinear Opt.*, 157(1):427–441, 1988.

57. D. Nwabunma and T. Kyu. Phase behavior, photopolymerization, and morphology development in mixtures of eutectic nematic liquid crystal and photocurable monomer. *Polymer*, 42(2):801–806, 2001.

58. B. Oyarzún, T. van Westen, and T. J. H. Vlugt. Isotropic-nematic phase equilibria of hard-sphere chain fluids-pure components and binary mixtures. *J. Chem. Phys.*, 142(6):064903, 2015.

59. J. M. Polson and E. Burnell. Nematic-isotropic phase coexistence in a lebwohl-lasher model binary liquid crystal mixture. *Chem. Phys. Lett.*, 281(December): 207–211, 1997.

60. V. Yarmolenko. *Lattice Modelling of Liquid Crystal Mixtures*. PhD thesis, Materials Reseach Institute, Sheffield Hallam University, 2003.

61. J. K. Gupta, M.-V. Meli, S. Teren, and N. L. Abbott. Elastic energy-driven phase separation of phospholipid monolayers at the nematic liquid-crystal˘aqueous interface. *Phys. Rev. Lett.*, 100:048301, 2008.

62. P. A. Lebwohl and G. Lasher. Nematic-liquid-crystal order - a monte carlo calculation. *Phys. Rev. A*, 6(1):426–429, 1972.

63. P. Palffy-Muhoray, D. Dunmur, and A. Price. Orientational order and refractive indices in binary nematic mixtures. *Chem. Phys. Lett.*, 93(6):572–577, 1982.

64. U. Fabbri and C. Zannoni. A monte carlo investigation of the lebwohl-lasher lattice model in the vicinity of its orientational phase transition. *Mol. Phys.*, 58 (4):763–788, 1986.

65. F. Wang and D. P. Landau. Efficient, multiple-range random walk algorithm to calculate the density of states. *Phys. Rev. Lett.*, 86:2050–2053, 2001.

66. R. Shekhar, J. K. Whitmer, R. Malshe, J. A. Moreno-Razo, T. F. Roberts, and J. J. de Pablo. Isotropicnematic phase transition in the lebwohllasher model from density of states simulations. *J. Chem. Phys.*, 136(23):234503, 2012.

67. A. Ferrenberg and R. Swendsen. New Monte Carlo technique for studying phase transitions. *Phys. Rev. Lett.*, 61(23):2635–2638, 1988.

68. S. Kumar, J. M. Rosenberg, D. Bouzida, R. H. Swendsen, and P. A. Kollman. The weighted histogram analysis method for free-energy calculations on biomolecules. I. The method. *J. Comput. Chem.*, 13(8):1011–1021, 1992.

69. D. Frenkel and B. Smit. *Understanding Molecular Simulation*. Elsevier, 2002. ISBN 9780122673511.

70. J. G. Briano and E. D. Glandt. Statistical thermodynamics of polydisperse fluids. *J. Chem. Phys.*, 80(7):3336, 1984.

71. S. Singh, M. Chopra, and J. J. de Pablo. Density of states-based molecular simulations. *Annu. Rev. Chem. Biomol. Eng.*, 3:369–394, 2012.

72. E. B. Kim, R. Faller, Q. Yan, N. L. Abbott, and J. J. de Pablo. Potential of mean force between a spherical particle suspended in a nematic liquid crystal and a substrate. *J. Chem. Phys.*, 117(16):7781–7787, 2002.

73. C. Chipot and A. Pohorille, editors. *Free Energy Calculations*. Springer-Verlag Berlin Heidelberg, 2007.

74. C. Zhou and R. N. Bhatt. Understanding and improving the Wang-Landau algorithm. *Phys. Rev. E*, 72(2):1–4, 2005.

75. A. A. Joshi, J. K. Whitmer, O. Guzmán, N. L. Abbott, and J. J. de Pablo. Measuring liquid crystal elastic constants with free energy perturbations. *Soft Matter*, 10:882–893, 2014.

76. J. K. Whitmer, C.-c. Chiu, A. A. Joshi, and J. J. de Pablo. Basis function sampling: A new paradigm for material property computation. *Phys. Rev. Lett.*, 113:190602, 2014.

77. D. J. Cleaver and M. P. Allen. Computer simulations of the elastic properties of liquid crystals. *Phys. Rev. A*, 43(4):1918–1931, 1991.

78. N. Metropolis, A. W. Rosenbluth, M. N. Rosenbluth, A. H. Teller, and E. Teller. Equation of State Calculations by Fast Computing Machines. *J. Phys. Chem.*, 21(6):1087–1092, 1953.

79. D. Jayasri, V. S. S. Sastry, and K. P. N. Murthy. Wang-landau monte carlo simulation of isotropic-nematic transition in liquid crystals. *Phys. Rev. E*, 72: 036702, 2005.

80. L. Janosi and M. Doxastakis. Accelerating flat-histogram methods for potential of mean force calculations. *J. Chem. Phys.*, 131(5):054105, 2009.

81. C. Casagrande, P. Fabre, M. A. Guedeau, and M. Veyssie. Observation of anisotropic droplets in nematic-nematic phase separation. *Europhys. Lett.*, 3 (1):73, 1987.

82. P. Palffy-Muhoray, A. Berlinsky, J. De Bruyn, and D. Dunmur. Coexisting nematic phases in binary mixtures of liquid crystals. *Phys. Lett. A*, 104(3): 159–162, 1984.

83. B. A. H. Huisman and A. Fasolino. Influence of latent heat and thermal diffusion on the growth of nematic liquid crystal nuclei. *Phys. Rev. E*, 76(2):1–7, 2007.

84. N. M. Abukhdeir, E. R. Soul, and A. D. Rey. Non-isothermal model for nematic spherulite growth. *Langmuir*, 24(23):13605–13613, 2008.

85. A. Matsuyama and T. Kato. Early stages of spinodal decomposition in binary liquid crystal mixtures. *J. Chem. Phys.*, 113(20):9300, 2000.

86. E. R. Soule and A. D. Rey. Modelling complex liquid crystal mixtures: from polymer dispersed mesophase to nematic nanocolloids. *Mol. Sim.*, 38(8-9):735–750, 2012.

87. M. V. Gorkunov, G. A. Shandryuk, A. M. Shatalova, I. Y. Kutergina, A. S. Merekalov, Y. V. Kudryavtsev, R. V. Talroze, and M. A. Osipov. Phase separation effects and the nematic-isotropic transition in polymer and low molecular weight liquid crystals doped with nanoparticles. *Soft Matter*, 9(13):3578–3588, 2013.

88. M. A. Osipov and M. V. Gorkunov. Molecular theory of phase separation in nematic liquid crystals doped with spherical nanoparticles. *ChemPhysChem*, 15 (7):1496–1501, 2014.

89. M. A. Osman. Physical properties of nematic mixtures. i. polar-polar and nonpolar-nonpolar systems. *J. Chem. Phys.*, 78(2):906, 1983.

90. G. Gray. New syntheses. the liquid crystal properties of some new mesogens. *J. Phys. Colloq. C*, 36(C1):1–337, 1975.

91. D. Meyerhofer. Elastic and dielectric constants in mixtures of nematic liquid crystals. *J. Appl. Phys.*, 46(12):5084–5087, 1975.

92. A. Chanishvili, G. Chilaya, G. Petriashvili, R. Barberi, R. Bartolino, G. Cipparrone, A. Mazzulla, and L. Oriol. Phototunable lasing in dye-doped cholesteric liquid crystals. *Appl. Phys. Lett.*, 83(26):5353–5355, 2003.

93. Z. Bradač, S. Kralj, and S. Žumer. Molecular dynamics study of nematic structures confined to a cylindrical cavity. *Phys. Rev. E*, 58:7447–7454, 1998.

94. C. Chiccoli, P. Pasini, F. Semeria, E. Berggren, and C. Zannoni. Computer Simulations of Cylindrically Confined Nematics. *Mol. Cryst. Liq. Cryst. Sci. Technol., Sect. A*, 290(1):237–244, 1996.

95. A. Sonnet, A. Kilian, and S. Hess. Alignment tensor versus director: Description of defects in nematic liquid crystals. *Phys. Rev. E*, 52:718–722, 1995.

96. N. Priezjev and R. A. Pelcovits. Surface extrapolation length and director structures in confined nematics. *Phys. Rev. E*, 62:6734–6738, 2000.

97. O. D. Lavrentovich, P. Pasini, C. Zannoni, and S. Žumer, editors. *Defects in Liquid Crystals: Computer Simulations, Theory and Experiments*. Springer Science + Business Media, 2001.

98. C. Chiccoli, P. Pasini, L. R. Evangelista, R. T. Teixeira-Souza, and C. Zannoni. Molecular organization of nematic liquid crystals between concentric cylinders: Role of the elastic anisotropy. *Phys. Rev. E*, 91:022501, 2015.

99. E. Bukusoglu, S. K. Pal, J. J. de Pablo, and N. L. Abbott. Colloid-in-liquid crystal gels formed via spinodal decomposition. *Soft Matter*, 10:1602–1610, 2014.

100. X. Wang, Y.-K. Kim, E. Bukusoglu, B. Zhang, D. S. Miller, and N. L. Abbott. Experimental insights into the nanostructure of the cores of topological defects in liquid crystals. *Phys. Rev. Lett.*, 116(14):147801, 2016.

101. J.-C. P. Gabriel and P. Davidson. Mineral liquid crystals from self-assembly of anisotropic nanosystems. In *Colloid Chemistry I*, pages 119–172. Springer, 2003.

102. G. W. Gray and S. M. Kelly. Liquid crystals for twisted nematic display devices. *J. Mater. Chem.*, 9:2037–2050, 1999.

103. M. A. Lohr, J. Cavallaro, Marcello, D. A. Beller, K. J. Stebe, R. D. Kamien, P. J. Collings, and A. G. Yodh. Elasticity-dependent self-assembly of micro-templated chromonic liquid crystal films. *Soft Matter*, 10(19):3477–3484, 2014.

104. D. Coursault, J. Grand, B. Zappone, H. Ayeb, G. Levi, N. Felidj, and E. Lacaze. Linear self-assembly of nanoparticles within liquid crystal defect arrays. *Adv. Mater.*, 24(11):1461–1465, 2012.

105. M. Ravnik, S. Čopar, and S. Žumer. Particles with changeable topology in nematic colloids. *J. Phys. Condens. Matter*, 27(35):354111, 2015.

106. V. Tomar, T. F. Roberts, N. L. Abbott, J. P. Hernndez-Ortiz, and J. J. de Pablo. Liquid crystal mediated interactions between nanoparticles in a nematic phase. *Langmuir*, 28(14):6124–6131, 2012. PMID: 22409589.

107. J. Gary M. Koenig, J. J. de Pablo, and N. L. Abbott. Characterization of the reversible interaction of pairs of nanoparticles dispersed in nematic liquid crystals. *Langmuir*, 25(23):13318–13321, 2009. PMID: 19928936.

108. I. I. Smalyukh, S. Chernyshuk, B. I. Lev, A. B. Nych, U. Ognysta, V. G. Nazarenko, and O. D. Lavrentovich. Ordered droplet structures at the liquid crystal surface and elastic-capillary colloidal interactions. *Phys. Rev. Lett.*, 93:117801, 2004.

109. I. I. Smalyukh, O. D. Lavrentovich, A. N. Kuzmin, A. V. Kachynski, and P. N. Prasad. Elasticity-mediated self-organization and colloidal interactions of solid spheres with tangential anchoring in a nematic liquid crystal. *Phys. Rev. Lett.*, 95:157801, 2005.

110. H. Eimura, D. S. Miller, X. Wang, N. L. Abbott, and T. Kato. Self-assembly of bioconjugated amphiphilic mesogens having specific binding moieties at aqueousliquid crystal interfaces. *Chem. Mater.*, 28(4):1170–1178, 2016.

111. T. Bera, J. Deng, and J. Fang. Protein-induced configuration transitions of polyelectrolyte-modified liquid crystal droplets. *J. Phys. Chem. B*, 118(18): 4970–4975, 2014.

112. P. Popov, E. K. Mann, and A. Jákli. Accurate optical detection of amphiphiles at liquid-crystal–water interfaces. *Phys. Rev. Appl.*, 1(3):034003, 2014.

113. M. Khan and S.-Y. Park. Specific detection of avidinbiotin binding using liquid crystal droplets. *Colloid Surf. B.*, 127:241–246, 2015.

114. V. Tomar, S. I. Hernandez, N. L. Abbott, J. P. Hernandez-Ortiz, and J. J. de Pablo. Morphological transitions in liquid crystal nanodroplets. *Soft Matter*, 8:8679–8689, 2012.

115. A. M. Lowe, B. H. Ozer, Y. Bai, P. J. Bertics, and N. L. Abbott. Design of surfaces for liquid crystal-based bioanalytical assays. *ACS Appl. Mater. Inter.*, 2(3):722–731, 2010. PMID: 20356273.

116. T. A. Wood, J. S. Lintuvuori, A. B. Schofield, D. Marenduzzo, and W. C. K. Poon. A self-quenched defect glass in a colloid-nematic liquid crystal composite. *Science*, 334(6052):79–83, 2011.

117. H. Stark. Physics of colloidal dispersions in nematic liquid crystals. *Phys. Rep*, 351(6):387–474, 2001.

118. D. Voloschenko, O. P. Pishnyak, S. V. Shiyanovskii, and O. D. Lavrentovich. Effect of director distortions on morphologies of phase separation in liquid crystals. *Phys. Rev. E*, 65(6):060701, 2002.

119. B. J. Berne and P. Pechukas. Gaussian model potentials for molecular interactions. *J. Chem. Phys.*, 56(8):4213–4216, 1972.

120. G. Luckhurst and P. Simmonds. Computer simulation studies of anisotropic systems. XXI. Parametrization of the Gay-Berne potential for model mesogens. *Mol. Phys.*, 80(2):233–252, 1993.

121. A. Emerson, G. Luckhurst, and S. Whatling. Computer simulation studies of anisotropic systems. XXIII. The Gay-Berne discogen. *Mol. Phys.*, 82(1):113–124, 1994.

122. M. A. Bates and G. R. Luckhurst. Computer simulation studies of anisotropic systems. XXX. The phase behavior and structure of a Gay-Berne mesogen. *J. Chem. Phys.*, 110(14):7087, 1999.

123. M. P. Allen, M. A. Warren, M. R. Wilson, A. Sauron, and W. Smith. Molecular dynamics calculation of elastic constants in GayBerne nematic liquid crystals. *J. Chem. Phys.*, 105:2850, 1996.

124. A. Humpert and M. P. Allen. Elastic constants and dynamics in nematic liquid crystals. *Mol. Phys.*, 113(17-18):2680–2692, 2015.

125. G. R. Luckhurst and K. Satoh. A computer simulation investigation of the freedericksz transition for the nematic phase of a Gay-Berne mesogen. *Mol. Cryst. Liq. Cryst.*, 402(1):85–102, 2003.

126. R. Berardi, A. P. J. Emerson, and C. Zannoni. Monte Carlo investigations of a GayBerne liquid crystal. *J. Chem. Soc, Faraday Trans.*, 89(22):4069–4078, 1993.

127. V. Palermo, F. Biscarini, and C. Zannoni. Abrupt orientational changes for liquid crystals adsorbed on a graphite surface. *Phys. Rev. E*, 57(3):R2519–R2522, 1998.

128. O. Cienega-Cacerez, J. A. Moreno-Razo, E. Díaz-Herrera, and E. J. Sambriski. Phase equilibria, fluid structure, and diffusivity of a discotic liquid crystal. *Soft Matter*, 10(18):3171–82, 2014.

129. P. Prybytak, W. J. Frith, and D. J. Cleaver. Hierarchical self-assembly of chiral fibres from achiral particles. *Interface Focus*, 2(5):651–657, 2012.

130. J. Kushick and B. J. Berne. Computer simulation of anisotropic molecular fluids. *J. Chem. Phys.*, 64(4):1362–1367, 1976.

131. D. J. Cleaver, C. M. Care, M. P. Allen, and M. P. Neal. Extension and generalization of the Gay-Berne potential. *Phys. Rev. E*, 54(1):559–567, 1996.

132. R. Berardi, C. Fava, and C. Zannoni. A generalized Gay-Berne intermolecular potential for biaxial particles. *Chem. Phys. Lett.*, 236(4-5):462–468, 1995.

133. P. A. Golubkov and P. Ren. Generalized coarse-grained model based on point multipole and Gay-Berne potentials. *J. Chem. Phys.*, 125(6), 2006.

134. C. Zannoni, C. Fisica, and V. Risorgimento. Molecular design and computer simulations of novel mesophases. *J. Mater. Chem.*, 11(11):2637–2646, 2001.

135. G. Luckhurst, R. Stephens, and R. Phippen. Computer simulation studies of anisotropic systems XIX: mesophases formed by the Gay-Berne model mesogen. *Liq. Cryst.*, 8(4):451–464, 1990.

136. R. Memmer, H.-G. Kuball, and A. Schönhofer. Computer simulation of chiral liquid crystal phases. I. The polymorphism of the chiral Gay-Berne fluid. *Liq. Cryst.*, 15(3):345–360, 1993.

137. R. Memmer. Computer simulation of chiral liquid crystal phases VIII. Blue phases of the chiral Gay-Berne fluid. *Liq. Cryst.*, 27(4):533–546, 2000.

138. E. Cañeda-Guzmán, J. Moreno-Razo, E. Díaz-Herrera, and E. Sambriski. Molecular aspect ratio and anchoring strength effects in a confined Gay-Berne liquid crystal. *Mol. Phys.*, 112(8):1149–1159, 2013.

139. R. C. Singh. Orientational phase transition of long elongated GayBerne molecules. *Mol. Cryst. Liq. Cryst.*, 457(1):67–82, 2006.

140. E. Cañeda-Guzmán, J. A. Moreno-Razo, E. Díaz-Herrera, and E. J. Sambriski. *Experimental and Theoretical Advances in Fluid Dynamics*, chapter Structure and translational diffusion in liquid crystalline phases of a Gay-Berne mesogen: A molecular dynamics study, pages 25–38. Springer Berlin Heidelberg, Berlin, Heidelberg, 2012. ISBN 978-3-642-17958-7.

141. Q. Ji, R. Lefort, and D. Morineau. Influence of pore shape on the structure of a nanoconfined Gay-Berne liquid crystal. *Chem. Phys. Lett.*, 478(46):161–165, 2009.

142. G. R. Luckhurst and K. Satoh. Computer simulation of the field-induced alignment of the smectic A phase of the Gay-Berne mesogen GB(4.4,20.0,1,1). *Mol. Cryst. Liq. Cryst.*, 394(1):153–169, 2003.

143. E. D. Miguel, F. J. Blas, and E. M. D. Río. Molecular simulation of model liquid crystals in a strong aligning field. *Mol. Phys.*, 104(18):2919–2927, 2006.

144. J. K. Whitmer, A. M. Fluitt, L. Antony, J. Qin, M. McGovern, and J. J. De Pablo. Sculpting bespoke mountains: Determining free energies with basis expansions. *J. Chem. Phys.*, 143(4), 2015.

145. A. Laio and M. Parrinello. Escaping Free-Energy Minima. *Proc. Natl. Acad. Sci.*, 99(20):12562–12566, 2002.

146. E. Darve, D. Rodrguez-Gmez, and A. Pohorille. Adaptive biasing force method for scalar and vector free energy calculations. *J. Chem. Phys.*, 128(14):144120, 2008.

147. H. Sidky and J. K. Whitmer. Elastic response and phase behavior in binary liquid crystal mixtures. *Soft Matter*, 12:4489–4498, 2016.

148. J. Stelzer, L. Longa, and H.-R. Trebin. Elastic constants of nematic liquid crystals from molecular dynamics simulations. *Mol. Cryst. Liq. Cryst. A*, 262 (1):455–461, 1995.

149. J. Stelzer, L. Longa, and H.-R. Trebin. Molecular dynamics simulations of a Gay-Berne nematic liquid crystal: Elastic properties from direct correlation functions. *J. Chem. Phys.*, 103(8):3098, 1995.

150. N. H. Phuong, G. Germano, and F. Schmid. Elastic constants from direct correlation functions in nematic liquid crystals: A computer simulation study. *J. Chem. Phys.*, 115(15):7227–7234, 2001.

151. H. Sidky. SAPHRON - A Lightweight C++11 Monte Carlo Molecular Simulation Engine. `https://github.com/hsidky/SAPHRON`, 2016.

152. N. V. Madhusudana and R. Pratibha. Elasticity and orientational order in some cyanobiphenyls: Part IV. reanalysis of the data. *Mol. Cryst. Liq. Cryst.*, 89(1-4):249–257, 1982.

153. P. G. de Gennes and J. Prost. *The Physics of Liquid Crystals*, volume 4. Oxford university press, second edition, 1994.

154. D. Caprion, L. Bellier-Castella, and J.-P. Ryckaert. Influence of shape and energy anisotropies on the phase diagram of discotic molecules. *Phys. Rev. E*, 67:041703, 2003.

155. N. H. Tinh, H. Gasparoux, and C. Destrade. An homologous series of disc-like mesogens with nematic and columnar polymorphism. *Mol. Cryst. Liq. Cryst.*, 68(1):101–111, 1981.

156. M. A. Bates and G. R. Luckhurst. Computer simulation studies of anisotropic systems. XXVI. Monte Carlo investigations of a Gay-Berne discotic at constant pressure. *J. Chem. Phys.*, 104(17):6696–6709, 1996.

157. E. Kats and M. I. Monastyrsky. Ordering in discotic liquid crystals. *J. Phys. France*, 45(4):709–714, 1984.

158. M. Osipov and S. Hess. The elastic constants of nematic and nematic discotic liquid crystals with perfect local orientational order. *Mol. Phys.*, 78(5):1191–1201, 1993.

159. H. K. Bisoyi and S. Kumar. Discotic nematic liquid crystals: science and technology. *Chem. Soc. Rev.*, 39(1):264–285, 2010.

160. V. A. Raghunathan, N. V. Madhusudana, S. Chandrasekhar, and C. Destrade. Bend and splay elastic constants of a discotic nematic. *Mol. Cryst. Liq. Cryst.*, 148(1):77–83, 1987.

161. G. Heppke, A. Ranft, and B. Sabaschus. Bend and splay elastic constants of some discotic nematic compounds. *Mol. Cryst. Liq. Cryst. Lett.*, 8(1):17–25, 1991.

162. D. Venkata Sai, G. Mirri, P. H. J. Kouwer, R. Sahoo, I. Musevic, and S. Dhara. Unusual temperature dependence of elastic constants of an ambient-temperature discotic nematic liquid crystal. *Soft Matter*, 12(11):2960–2964, 2016.

163. T. J. Phillips, J. C. Jones, and D. G. McDonnell. On the influence of short range order upon the physical properties of triphenylene nematic discogens. *Liq. Cryst.*, 15(2):203–215, 1993.

164. R. Berardi, S. Orlandi, and C. Zannoni. Monte carlo simulation of discotic gay–berne mesogens with axial dipole. *J. Chem. Soc., Faraday T.*, 93:1493–1496, 1997.

165. A. Poniewierski and J. Stecki. Statistical theory of the Frank elastic constants. *Phys. Rev. A*, 25:2368–2370, 1982.

166. R. H. Chen. *Liquid Crystal Displays*. John Wiley & Sons, Inc., 2011. ISBN 9781118084359.

167. H. Kikuchi, M. Yokota, Y. Hisakado, H. Yang, and T. Kajiyama. Polymer-stabilized liquid crystal blue phases. *Nat. Mater.*, 1(1):64–8, 2002.

168. G. Li, D. L. Mathine, P. Valley, P. Äyräs, J. N. Haddock, M. Giridhar, G. Williby, J. Schwiegerling, G. R. Meredith, B. Kippelen, et al. Switchable electro-optic diffractive lens with high efficiency for ophthalmic applications. *Proc. Natl. Acad. Sci.*, 103(16):6100–6104, 2006.

169. P. J. Collings, J. N. Goldstein, E. J. Hamilton, B. R. Mercado, K. J. Nieser, and M. H. Regan. The Nature of the Assembly Process in Chromonic Liquid Crystals. *Liq. Cryst. Rev.*, 3(1):1–27, 2015.

170. P. K. Maiti, Y. Lansac, M. A. Glaser, and N. A. Clark. Isodesmic Self-assembly in Lyotropic Chromonic Systems. *Liq. Cryst.*, 29(5):619–626, 2002.

171. M. Walker, A. J. Masters, and M. R. Wilson. Self-assembly and Mesophase Formation in a Non-ionic Chromonic Liquid Crystal System: Insights From Dissipative Particle Dynamics Simulations. *Phys. Chem. Chem. Phys.*, 16(42): 23074–81, 2014.

172. R. G. Edwards, J. Henderson, and R. L. Pinning. Simulation of Self-assembly and Lyotropic Liquid Crystal Phases in Model Discotic Solutions. *Mol. Phys.*, 86(4):567–598, 1995.

173. J. Lydon. Chromonic Review. *J. Mater. Chem.*, 20(45):10071, 2010.

174. E. A. Mills, M. H. Regan, V. Stanic, and P. J. Collings. Large Assembly Formation via a Two-step Process in a Chromonic Liquid Crystal. *J. Phys. Chem. B*, 116(45):13506–13515, 2012.

175. M. Walker and M. R. Wilson. A Simple Model for Chromonic Aggregation. *Mol. Cryst. Liq. Cryst.*, 612(1):117–125, 2015.

176. M. B. Sweatman, R. Fartaria, and L. Lue. Cluster Formation in Fluids with Competing Short-range and Long-range Interactions. *J. Chem. Phys.*, 140(12): 124508, 2014.

177. C. J. Fennell and J. D. Gezelter. Is the ewald summation still necessary? pairwise alternatives to the accepted standard for long-range electrostatics. *J. Chem. Phys.*, 124(23):234104, 2006.

178. V. R. Horowitz, L. A. Janowitz, A. L. Modic, P. A. Heiney, and P. J. Collings. Aggregation Behavior and Chromonic Liquid Crystal Properties of an Anionic Monoazo Dye. *Phys. Rev. E*, 72(4):1–10, 2005.

179. D. Trzesniak, A.-P. E. Kunz, and W. F. van Gunsteren. A comparison of methods to compute the potential of mean force. *Chemphyschem*, 8(1):162–169, 2007.

180. J. Gezelter, S. Kuang, J. Marr, K. Stocker, C. Li, C. Vardeman, T. Lin, C. Fennell, X. Sun, and K. Daily. Openmd, an open source engine for molecular dynamics, 2010.

181. R. Chang. Orientational Order in MBBA From Optical Anisotropy Measurements. *Mol. Cryst. Liq. Cryst.*, 30(1-2):155–165, 1975.

182. K. T. Nguyen, F. Sciortino, and C. De Michele. Self-assembly-driven Nematization. *Langmuir*, 30(16):4814–4819, 2014.

183. A. Akinshina, M. Walker, M. R. Wilson, G. J. T. Tiddy, A. J. Masters, and P. Carbone. Thermodynamics of the Self-assembly of Non-ionic Chromonic Molecules using Atomistic Simulations. The Case of TP6EO2M in Aqueous Solution. *Soft Matter*, 11(4):680–91, 2015.

184. A. J. Dickinson, N. D. LaRacuente, C. B. McKitterick, and P. J. Collings. Aggregate structure and free energy changes in chromonic liquid crystals. *Mol. Cryst. Liq. Cryst.*, 509(1):9–20, 2009.

185. K. Nayani, J. Fu, R. Chang, J. O. Park, and M. Srinivasarao. Using chiral Tactoids as Optical Probes to Study the Aggregation Behavior of Chromonics. *Proc. Natl. Acad. Sci.*, 114(15):3826–3831, 2017.

186. X. Li, J. C. Armas-Pérez, J. P. Hernández-Ortiz, C. G. Arges, X. Liu, J. A. Martínez-González, L. E. Ocola, C. Bishop, H. Xie, J. J. de Pablo, et al. Directed self-assembly of colloidal particles onto nematic liquid crystalline defects engineered by chemically patterned surfaces. *ACS Nano*, 11(6):6492–6501, 2017.

187. V. G. Nazarenko, O. P. Boiko, M. I. Anisimov, A. K. Kadashchuk, Y. A. Nastishin, A. B. Golovin, and O. D. Lavrentovich. Lyotropic chromonic liquid crystal semiconductors for water-solution processable organic electronics. *Apply. Phys. Lett.*, 97(26):263305, 2010.

188. S. V. Shiyanovskii, O. D. Lavrentovich, T. Schneider, T. Ishikawa, I. I. Smalyukh, C. J. Woolverton, G. D. Niehaus, and K. J. Doane. Lyotropic Chromonic Liquid Crystals for Biological Sensing Applications. *Mol. Cryst. Liq. Cryst.*, 434 (1):259/[587]–270/[598], 2005.

189. R. L. Sutherland, V. P. Tondiglia, L. V. Natarajan, T. J. Bunning, and W. W. Adams. Electrically switchable volume gratings in polymer-dispersed liquid crystals. *Appl. Phys. Lett.*, 64(9):1074–1076, 1994.

190. L. Tran, M. O. Lavrentovich, D. A. Beller, N. Li, K. J. Stebe, and R. D. Kamien. Lassoing saddle splay and the geometrical control of topological defects. *Proc. Natl. Acad. Sci.*, 113(26):7106–7111, 2016.

191. Ž. Kos and M. Ravnik. Relevance of saddle-splay elasticity in complex nematic geometries. *Soft Matter*, 12(4):1313–1323, 2016.

192. G. Tiberio, L. Muccioli, R. Berardi, and C. Zannoni. Towards in silico liquid crystals. realistic transition temperatures and physical properties for n-cyanobiphenyls via molecular dynamics simulations. *ChemPhysChem*, 10(1): 125–136, 2009.

193. S. Singh. Curvature elasticity in liquid crystals. *Phys. Rep.*, 277(5-6):283–384, 1996.

194. S. Faetti, M. Gatti, and V. Palleschi. A new torsion pendulum technique to measure the twist elastic constant of liquid crystals. *J. Phys. Lett. Paris*, 46 (18):881–886, 1985.

195. G.-P. Chen, H. Takezoe, and A. Fukuda. Determination of Ki (i = 13) and μj (j = 26) in 5CB by observing the angular dependence of Rayleigh line spectral widths. *Liq. Cryst.*, 5(1):341–347, 1989.

196. V. Fredericksz and V. Zolina. Forces causing the orientation of an anisotropic liquid. *T. Faraday Soc.*, 29(140):919, 1933.

197. M. Rahimi, H. Ramezani-Dakhel, R. Zhang, A. Ramirez-Hernandez, N. L. Abbott, and J. J. de Pablo. Segregation of liquid crystal mixtures in topological defects. *Nat. Comm.*, 8:15064, 2017.

198. H. Ramezani-Dakhel, M. Sadati, M. Rahimi, A. Ramirez-Hernandez, B. Roux, and J. J. de Pablo. Understanding Atomic-Scale Behavior of Liquid Crystals at Aqueous Interfaces. *J. Chem. Theory Comput.*, 13(1):237–244, 2017.

199. M. Sadati, H. Ramezani-Dakhel, W. Bu, E. Sevgen, Z. Liang, C. Erol, M. Rahimi, N. Taheri Qazvini, B. Lin, N. L. Abbott, B. Roux, M. L. Schlossman, and J. J. de Pablo. Molecular structure of canonical liquid crystal interfaces. *J. Am. Chem. Soc.*, 139(10):3841–3850, 2017.

200. N. J. Boyd and M. R. Wilson. Optimization of the GAFF force field to describe liquid crystal molecules: the path to a dramatic improvement in transition temperature predictions. *Phys. Chem. Chem. Phys.*, 17(38):24851–24865, 2015.

201. A. Pizzirusso, M. E. Di Pietro, G. De Luca, G. Celebre, M. Longeri, L. Muccioli, and C. Zannoni. Order and conformation of biphenyl in cyanobiphenyl liquid crystals: A combined atomistic molecular dynamics and 1h nmr study. *ChemPhysChem*, 15(7):1356–1367, 2014.

202. A. Zakharov and A. Maliniak. Structure and elastic properties of a nematic liquid crystal: A theoretical treatment and molecular dynamics simulation. *Eur. Phys. J. E*, 4(1):85–91, 2001.

203. M. Cestari and A. Ferrarini. Curvature elasticity of nematic liquid crystals: simply a matter of molecular shape? Insights from atomistic modeling. *Soft Matter*, 5:3879, 2009.

204. M. J. Abraham, T. Murtola, R. Schulz, S. Páll, J. C. Smith, B. Hess, and E. Lindahl. GROMACS: High performance molecular simulations through multi-level parallelism from laptops to supercomputers. *SoftwareX*, 12:19–25, 2015.

205. L. Martinez, R. Andrade, E. G. Birgin, and J. M. Martínez. Packmol: A package for building initial configurations for molecular dynamics simulations. *J. Comput. Chem.*, 30(13):2157–2164, 2009.

206. H. Sidky, Y. J. Colón, J. Helfferich, B. J. Sikora, C. Bezik, W. Chu, F. Giberti, A. Z. Guo, X. Jiang, J. Lequieu, J. Li, J. Moller, M. J. Quevillon, M. Rahimi, H. Ramezani-Dakhel, V. S. Rathee, D. R. Reid, E. Sevgen, V. Thapar, M. A. Webb, J. K. Whitmer, and J. J. de Pablo. SSAGES: Software Suite for Advanced General Ensemble Simulations. *J. Phys. Chem.*, 148(4):044104, 2018.

207. H. J. C. Berendsen, J. R. Grigera, and T. P. Straatsma. The missing term in effective pair potentials. *J. Phys. Chem.*, 91(24):6269–6271, 1987.

208. H. Mori, E. C. Gartland Jr, J. R. Kelly, and P. J. Bos. Multidimensional director modeling using the q tensor representation in a liquid crystal cell and its application to the π cell with patterned electrodes. *Jpn. J. Appl. Phys.*, 38 (1R):135, 1999.